Università degli Studi di Cagliari

Università degli Studi di Sassari

PhD DEGREE

Chemical Sciences and Technologies

32nd Cycle PON-RI

# TITLE OF THE PhD THESIS

## Design of Siliceous Materials from Industrial Waste

Scientific Disciplinary Sectors

CHIM/02 CHIM/04


| | |
|---|---|
| PhD Student: | Mirko Antonio Vacca |
| Coordinator of the PhD Programme | Prof. Stefano Enzo |
| Supervisor | Prof. Carla Cannas<br>Dr. Luca Pala<br>Dr. Václav Tyrpekl |



Final exam. Academic Year 2018 – 2019

Thesis defence: June - July 2020 Session

# Statement of Confidentiality

*This thesis contains sensitive information and can be consulted only by the author, his advisors, and the members of the Ph.D. Examining Broad. Access to the data by third parties may be granted upon explicit joint consent from the author and at least two advisers. Republishing, duplicating, and disclosing the content of this thesis, either totally or partially, are severely forbidden.*

*To My Parents*

*In Loving Memory of*
*Prof. Dr. Daniel Nižňanský*

*"He who has a why to live for can bear almost any how."*
*Friedrich Nietzsche, Götzen-Dämmerung.*

# Contents

# List of Figures

# List of Tables

# Introduction and Aim of the Work

Silica ($SiO_2$) is one of the most commonly found compound on the Earth's crust and has accompanied human technological advancements since the beginning of our civilization. Despite its simple chemical formula, silica exhibits a number of polymorphous and amorphous forms, including glass sate. Its fundamental repetitive units are $SiO_4$ tetrahedra bonding one another by sharing their vertices. In crystalline silica, $SiO_4$ tetrahedra are arranged according to a well-defined three-dimensional long-range order extending all over the entire material. Examples of crystalline silica include quartz, tridymite, and cristobalite. Conversely, no repetitive pattern can be found throughout the solid in its amorphous state. Common industrially relevant varieties of amorphous silica include precipitated, fumed, colloidal, hydrophobic silica, and silica gel. Among amorphous $SiO_2$-based materials, a relatively new class when was discovered is represented by ordered mesoporous siliceous materials. The first material of such class to be synthesized was MCM-41 in 1992, which belongs to the so-called M41S family. The salient feature of MCM-41 is the long-range order of hexagonally-arranged pores of width in the mesoporous range (from 2 to 50 nm). For this reason, MCM-41 and other ordered mesoporous materials have been attracting the attention of the scientific community for their potential applications in a wide range of fields. However, the high cost of the conventional precursors used for the synthesis of these materials (such as TEOS and TMOS) thwarts their large-scale production, eliciting the need for more economical alternatives.

This thesis is devoted to ascertaining the feasibility of obtaining both precipitated and mesostructured silica from $H_2SiF_6$ (FSA), a low-cost waste material produced by the phosphate fertilizer and the HF industries. As far as

precipitated silica is concerned, FSA might be an interesting alternative in manufacturing silica to be used as a reinforcing agent in tyres, with significant environmental and economical advantages in the perspective of setting up a possible industrial process in which a hazardous waste is utilized, lowering the costs associated with the production of precipitated $SiO_2$ and rendering it a competitive partial or complete alternative to carbon black, the most common reinforcing agent for tyres. As for mesostructured materials, FSA will serve as an alternative silicon source to TEOS and other alkoxides. A head-to-head comparison was drawn between the the TEOS- and the FSA-derived to identify the best experimental conditions to obtain a support to impregnated with an active phase. Such nanocomposites may be useful in the removal process of $H_2S$ from syngas. Along the lines of precipitated silica, the use of hexafluorosilicic acid is functional in reducing the cost associated with the synthesis of high value-added products such as MCM-41, which is hindered by the high cost of TEOS. Moreover, by coupling the use of FSA with the recovery of the templating agent, it might be possible to envisage an industrial process for a larger-scale, low-cost, and environmentally friendly production of MCM-41.

The first three chapters introduce the main concepts to understand the experimental work presented later in the following chapters. The first chapter provides basic knowledge about precipitated silica and hexafluorosilicic acid while chapter 2 delves into the topic of using precipitated silica in tyres focusing on how tyre properties (such as rolling resistance, wear resistance, and wet skid resistance) are affected by it.
The third chapter gives a brief introduction on ordered mesostructured materials, their characteristics, mechanisms of formation, and the silicon sources commonly used in their manufacture process.
Chapter 4 is devoted to briefly outlining how coal-derived syngas may still play a part as a transition, albeit non-renewable, energy source and how desulfurization process of syngas by means of mesostructured nanocomposites may serve as a valuable process to capture the $H_2S$ contained in it and prevent its obnoxious impact on the environment.
Chapter 5 discusses the experimental work carried out to synthesize precipitated silica from hexafluorosilicic acid to be used as a filler in tyres. This experimental work consisted in ascertaining the best conditions of pH, temperature, reactant

concentration, and other parameters to obtain a product featuring the desired properties for the intended use. Eventually, the samples deemed to be the most suitable were used to prepare tread compounds and their reinforcing performances were assessed. These tests were performed in collaboration with the University of Milan "Bicocca".

Chapter 6 describes the first attempts to utilize $H_2SiF_6$ in the synthesis of MCM-41 as a precursor according to a synthetic procedure adopted by the author's research group to obtain MCM-41 from TEOS. Furthermore, it reports the experimental route to obtain a suitable MCM-41 material to be used as a support to manufacture nanocomposites to be used in the sweetening process of syngas. This was realized by systematically comparing the properties of the materials obtained from TEOS and FSA after carrying out experiments in which parameters such as temperature, reaction duration, presence of ethyl acetate, and ancillary hydrothermal treatment had been changed one at a time. This chapter also deals with the issue of recovery CTAB from the as-synthesized mesostructured material by using either ethanol or water and an investigation on the textural properties of the TEOS- and FSA-bare sorbents *via* $^{29}Si$ MAS Solid State NMR and FT-IR.

Chapter 7 describes how these bare supports synthesized were used to obtain $Fe_2O_3$ and their related $ZnFe_2O_4$-bearing nanocomposites. They were thoroughly characterized, tested for $H_2S$ removal from syngas, and compared one another.

The thesis is closed by a conclusion chapter where a recapitulation of the results of the present work and the future insights are given, followed by an appendix containing brief descriptions of the analytical techniques and the equipment used throughout this work.

# 1

# Precipitated $SiO_2$ and $H_2SiF_6$: an overview

*This introductory chapter provides some basic information about precipitated silica, in particular its production, physicochemical and surface properties, applications while some notions on hexafluorosilicic acid are given in terms of chemical properties, uses, and prospective as an alternative of both silicon and fluorine.*

## 1.1 Precipitated Silica

Precipitated silica (*PS*) constitutes the most commercially important group of silicas by reason of the quantity produced *per* year. It has been estimated that the global market share for precipitated silica was valued at 1.96 billion USD in 2018, with Degussa-Hülls, Akzo, PPG, Huber, Evonik, and Rhodia as the major manufacturers.[1]

### 1.1.1 Production

Synthesis of *PS* involves the reaction between a silicon source, such as an aqueous alkali metal silicate solution (*e.g.*, water glass), and a mineral acid, generally $H_2SO_4$. Other silicon source and acids may be used, but seldom in industrial settings. The reaction between the alkali silicate solution and sulfuric acid is exemplified in equation 1:

$$Na_2O \cdot 3.3\,SiO_2 + H_2SO_4 \longrightarrow x\,SiO_2 + Na_2SO_4 + H_2O \qquad (\textbf{Eq. } 1)$$

Polymerization occurs with the formation of siloxane groups (O-Si-O) through

a mechanism of hydrolysis and condensation. The scheme reported below depicts how polymerization ends up with the formation of precipitated $SiO_2$:

*Monomer → Dimer → Cyclic Molecule → Particle → Precipitated Silica*

The first spherical particles formed during the reaction are called primary particles (usually 2 - 20 nm) and may be regarded as the basic assembly units of precipitated silica. When primary particles bond together *via* siloxane (O-Si-O) bonds, they form an aggregate. Given the covalent nature of this bond, it is impossible to split up the aggregates back into primary particles. Finally, aggregates bond together through Van-der-Walls forces and hydrogen bonds making up an agglomerate (Fig.1.1), of dimensions ranging from 2 $\mu$m up to 3000 $\mu$m.

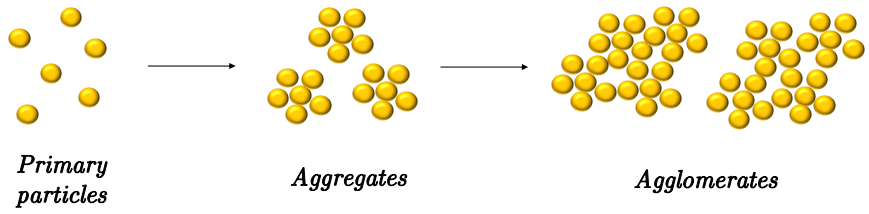


***Figure 1.1*** *Different stages of aggregation in precipitated $SiO_2$, form primary particles to agglomerates.*

The steps involved in manufacturing precipitated $SiO_2$ are precipitation, filtration, and drying. The so-obtained silica is usually sold in the form of granules and micropearls.
Separation is carried out by filtration followed by a washing step. Given the considerable content of water in the filtered cake (up to 50 %), drying is required. This process is pivotal in determining the properties of the end product and is carried out in a variety of apparatuses including plate, spray, nozzle spray, rotary, and belt dryers. An ancillary procedure is grinding, which involves the use of mills with the aim of obtaining particles of desired fineness. Compression and/or granulation may be used to reduce volumes and preventing dust formation.[2]

### 1.1.2 Physicochemical and Surface Properties

Assessing the properties of $SiO_2$ largely consists in the study of its morphology. Particle size is one of the most important property of *PS* as several

of its desired end uses depend on this parameter. Factors such as composition, concentration, and ratio of reactants in the precipitating solution, as well as reaction time, reaction temperature, and stirring rate are all implicated in determining particle size. Electron microscopy imaging and dynamic light scattering are the elective techniques for its assessment.

Specific surface area is another critical property of *PS*, especially in the field of adsorptive materials and rubber reinforcement. It is usually determined by $N_2$-ad/desorption measurements and applying the BET method. Typical values of specific surface area for PS vary from 25 to 800 $m^2$ $g^{-1}$.[3] $N_2$-ad/desorption measurements are also useful for determining porosity and pore size distribution, especially when mesopores (2 - 50 nm of diameter) are concerned. Conversely, mercury intrusion porosimetry is best applied to gauge pores with dimension above 30 nm.[3–5]

Loss on drying (LoD) quantifies the loss in weight upon heating at 105 °C for a minimum of 2 hours. This loss in weight is due to physically adsorbed water. Typical values of LoD for *PS* lie between 2.5 and 7 %. A similar property is Loss on ignition (LoI) which measures the loss in weight of both physically and chemically bonded water upon "ignition", a treatment involving very high temperatures for an apt length of time. LoI values for *PS* often typically range from 3 to 10 %.[2,6]

### 1.1.3 Surface and Reactivity

Surface properties of $SiO_2$ depend on two reactively different chemical groups: the reactive and hydrophilic silanols (≡Si-OH) and the hydrophobic siloxanes (Si-O-Si). By its own nature, amorphous silica lacks long-range ordered arrangement of the $SiO_4$ tetrahedra. As a consequence, relative distances among the silanol groups on the surface are far from being regular. This fact explains the different physicochemical behaviours of silanols on a given $SiO_2$ surface.[6]

Taking into account their relative position, the likelihood of forming hydrogen bonds and the Si atom coordination, silanols may be classified as *a) isolated*, where the silicon atom bonds three oxygen atoms located into the bulk and a single hydroxyl group, *b) vicinal*, in which two proximal isolated silanols are able to form a hydrogen bond, and *c) geminal* where the central silicon atom is bonded with two bulk oxygen atoms and two hydroxyls (Fig.1.2).[7]

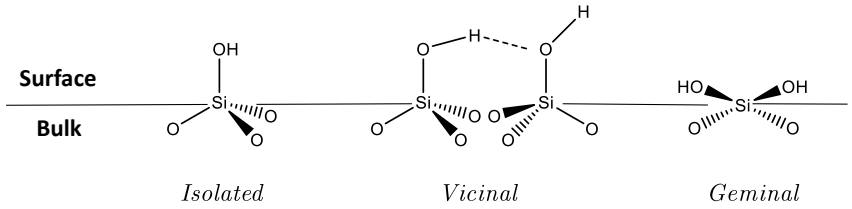


***Figure 1.2*** *Silanol groups found on an amorphous silica surface.*

Hydroxyl groups are responsible for the hydrophilic nature of $SiO_2$ and for its reactivity. In 1956, Sears developed an analytical technique to quantify this property *via* titration by neutralization with NaOH.[8] The quantity of NaOH 0.1 M needed to titrate a silica suspension from pH 6 to pH 9 is known as "Sears Number", which is still used in the industry to classify silica according to its hydrophilicity.[2]
Surface reactivity also implies the possibility of surface modification. One of the most industrially important, especially in the tyre industry, is hydrophobization which is carried out by reacting *PS* with silicone fluids or adding into the precipitate solution organochlorosilanes: these processes are known as dry and wet process, respectively.[2,9]

### 1.1.4 Applications

In virtue of their tunable physicochemical properties, uses of *PS* are various and matter of interest in numerous industrial fields. As an example, Figure 1.3 reports the worldwide consumption of precipitated silica in 1999.[2]

PS is added into toothpastes for its ability to clean and polish the dental enamel without abrading it. In the food and pharmaceutical industries, it is used as absorbent, anti-caking agent, and rheology modifier. Paper adsorptivity of ink is enhanced when *PS* are used. *PS* can also be useful as carriers to turn liquids or caking-prone hygroscopic solids into dispersible powders, improving the manageability of these substances: this is particularly relevant in agriculture where pesticides, herbicides, fungicides, and insecticides need to be stored,

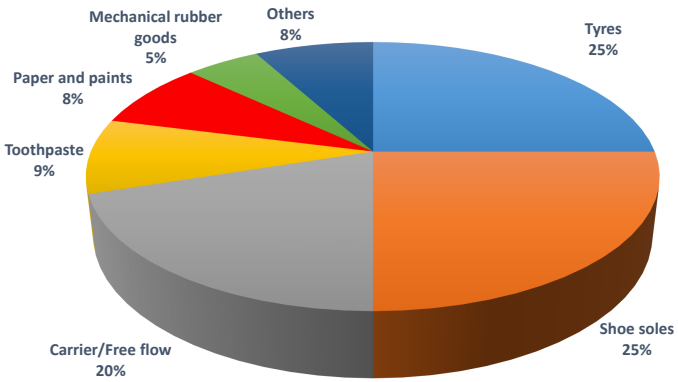


***Figure 1.3*** *Worldwide precipitated $SiO_2$ usage in 1999, modified after Ullman [2]*

moved, weighed, and uniformly dispersed over the fields.
However, the first and by far most important application is to improve the performance of rubber and plastics by acting as a reinforcing agent. Indeed, adding appropriate amounts of *PS* into rubber matrices enhances their hardness, tensile and tear strength, as well as abrasion resistance in a wide range of rubber and plastics.[2] The topic of reinforcing elastomers in the tyre industry will be detailed in chapter 2.

## 1.2 Hexafluorosilicic Acid

### 1.2.1 Generalities and production as by-product

Hexafluorosilicic acid (FSA), also known as fluorosilicic acid, is a hazardous waste by-product produced in the industrial wet synthesis of phosphate-containing fertilizers and, to a lesser extent, hydrofluoric acid. It is a strong acid that in aqueous solution generates $SiF_6^{2-}$ upon deprotonation (Eq.2 and 3). This species may in turn decompose either into $SiF_4$ and $F^-$ or further hydrolyses to $SiO_2$ (Eq.5), $H^+$ and $F^-$. The following reactions summarize the *equilibria* described so far.[10,11]

$$H_2SiF_6 \xrightarrow{\text{strong}} H^+ + HSiF_6^- \qquad \textbf{(Eq. 2)}$$

$$HSiF_6^- \underset{}{\overset{Ka_2 = 10^{-0.65}}{\rightleftharpoons}} SiF_6^{2-} + H^+ \qquad \textbf{(Eq. 3)}$$

$$SiF_6^{2-} \underset{}{\overset{K = 1 \cdot 10^{-6}}{\rightleftharpoons}} SiF_4 + 2\,F^- \qquad \textbf{(Eq. 4)}$$

$$SiF_6^{2-} + 2\,H_2O \underset{}{\overset{K = 1.2 \cdot 10^{-27}}{\rightleftharpoons}} SiO_2 + 4\,H^+ + 6\,F^- \qquad \textbf{(Eq. 5)}$$

It is a colourless and corrosive liquid with a sharp smell. Typical concentrations of commercial interest lie within the range of 20-35 % w/w. Higher concentrations are seldom seen, whilst its undiluted form is yet to be isolated. Table 1.1 reports the hazard and precautionary statements relative to FSA.

***Table 1.1*** *Hazard and precautionary statements relative to FSA.*

| | |
|---|---|
| **Hazard Statements** | H302-H311-H314 |
| **Precautionary Statements** | P280-P301 + P312 + P330-P303 + P361 + P353-P304 + P340 + P310-P305 + P351 + P338 |

### 1.2.2 FSA in the Phosphate Fertilizer Industry

As mentioned earlier, FSA is primarily produced by the phosphate fertilizer industry. These fertilizers are obtained by reacting fluorapatite with sulfuric acid according to equation 6:

$$2\,Ca_5F(PO_4)_3 + 7\,H_2SO_4 \longrightarrow 3\,Ca(H_2PO_4)_2 + 7\,CaSO_4 + 2\,HF \qquad (\textbf{Eq. } 6)$$

Then, two distinct reactions (Eq. 7 and 8) are possible:

$$Ca_5F(PO_4)_3 + 5\,H_2SO_4 \longrightarrow 3\,H_3PO_4 + 5\,CaSO_4 + HF \qquad (\textbf{Eq. } 7)$$

$$Ca_5F(PO_4)_3 + 7\,H_3PO_4 \longrightarrow 5\,Ca(H_2PO_4)_2 + HF \qquad (\textbf{Eq. } 8)$$

Unfortunately, fluorapatite contains various impurities, including $SiO_2$. It reacts with HF giving $H_2SiF_6$ (Eq.9), which in turn decomposes into $SiF_4$ yielding back HF (Eq.10):

$$SiO_2 + 6\,HF \longrightarrow H_2SiF_6 + 2\,H_2O \qquad (\textbf{Eq. } 9)$$

$$H_2SiF_6 \longrightarrow SiF_4 + 2\,HF \qquad (\textbf{Eq. } 10)$$

Finally, $SiF_4$ is collected *via* adsorptoion process with $H_2O$ in a scrubber, where further FSA is obtained.[12]

### 1.2.3 FSA in HF Industry

In the synthesis of HF, it has been estimated that about 50 kg of $H_2SiF_6$ are produced for every tonne of HF for the inevitable impurities of $SiO_2$ (Eq. 12) in the fluorspar ($CaF_2$) used as raw material.[2] The following reactions exemplify the parasitic reactions involved in the formation of $H_2SiF_6$.

$$CaF_2 + H_2SO_4 \longrightarrow 2\,HF + CaSO_4 \qquad (\textbf{Eq. } 11)$$

$$SiO_2 + 4\,HF \longrightarrow SiF_4 + 2\,H_2O \qquad (\textbf{Eq. } 12)$$

$$3\,SiF_4 + 2\,H_2O \longrightarrow 2\,H_2SiF_6 + SiO_2 \qquad (\textbf{Eq. } 13)$$

$$SiF_4 + 2\,HF \longrightarrow H_2SiF_6 \qquad (\textbf{Eq. } 14)$$

Eq. 11 describes the reaction exploited in the industrial production of HF, whereby fluorite and sulfuric acid react. Along with HF, $CaSO_4$ is also obtained. $SiO_2$ represents one of the major impurity in Acid Grade Fluospar with concentrations ranging from 0.5 to 1.5 %.[2]

Eq. 12 accounts for the formation of $SiF_4$ which may react either with water (Eq. 13) or with HF (Eq. 14) to give FSA. By examining Eq.12 and 14, it should be evident once again why FSA is such an economic burden for the industry. In Eq. 12, silica is shown to react with four equivalents of HF and, in doing so, it decreases the yield of HF. $SiF_4$ is then produced which in turn reacts with other two equivalents of HF further decreasing its yield. The environmental consequences are equally relevant. Given the hazardousness of FSA, its treatment and disposal should be carried out in suitable plants with proper stock facilities. At the same time, the demand of FSA as raw material is far lower than its supply resulting in a condition of surplus. Therefore, disposal at sea or in landfills of FSA-contaminated wastes still common practice.[13]

### 1.2.4 Uses and Emerging Importance as F e Si Source

*Per se*, $H_2SiF_6$ has a few direct uses. As fluorine source, water fluoridation (allowed only in some countries, such as Ireland, Canada, and the U.S.) is one of them with the aim of adjusting the content of fluorides to prevent tooth decay in the general population.[10] However, almost half of the production FSA is used the synthesis of fluorosilicates. These compounds are synthesized by neutralization

with a base or by reaction with a metal. The most important fluorosilicate is $Na_2SiF_6$ which is used in water fluoridation, as etching and polish agent for glass, in industrial laundries, and as microbicide. Other fluorosilicates include $(NH_4)_2SiF_6$, $K_2SiF_6$, and $BaSiF_6$.[2] It ought to be acknowledged that fluorosilicates are regarded as low value-added products. Low-density $AlF_3$ consumes approximately a quarter of the FSA market, but the process requires high-purity acid.[14]

A few processes in which hydrofluoric acid is recovered from FSA have been put forward. Among these, one consists in reacting $H_2SiF_6$ directly with $H_2SO_4$ while an alternative involves the formation of a fluosilicate intermediate *via* a metathesis reaction with a salt, generating HF upon heating. While appealing, such processes are difficult to scale up as they require expensive appliances specially made of corrosion-resistant materials. In fact, only five plants are producing HF from FSA worldwide to date.[13] Another example of direct use of FSA is represented in Pb electrorefining[2] whereas examples of its use in desilylation reactions in organic chemistry have been reported in the literature.[15]

FSA is also a silicon source, although a relatively limited number of studies has been reported in this sense. Dragičević and Hraste synthesized $SiO_2$ by neutralizing $H_2SiF_6$ with $NH_3$ and characterized the so-obtained product, with surface area values as high as 190 $m^2\ g^{-1}$.[16,17] Later, Yu *et al.* obtained highly pure precipitated silica *via* a two-step ammoniation synthesis. The reaction was studied over different ($NH_3/H_2SiF_6$) molar ratios to assess the best experimental conditions to obtain $SiO_2$ through this process. Surface areas value range from 27 to 160 $m^2\ g^{-1}$.[18]

Sodium silicate has also been used to obtain precipitated silica from FSA. Elineema *et al.* compared the properties of FSA-derived silica with that obtained from sulfuric acid at different temperature. Their study showed how the characteristics of the two silicas were fairly similar, with the interesting exception of surface area whose values were consistently higher in the FSA-derived samples.[12] Sarawade *et al.* obtained high specific surface area precipitated silica (up to 800 $m^2\ g^{-1}$) by neutralizing FSA with $Na_2CO_3$ keeping a fixed ratio of 1:3 of the two reactants. Their study also demonstrated how pH can affect superface area: carrying out the reaction under acidic conditions allowed to obtain silica with the highest surface area (800 $m^2\ g^{-1}$ for pH = 1)

whereas silica synthesized in a basic medium (pH = 10) feature lower surface area values, down to 200 $m^2$ $g^{-1}$.[19]

Finally, a couple of studies specifically addressed the synthesis of PS for tyre reinforcement from $H_2SiF_6$.[20,21] These will be discussed in Chapter 5.

In conclusion, as containing both F and Si, hexafluorosilicic acid is to be considered an interesting alternive source of both the elements. Recover and utilization of $H_2SiF_6$ fit well into the context of envisaging processes that may be both environmentally and economically sustainable, with the remarkable advantage of valorizing a low-cost hazardous waste in manufacturing more valuable and higher value-added products. Moreover, integrating the processes that generate and recover FSA in the same plant may bring about both relevant environmental benefits and more favourable economic outcomes in terms of developing a more "circular" local economy.

# References


[1] Grand View Research, Inc. Precipitated Silica Market Size, Share and Trends Analysis Report By Application, By Region, And Segment Forecasts, 2019-2025. https://www.grandviewresearch.com/industry-analysis/precipitated-silica-market.

[2] *Ullmann's Encyclopedia of Industrial Chemistry*; Wiley: 2000, ISBN: 9783527303854.

[3] Rouquerol, F.; Rouquerol, J.; Sing, K. In *Adsorption by Powders and Porous Solids*, Rouquerol, F., Rouquerol, J., Sing, K., Eds.; Academic Press: London, 1999, pp 165–189, ISBN: 978-0-12-598920-6, DOI: https://doi.org/10.1016/B978-012598920-6/50007-5.

[4] Rouquerol, F.; Rouquerol, J.; Sing, K. In *Adsorption by Powders and Porous Solids*, Rouquerol, F., Rouquerol, J., Sing, K., Eds.; Academic Press: London, 2014, pp 219–236, ISBN: 978-0-12-598920-6, DOI: https://doi.org/10.1016/B978-012598920-6/50009-9.

[5] Rouquerol, F.; Rouquerol, J.; Sing, K. In *Adsorption by Powders and Porous Solids*, Rouquerol, F., Rouquerol, J., Sing, K., Eds.; Academic Press: London, 1999, pp 191–217, ISBN: 978-0-12-598920-6, DOI: https://doi.org/10.1016/B978-012598920-6/50008-7.

[6] Iler, R. K., *The Chemistry of Silica*; Wiley: 1979, ISBN: 047102404X.

[7] In *Characterization and Chemical Modification of the Silica Surface*, Vansant, E., Voort, P. V. D., Vrancken, K., Eds.; Studies in Surface Science and Catalysis, Vol. 93; Elsevier: 1995, pp 59–77, DOI: https://doi.org/10.1016/S0167-2991(06)81511-9.

[8] Sears, G. W. Determination of Specific Surface Area of Colloidal Silica by Titration with Sodium Hydroxide. *Analytical Chemistry* **1956**, *28*, 1981–1983, DOI: https://doi.org/10.1021/ac60120a048.

[9] Reinhardt H. et al. Process for Hydrophobization of Finely Divided Silica and Silicates Using Prepolycondensed Organosilane., DE-AS 2-435-860.

[10] Urbansky, E. T. Fate of Fluorosilicate Drinking Water Additives. *Chemical Reviews* **2002**, *102*, 2837–2854, DOI: https://doi.org/10.1021/cr020403c.

[11] Ciavatta, L.; Iuliano, M.; Porto, R. Fluorosilicate Equilibria in Acid Solution. *Polyhedron* **1988**, *7*, 1773–1779, ISSN: 0277-5387, DOI: https://doi.org/10.1016/S0277-5387(00)80410-6.

[12] Elineema, G.; Kim, J. K.; Hilonga, A.; Shao, G. N.; Kim, Y.-N.; Quang, D. V.; Sarawade, P. B.; Kim, H. T. Quantitative Recovery of High Purity Nanoporous Silica from Waste Products of the Phosphate Fertilizer Industry. *Journal of Industrial and Engineering Chemistry* **2013**, *19*, 63–67, ISSN: 1226-086X, DOI: https://doi.org/10.1016/j.jiec.2012.07.001.

[13] Dahlke, T.; Ruffiner, O.; Cant, R. Production of HF from $H_2SiF_6$. *Procedia Engineering* **2016**, *138*, SYMPHOS 2015 - 3rd International Symposium on Innovation and Technology in the Phosphate Industry, 231–239, ISSN: 1877-7058, DOI: https://doi.org/10.1016/j.proeng.2016.02.080.

[14] Will, R. K. The Benefits of Isolating & Utilizing Fluorine from Phosphate Operations. *Procedia Engineering* **2016**, *138*, 267–272, DOI: https://doi.org/10.1016/j.proeng.2016.02.084.

[15] Pilcher, A. S.; Hill, D. K.; Shimshock, S. J.; Waltermire, R. E.; DeShong, P. Selective deprotection of trialkylsilyl ethers using fluorosilicic acid. *The Journal of Organic Chemistry* **1992**, *57*, 2492–2495, DOI: https://doi.org/10.1021/jo00034a057.

[16] T.Dragičević; Hraste, M. Particle Size Distribution of Silica Produced by Neutralization of Fluosilicic Acid. *Chem. Biochem. Eng.* **1993**, *7*, 89.

[17] T.Dragičević; Hraste, M. Surface Area of Silica Produced by Neutralization of Fluosilicic acid. *Chem. Biochem. Eng.* **1994**, *8*, 141–143.

[18] Yu, H. S.; Rhee, K.-I.; Lee, C. K.; Yang, D.-H. Two-Step Ammoniation of By-Product Fluosilicic Acid to Produce High Quality Amorphous Silica. *Korean Journal of Chemical Engineering* **2000**, *17*, 401–408, ISSN: 1975-7220, DOI: https://doi.org/10.1007/BF02706850.

[19] Sarawade, P.; Kim, J.; Hilonga, A.; Kim, H. T. Recovery of High Surface Area Mesoporous Silica from Waste Hexafluorosilicic Acid ($H_2SiF_6$) of Fertilizer Industry. *Journal of Hazardous Materials* **2009**, *173*, 576–580, DOI: https://doi.org/10.1016/j.jhazmat.2009.08.125.

[20] Hilonga Askwar and Kim, J.-K.; Sarawade, P. B.; Quang, D. V.; Shao Godlisten Namwel and Elineema, G.; Kim, H. T. Two-Step Rapid Synthesis of Mesoporous Silica for Green Tire. *Korean Journal of Chemical Engineering* **2012**, *29*, 1643–1646, ISSN: 1975-7220, DOI: https://doi.org/10.1007/s11814-012-0053-9.

[21] Nguyen, V.-H.; Vu, C.; Choi H.J.and Kien, B. Nanosilica Extracted from Hexafluorosilicic Acid of Waste Fertilizer as Reinforcement Material for Natural Rubber: Preparation and Mechanical Characteristics. *Materials* **2019**, *12*, 2707, DOI: https://doi.org/10.3390/ma12172707.

# 2 $SiO_2$ as a Reinforcing Agent for Tyres

## 2.1 Introduction

*This chapter introduces some basic information about tyres, trade compounds, vulcanization, and coupling agents. A summary on tyre performances in terms of rolling resistance, wear resistance, and wet skid resistance is then given. The concept of "magic triangle", a useful graphical representation of these properties, is also presented along with the effect of carbon black and silica as reinforcing agents.*

A tyre can be defined as a composite material made of several rubber components which are bound together. Nevertheless, it is a far more complex product than one could think. A tyre should be able to transfer efficiently engine power and brake forces onto the road for a comfortable and safe drive in both straights and curves and, in doing so, it should also feature essential characteristics, such as the maximum possible adhesion to road surfaces under all weather conditions, minimal rolling resistance, robustness, and longevity.[1]

Since their introduction in the 1880s, tyres have played a major role in the development of the modes of transport on road. Both natural and synthetic rubbers are used as raw materials in their production and almost half of the rubber produced in the world is used up by the tyre industry. *Per se*, rubber does not feature the characteristics of resiliency, strength, and wear-resistance needed to be directly used in tyres. For this reason, rubber undergoes a treatment named *vulcanization* which is instrumental in its strengthening. This process was serendipitously discovered by American chemist Charles Goodyear in 1839. While he was working on setting up a curing process, a mixture made of

rubber and sulfur accidentally fell on a hot stove and turned into a solid lump, instead of melting down.[2]

The reason why vulcanization strengthens rubber involves the heat-activated formation of cross-linking sulfur bridges between sections of the rubber polymeric chains (Figure 2.1). The chemistry behind this process is quite complex and the exact mechanism is only partially understood and still subject of debate. However, empirical observations have suggested that an ionic mechanism is more likely to be involved than a free-radical mechanism. In fact, it was observed that free-radical inhibitors and retarders do not have any effect on vulcanization rate whilst the opposite result was achieved when either organic acids, bases, or solvents with high dielectric constant were added.[3]

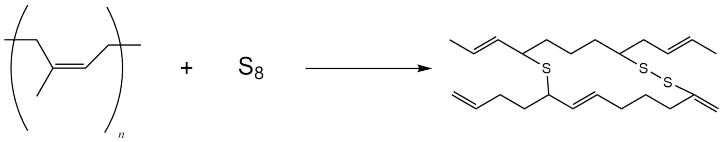


***Figure 2.1*** *A simplified representation of vulcanization of a natural rubber.*

To further enhance wear resistance, tensile strength and tear strength, carbon black was first introduced as a reinforcing agent in the beginning of the $20^{\text{th}}$ century.[4] Carbon black is a material obtained upon incomplete combustion of heavy petroleum products (*e.g.*, tars) and is considered as a form of "paracrystalline" carbon with a high surface-area-to-volume ratio.[5] Nowadays, the reinforcing properties of carbon black are complemented by adding apt amounts of silica into the tread compound. The use of $SiO_2$ is justified by the numerous advantages in terms of reduction in rolling resistance, and hence lower fuel consumption, as well as improved wet skid performance with enhanced braking and grip on snowy roads, allowing safer driving conditions.[6,7] However, given its hydrophilicity and low degree of physical and chemical binding with the rubber matrix, the addition of a coupling agent is needed to allow $SiO_2$ to serve as a reinforcing agent (*vide infra*).

## 2.2 Compounding Precipitated $SiO_2$ on Tread Compound

During the synthesis of precipitated silica for tyres, reinforcement potential strictly depends on primary particle size, which is fixed during the very first stages of the synthesis itself.[8] The precipitation parameters deemed to be involved in determining particle size are temperature, silicate ratio, reaction rate, reactant concentrations, and the presence of additives.[8,9] For example, lower temperatures lead to smaller particle sizes, using more concentrated reactants is linked with greater production of gel whereas slow rates of neutralization reduces gel formation.[8] Table 2.1 reports the specifications that precipitated $SiO_2$ should feature in order to act as a suitable reinforcing agent.[6]

***Table 2.1*** *Desired specifications for precipitated $SiO_2$ in tyre reinforcement.*

| Property | Range |
|---|---|
| **Surface Area** | 125 - 250 $m^2g^{-1}$ |
| **Free Water, loss @ 105 °C** | (6 ± 3) % |
| **pH** | 5 - 7 |
| **Bound Water** | (3 ± 0.5) % |
| **Salt Content** | (0.5 - 2.5) % |

Besides precipitation, post-synthesis operations such as milling, drying, and compaction also play an important part in determining silica behaviour in rubber. Table 2.2 summarizes the correlation between operations on silica and its behaviour in rubber.

***Table 2.2*** *Effect of synthesis and post-synthesis operations on the properties of precipitated $SiO_2$.*[6]

| Operation | Behaviour in Rubber |
|---|---|
| **Precipitation** | Reinforcement; Visible Dispersion |
| **Milling; Compaction; Drying** | Visible Dispersion; Dustiness |

Compared with carbon black, the most common filler for rubber, as-synthesized precipitated silica shows poorer performances only in regards to wear resistance: in fact, performances of tear and tensile strengths are

substantially superimposable. However, this finding, along with higher manufacturing costs, has confined silica production and consumption in the tyre industry to approximately 10 % that of carbon black.[8] Reinforcing precipitated silicas are usually classified taking into account surface area, structure, and surface activity as in the case of carbon black. Specific Surface area, along with particle shape, is undoubtedly the most important parameter in predicting reinforcement:[8,10] the higher the surface area the higher the degree of reinforcement. Usually, suitable surface area values for tyre reinforcement range from 125 to 250 $m^2$ $g^{-1}$ which correspond to primary particle sizes in the range 10 - 30 nm. Concerning its surface, silica is characterized by the presence of silanol and siloxane groups (section 1.1.3). Silanols are responsible for the typical hydrophylicity of $SiO_2$ and thus for the low affinity that silica show for rubber, justifying low wear resistance when compared to carbon black. Similarly, silanols also define silica structure by forming hydrogen bonds responsible for bonding individual particles to form clusters.[6]

In order to overcome the low affinity of silica for rubber, a coupling agent is needed. These agents are usually bifunctional organosilanes, which are mixed with rubber and carbon black to obtain the tread compound. During the mixing, the coupling agent will react following two different chemical pathways.

The favoured pathway consists in the bonding of the organosilane to the silica surface and is responsible for the improvement in the mechanical properties of the tread. This reaction is thought to decrease filler-filler interactions by lessening silica surface energy. Moreover, they are able to improve rubber-filler interactions *via* sulfur-mediated linkages.[11] The second occurs between the rubber matrix and the coupling agent *via* either a direct sulfur donation or the interactions between of the silane sulfur moiety and the rubber. This causes the untimely scorch of the tread compound, which is an undesired outcome with detrimental effects on tyre performance.[12]

## 2.3 Tyre Performances and Properties

### 2.3.1 Tread Compounds and the "Magic Triangle"

The main component of a tread compound is rubber, which be either natural or synthetic (polybutadiene or, more frequently, styrene-butadiene copolymers (SBR)). Fillers are added to improve the mechanical characteristics of the tyre

soon after vulcanization whereas oils and plastifiers are used to facilitate tread compound workability. Lastly, antioxidants are added to prevent ageing and improve grip.
Styrene-butadiene copolymers combine the properties of polybutadiene (high hysteresis which offers good wet grip properties) with the properties of polystyrene which, despite providing lower hysteresis and rolling resistance, enhances wear resistance. The ratio between the two monomers in SBR, with styrene content up to 25 %, is crucial in determining the grip and resistance properties of the final tyre. Table 2.3 exemplifies the behaviour of some of the components in a tread compound.

***Table 2.3*** *Behaviour of the main components in a tread compound.*

| Component | Rolling Resistance | Wet Skid Resistance |
|---|---|---|
| **Polybutadiene** | Excellent | Mediocre |
| **SBR 23.5 % styrene** | Medium | Good |
| **SBA 40 % styrene** | Mediocre | Excellent |
| **Carbon Black** | Very Good but decreases when increasing its content | Improves when increasing its content |
| **Oil** | Decreases when increasing the content | Increases when increasing its content |

The main features that characterize tyre performance are wear resistance, wet skid resistance, and rolling resistance. Often, these three properties are depicted on a graph that takes the form of a triangle. This graph is commonly referred as the "magic triangle" and is often useful when comparing the performances of different tyres. A simple example of such a representation is reported in figure 2.2. As will be shown further on, improvement in one of these properties often leads to the unwelcome decline of the other two parameters.

### 2.3.2 Rolling Resistance

Rolling resistance is defined as the force that opposes motion or, put in other terms, the force required to keep a tyre rolling. Hysteresis, the main responsible for rolling resistance, is the energy loss that a tyre suffers while rolling. This energy loss must be overcome by the vehicle's engine leading to higher fuel consumption. Mathematically, rolling resistance is calculated according to Eq. 2.1:

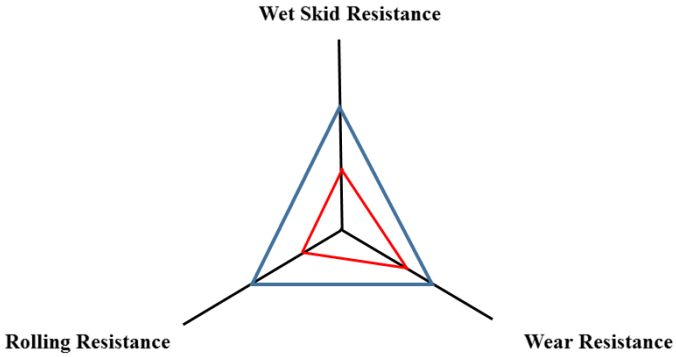


***Figure 2.2*** *Exemplifying magic triangles depicting the performances of two tyres.*

$$R_r = k_r W \tag{2.1}$$

where $R_r$ is the rolling resistance, $k_r$ is the rolling resistance constant, and $W$ is the weight of the vehicle.

Several factors affecting or featured by a given tread compound contribute to define its rolling resistance, including:

- drive style and road conditions;
- tread thickness and shape affect rolling resistance, with thicker and more contoured tread showing higher rolling resistance;
- nature of the rubber: natural rubber generally features lower rolling resistance than its synthetic counterparts;
- partial substitution of carbon black with silica allow to reduce rolling resistance (see par. 2.2).

Two standard procedures have been set up and by SAE (Society of Automotive Engineers) to assess tire rolling resistance, namely J1269 (carried out at fixed speed) and J2452 (carried out at different speeds).[13,14]

### 2.3.3 Wear Resistance

Wear is defined as the unavoidable loss of rubber occurring during the rolling and the sliding contact of a tyre with the road surface.[15] While the exact

mechanism whereby this *phenomenon* occurs in tyres is still subject of debate, it is widely acknowledged that wear resistance is strongly affected by the filler, in particular by its chemical nature, morphology, and surface characteristics.[11]
Given its hydrophobic nature, carbon black shows strong interactions with the rubber matrix. Rubber filled with relatively high-surface area carbon black provides high abrasion resistance performances. For example, Wang reported that the optimal surface area for a SBR/BR rubber with a loading of 65 phr* carbon black and 35 phr oil ranges from 130 to 150 $m^2g^{-1}$. However, higher surface area decreases wear resistance probably because of the increased interactions between carbon black particles at the expense of rubber-carbon black interactions.[11]
On the other hand, silica filling is considered detrimental to wear resistance if added into a tread compound without a proper coupling agent: in fact, silica-filled tires show very low wear resistance. Again, the turning point came with the discovery of sulfur-containing silane coupling agents such as TESPT (Figure 2.3),[16] allowing the partial replacement of carbon black and manufacturing tyres with performances substantially equal to the carbon black-filled only counterparts.

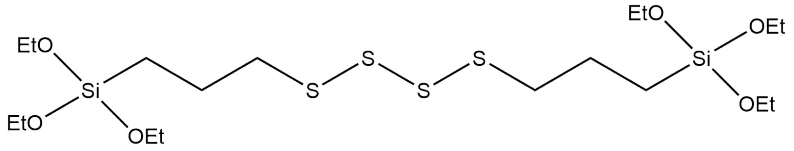


***Figure 2.3*** *Skeletal structural formula of Bis(triethoxysilylpropyl)tetrasulfide (TESPT).*

### 2.3.4 Wet Skid Resistance

Wet skid resistance (WSR) is the force developed when a tyre, prevented from rotating (*i.e.*, braking), slides on a wet road surface.[17] This parameter is particularly important when driving safety is concerned. As in rolling resistance and wear resistance, both rubber composition and filler(s) of choice contribute to determine WSR (actually, several factors are involved in WSR but, nonetheless, the attention will be focused only on the effect of fillers for the sake of brevity). Addition of silica into a tread compound positively affects WSR performances,

*phr is a measurement unit commonly used in rubber chemistry to quantify the amount of a given component in a tread compound. The acronym stands for Parts per Hundred Rubber.

having values of tan $\delta$ (the ratio of the loss modulus to the storage modulus)[18] comparable with an analogous carbon black-filled compound at low temperature. Tan $\delta$ is also referred as V/E ratio (*i.e.*, the viscous quality divided by the elastic quality) and, as such, is a dimensionless parameter. Tan $\delta$ is usually high in the uncured state and low in the cured state and it is related to the processability of rubber in its uncured state. This ratio relates to heat buildup (hysteresis) and inversely relates to rebound (resiliency) for rubber in the cured state.[19]

However, the most striking advantage of $SiO_2$ over carbon black consists in obtaining a good balance between rolling and wet skid resistance.[20] although carbon black performs better in dry conditions.[21]

Friction is at the root of WSR and is defined as the force of resistance to the relative motion of two contacting surfaces. Mathematically, friction (F) is defined in Eq. 2.2 as follows:

$$F = \mu N \tag{2.2}$$

where $\mu$ is the friction constant and $N$ the normal reaction force.

In sliding rubber-made materials, frictional energy dissipation is due to the aforementioned phenomenon of hysteresis with almost negligible permanent deformation.[21] In a laboratory setting, WSR of a tread compound is usually assessed by means of a British Portable Skid Tester (BPST). As for the tyre as whole, a standard ASTM method (E274/E274M) is available to gauge skid resistance both in dry and wet road conditions, although national and supranational authorities for driving safety may establish additional procedures and/or parameters for the assessment.[22]

# References


[1] Leister, G., *Passenger Car Tires and Wheels: Development - Manufacturing - Application*, 1st ed.; Springer International Publishing: 2018, ISBN: 978-3-319-50117-8.

[2] Stephens, H. L. In *Rubber Technology*, Morton, M., Ed.; Springer Netherlands: Dordrecht, 1999, pp 20–58, ISBN: 978-94-017-2925-3, DOI: https://doi.org/10.1007/978-94-017-2925-3_2.

[3] Oae, S., *Organic Sulfur Chemistry : Structure and Mechanism*; CRC revivals; CRC Press: 2018, ISBN: 978-1-351-07527-5.

[4] Blow, C.; Hepburn, C., *Rubber Technology and Manufacture*; Plastics and Rubber Institute: London, 1982, DOI: https://doi.org/10.1002/pol.1983.130210620.

[5] International Carbon Black Association What is Carbon Black. https://web.archive.org/web/20070821070137/http://www.carbon-black.org/what_is.html.

[6] Hewitt, N., *Compounding Precipitated Silica in Elastomers*; Plastics Design Library; William Andrew Publishing: Norwich, NY, 2007, ISBN: 978-0-8155-1528-9, DOI: https://doi.org/10.1016/B978-0-8155-1528-9.50022-9.

[7] Derham, C.; Newell, R.; Swift, P. Use of Silica for Improving Tread Grip in Winter Tyres. *NR Technol.* **1988**, *19*, 1–9.

[8] Hewitt, N.; Ciullo, P., *Compounding Precipitated Silica in Elastomers: Theory and Practice*; Plastics Design Library; Elsevier Science: 2007, ISBN: 9780815516538.

[9] Brinker, C. J.; Scherer, G. W., *Sol-Gel Science*; Academic Press: San Diego, 1990, pp 786–837, ISBN: 978-0-08-057103-4, DOI: https://doi.org/10.1016/B978-0-08-057103-4.50018-0.

[10] Rueby, J. In *VKRT Seminar*, 2019.

[11] Wang, M.-J. Effect of Filler-Elastomer Interaction on Tire Tread Performance Part III. Effects on Abrasion. https://www.kgk-rubberpoint.de/wp-content/uploads/migrated/paid_content/artikel/740.pdf.

[12] Brinke, J.; Debnath, S.; Reuvekamp, L.; Noordermeer, J. Mechanistic aspects of the role of coupling agents in silica–rubber composites. *Composites Science and Technology* **2003**, *63*, 1165–1174, DOI: https://doi.org/10.1016/S0266-3538(03)00077-0.

[13] Hall, D. E.; Moreland, J. C. Fundamentals of Rolling Resistance. *Rubber Chemistry and Technology* **2001**, *74*, 525–539, DOI: https://doi.org/10.5254/1.3547650.

[14] Society of Automotive Engineers Standard Collections. https://www.sae.org/standards/.

[15] Klüppel, M. In *Encyclopedia of Polymeric Nanomaterials*, Kobayashi, S., Müllen, K., Eds.; Springer Berlin Heidelberg: Berlin, Heidelberg, 2021, pp 1–6, ISBN: 978-3-642-36199-9, DOI: 10.1007/978-3-642-36199-9_312-1.

[16] *The Science and Technology of Rubber Fourth Edition*, Fourth Edition; Mark, J. E., Erman, B., Roland, C. M., Eds.; Academic Press: Boston, 2013, ISBN: 978-0-12-394584-6, DOI: https://doi.org/10.1016/B978-0-12-394584-6.00015-7.

[17] National Research Council (U.S.), *Skid resistance*; National Cooperative Highway Research Program Reports; Highway Research Board: 1972.

[18] Perkin Elmer Characterization of Car Tire Rubber. https://www.perkinelmer.com/lab-solutions/resources/docs/APP_007771B_15_Characterization_of_Car_Tire_Rubber.pdf.

[19] Dick, J., *Basic Rubber Testing: Selecting Methods for a Rubber Test Program*; ASTM Manual Series MNL 39; ASTM: 2003, ISBN: 9780803133587.

[20] Muramatsu, R.; Takahashi, H. Materials Technology for Reducing Rolling Resistance. *International Polymer Science and Technology* **2001**, *28*, 47–53, DOI: https://doi.org/10.1177/0307174X0102800514.

[21] Wang, M.-J.; Kutsovsky, Y. Effect of Fillers on Wet Skid Resistance of Tires. Part II: Experimental Observations on Effect of Filler-Elastomer Interactions on Water Lubrication. *Rubber Chemistry and Technology* **2008**, *81*, 576–599, DOI: https://doi.org/10.5254/1.3548221.

[22] ASTM Standard Test Method for Skid Resistance of Paved Surfaces Using a Full-Scale Tire.
http://www.astm.org/cgi-bin/resolver.cgi?E274E274M.

# 3 Ordered Siliceous Mesoporous Materials

*Chapter 3 is devoted to introducing ordered silicon-based mesoporous materials, an interesting family of materials with a variety of potential application in a wide range of fields. The concepts of self-assembly, soft templating, the description of the interactions between surfactant, Si-containing species, and other possible reactants are introduced. Lastly, a brief summary concerning the alternative silicon sources investigated in the literature to replace Si-alkoxides in the synthesis of these materials is presented.*

## 3.1 History and Background

Ordered siliceous mesoporous materials are a relatively new class inorganic of Si-containing materials which have attracted considerable attention from the scientific community. The reason of this interest is linked to the peculiar features they possess. Among them, large surface areas and regular zeolite-like open-pore structures certainly stand out. In these materials pore sizes range from 2 up to 50 nm, in between micro- and macropores, hence the name mesoporous materials. They have been thoroughly investigated for applications such as chromatography, environmental remediation, sensors, drug delivery, and catalyst supports[1] as reported in figure 3.1.

M41S family materials were the first to be synthesized and characterized in 1992 by a group of scientists at Mobile Corporation.[2] This family of materials is composed of three members with different symmetries. MCM-41* was the first to

*The acronym MCM stands for *Mobil Composition Matter*.

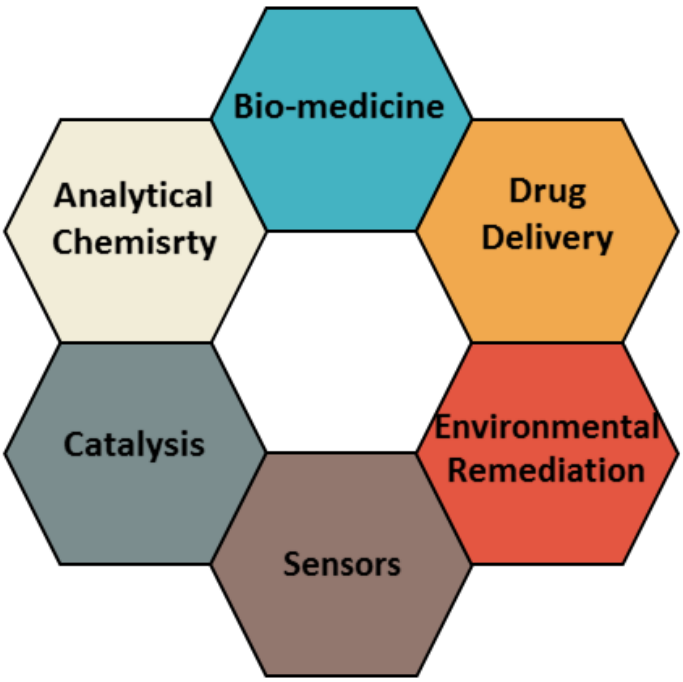


***Figure 3.1*** *Possible applications of mesoporous materials.*

be synthesized and has been the most studied among the three. Its symmetry group is *p6mm*, given the hexagonal packing of the channels. MCM-48 features a cubic bicontinuous structure ($Ia\bar{3}d$) symmetry generated by two interwoven networks of mesochannels. Lastly, MCM-50 is a laminar phase characterized by a planar (*p2*) symmetry and it is thought to be the least stable of the group. Graphical representations of these phases are given in Figure 3.2.

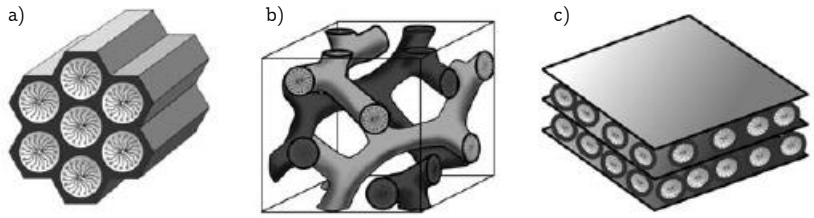


***Figure 3.2*** *M41S family: a) MCM-41 (hexagonal, p6mm), b) MCM-48 (cubic, $Ia\bar{3}d$), c) MCM-50 (planar, p2). Adapted from Hoffman et al.[3]*

The fabrication of mesoporous materials consists in building a long-range ordered array of apt sized pores.To do this, the synthesis of such materials require a scaffold generated by self-assembling molecules (called either structure-directing (SDAs) or simply templating agents), upon which a siliceous precursor (typically TEOS or TMOS) can first interact with and then

polymerize, as described in Eq. 15, 16, and17.

$$\equiv\mathrm{Si}-\mathrm{OR} + \mathrm{H_2O} \overset{\text{hydrolysis}}{\rightleftharpoons} \equiv\mathrm{Si}-\mathrm{OH} + \mathrm{ROH} \qquad (\textbf{Eq. } 15)$$

$$\equiv\mathrm{Si}-\mathrm{OH} + \mathrm{HO}-\mathrm{Si}\equiv \overset{\text{water cond}\cdot}{\rightleftharpoons} \equiv\mathrm{Si}-\mathrm{O}-\mathrm{Si}\equiv + \mathrm{H_2O} \qquad (\textbf{Eq. } 16)$$

$$\equiv\mathrm{Si}-\mathrm{OR} + \mathrm{HO}-\mathrm{Si}\equiv \overset{\text{alcohol cond}\cdot}{\rightleftharpoons} \equiv\mathrm{Si}-\mathrm{O}-\mathrm{Si}\equiv + \mathrm{ROH} \qquad (\textbf{Eq. } 17)$$

SDAs are usually organic molecules whose spontaneous assembling is driven by minimizing interface energy, which is the driving force of the self-assembly. Upon preliminary formation of spherical micelles, the development of the final silica/surfactant composite comes about by following two different mechanisms: the true liquid-crystal templating mechanism (TLCT) and the so-called cooperative liquid-crystal templating mechanism (CLCT). The former consists in the formation of a liquid-crystalline phase when the surfactant concentration is sufficiently high under given conditions of pH and temperature; this happens regardless of the precursor presence. The latter, instead, may occur at lower SDA concentration and involves the cooperative self-assembly of the templating agent in the presence of already condensed precursor.[3–5] This method of obtaining a mesoporous material is often referred to as "soft-templating approach". Once synthesized the organic/inorganic composite, it is possible to obtain the mesoporous material by calcination, extraction, microwave treatment, chemical and/or physical oxidation, *etc.*[1] A schematization of the formation of MCM-41 is reported in figure 3.3 as an example of the two process involved in the formation of a mesoporous material.

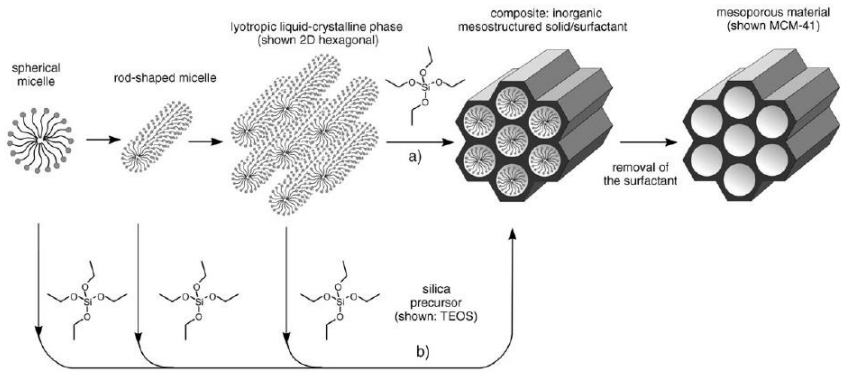


***Figure 3.3*** *Soft-templating approach for the synthesis of MCM-41. Adapted from Hoffman et al.[3]*

## 3.2 Interactions Involved in Obtaining Mesoporous Siliceous Materials

Depending on the nature of the surfactant, precursor, pH and ionic species in the reaction mixture, at least nine possible soft-template interactions exist and six of them are relevant to obtaining ordered mesoporous siliceous materials.[1]
The first interaction involves Coulumb interactions between a cationic surfactant (S) (e.g., CTAB) and an anionic silicate precursor (I) in a basic *medium* is classified as $S^+I^-$: this is the interaction that leads to the formation M41S family of materials.[2]
Another interaction mediated by Coulumb forces under basic conditions is $S^-N^+I^-$, *viz.* the interaction between an anionic surfactant is mediated by a cationic amino group of molecules such as TMAPS or APS. ASM-n materials are obtained through this mechanism.[6]
Interaction $S^+X^-I^+$ is possible in an acidic *medium*, whereby the surfactant interacts with an anionic species that in turn interact with a positively charged Si-precursor. SBA-1, SBA-2, and SBA-3 are materials synthesized in this manner.[7]
The mechanism accounting for the formation of SBA-15 and related materials is explained by the interaction of four species ($S^0H^+X^-I^+$) under very acidic conditions, where S is a triblock copolymer such as Pluronic 127.[8]
Peculiar but minor forms of interaction are $S^+$-$I^-$, which involves a covalent rather then a electrostatic bond between surfactant and inorganic precursor,[9] and the H-bond driven interaction $S^0I^0$.[1] A summary with a brief description of these interactions is reported in Table 3.1.

***Table 3.1*** *Typical interactions involved in obtaining mesoporous $SiO_2$. Readapted from Zhao*[1]

| Mechanism | Interactions | Medium | Products |
|---|---|---|---|
| $\mathbf{S^+I^-}$ | Electrostatic Coulomb Forces | Basic | M41S |
| $\mathbf{S^-N^+I^-}$ | Electrostatic Coulomb Forces | Basic | AMS-n |
| $\mathbf{S^+X^-I^+}$ | Electrostatic Coulomb forces, H-bonds | Acidic | SBA-1 SBA-2 SBA-3 |
| $\mathbf{S^+\text{-}I^-}$ | Covalent Bond | Basic | Other mesoporous $SiO_2$ |
| $\mathbf{S^0I^0}$ | H-bonds | Neutral | Disordered worm-like mesoporous $SiO_2$; HMS, MSU |

***Legend:*** ***S*** *surfactant,* ***I*** *silicate species,* ***N*** *cationic amino group belonging to TMAPS or APS,* $\boldsymbol{X^-}$ *anionic species.*

## 3.3 Tuning Mesophases

As stated in the previous section, mesostructures are strongly affected by usually noncovalent organic-inorganic interactions among the species involved in their formation. These interactions are responsible for the coming into being of the ordered liquid-crystal mesophase set up by surfactant molecules. This liquid-crystal phase is often obtained by using amphiphilic surfactants whose molecules, as it is widely known, feature both hydrophilic and hydrophobic groups known as "heads" and "tails", respectively. In aqueous solution, they self-assemble leading to the formation ordered mesostructures of various morphologies called micelles which can be classified as lamellar, bicontinuous, mesh, columnar, and globular.[1]

Packing parameter of ionic surfactants ($g$) may be considered as a variable useful to foresee the final mesostructure generated by a given surfactant.[10] The $g$ value is calculated as it follows (Eq. 3.1):

$$g = \frac{V}{a_0 l} \tag{3.1}$$

where $V$ is the total volume hydrophobic chains plus any cosolvent organic molecules between them, $a_0$ is the effective hydrophilic contribution of the head

group at the water/micelle interface, while $l$ is the kinetic surfactant tail length. As far as cationic surfactants are concerned, when $g < 1/3$, spherical micelles are obtained leading to cubic and 3D hexagonal mesophase while, when $1/3 < g < 1/2$, a 2D hexagonal ($p66m$) mesophase, typical of MCM-41, is come by. The scaffold needed in the syntheis of MCM-48 (cubic mesophase, $Ia\bar{3}d$ symmetry group) is set up by 3D cylindrical micelles; $g$ values lie within the range 1/2 and 2/3 in this case. Finally, lamellar structures (MCM-50) are obtained when $g$ value is approximately 1 while $g > 1$ brings about the formation of reversed micelles. However, it ought to be acknowledged that specific arrangements of the surfactant molecules and the final mesostructure symmetry are highly dependent on reaction conditions by which the mesostructures are synthesized. Nevertheless, a few rules of thumb can be given to rationalize how different experimental conditions affect the final mesostructure. For example, the use of bulkier hydrophilic heads leads to a decrease in the value of $g$ with more spherical mesostructures. Conversely, two surfactant featuring the same $a_0$ value but different (single and double) tails differ for the $g$ value: the packing value for the double-tailed one is usually twice as large as the one-tailed. Therefore, formation of bilayers is more favoured in the case of double-tailed surfactant.[11]

Adding an organic additive into the reaction mixture also affects the properties of the surfactant micelles. Small organic solvent molecules usually will be located near the water/micelle interface whereas larger molecules are situated nearby the core. One feature commonly affected is pore dimension which usually results to be larger. Adding inorganic salts reduce head-group repulsions, causing an increase of $g$ value. The effect depends on the ionic radii of the ions added.[1,12]

## 3.4 Mesopostructured Materials from Alternative Silicon Sources

The history of the sol-gel process is intertwined with silicon alkoxides ($[Si(OR)_4]$), such as TEOS ($[Si(OC_2H_5)_4]$) and TMOS $[Si(OCH_3)_4]$. These synthetic precursors are widely used to obtain mesostructured materials, with the former resulting preferred in virtue of its lower toxicity and price.

Their use allows to obtain regular and tunable mesostructured materials in a variety of experimental conditions.[11] However, the use of these alkoxide on a large scale is problematic given their relatively high cost and toxicity. Therefore,

research has been focusing on finding alternative precursors in the framework of a greener approach to the synthesis of mesostructured silica. These alternatives investigated can be classified as either natural or waste-generated.

### 3.4.1 Alternative Natural Silica Sources

A natural silica source is defined as a non-toxic Si-containing mineral that is readily employed as a reagent in the synthesis of mesostructured $SiO_2$.[13] Talc,[14] kaolin,[15], and bentonite[16] are examples of natural clays that have been successfully investigated in this sense.[13] Other interesting natural precursors are zeolites, diatomaceous earth and other Si-containing minerals.[17] However, although their relative inexpensiveness and abundance are attractive features, problems in polymerization control and narrow experimental conditions may limit their applicability.[13] Environmental issues related to their extraction are also of concern.

### 3.4.2 Alternative Waste-derived Silica Sources

Waste-derived $SiO_2$ sources represent an alluring alternative to silicon alkoxide with the major advantage of recovering otherwise toxic, low value-added and/or useless by-products. E-waste is a growing environmental problem but can be also a source of raw materials. Among these, electronic packaging resins may be an alternative source of Si in the synthesis of mesostructured $SiO_2$ as demonstrated by Liou in his seminal work.[18] Rice husk, the outer covering of the rice grain, is an agricultural waste with a content of silica up to 25 %, which increases up to 90 % after combustion. A variety of mesostructures have been obtained by using the sodium silicate solution derived from rice husk including SBA-15, MCM-41, Al-MCM-41 and MCM-48, used later in a variety of applications.[13,19,20]

Another important source of silica from waste are fly ash and bottom ash, which are by-products of coal power plants for electricity production. Bottom ash is the heavier fraction of the particles that are not able to ascent dragged by the flow of the flue gases. Intsead, fly ash is lighter and, then, able to rise. Usually, ash is reacted with NaOH at around 500 °C for 1 h, cooled at room temperature, and milled. The so-obtained powder is then dissolved in water and aged for at

least one day. The sodium silicate-rich suspension is subsequently filtered which, upon reaction with an apt tamplating agent and hydrothermal treatment, yields a range of $SiO_2$-based mesostructured materials, including MCM-41, Al-MCM-41, Al-MCM-48, SBA-15, and SBA-16.[13,21–24]

Hexafluorosilicic acid (FSA, see section 1.2) is another interesting silicon source for the synthesis of mesostructured silica. However, few examples are reported in the literature. Jeong *et al.*[25] first synthesized MCM-41 and Al-MCM-41 from FSA and thoroughly characterized these materials while, a few years later, Liu *et al.*[26] synthesized Ti-MCM-41 from FSA to be used as an epoxidation catalyst. Lastly, Jin *et al.*[27] managed to obtain ZSM-5, an aluminosilicate zeolite with relevant applications in the petroleum industry as a heterogeneous catalyst.

Waste material-derived mesostructures feature similar characteristics to those derived from alkoxide with the exception of surface area, for which low or slightly lower values have been reported.[13]

# References

[1] Zhao, D.; Wan, Y.; Zhou, W., *Ordered Mesoporous Materials*; Wiley: 2013, ISBN: 9783527326358.

[2] Kresge, C.; Leonowicz, M.; Roth, W.; Vartuli, J.; Beck, J. Ordered Mesoporous Molecular Sieves Synthesized by Liquid-Crystal Template Mechanism. *Nature* **1992**, *359*, 710–712, DOI: https://doi.org/10.1038/359710a0.

[3] Hoffmann, F.; Cornelius, M.; Morell, J.; Fröba, M. Silica-Based Mesoporous Organic–Inorganic Hybrid Materials. *Angewandte Chemie (International ed. in English)* **2006**, *45*, 3216–3251, DOI: https://doi.org/10.1002/anie.200503075.

[4] Attard, G. S.; Glyde, J. C.; Göltner, C. G. Liquid-Crystalline Phases as Templates for the Synthesis of Mesoporous Silica. *Nature* **1995**, *378*, 366–368, DOI: https://doi.org/10.1038/378366a0.

[5] Monnier, A.; Schütha, F.; Huo, Q.; Kumar, D.; Margolese, D.; Maxwell, R. S.; Stucky, G. D.; Krishnamurty, M.; Petroff, P.; Firouzi, A.; Janicke, M.; Chmelka, B. F. Cooperative Formation of Inorganic-Organic Interfaces in the Synthesis of Silicate Mesostructures. *Nature* **1993**, *261*, 1299–1303, DOI: https://doi.org/10.1126/science.261.5126.1299.

[6] Che, S.; Garcia-Bennett, A. E.; Yokoi, T.; Sakamoto, K.; Kunieda, H.; Terasaki, O.; Tatsumi, T. A novel Anionic Surfactant Templating Route for Synthesizing Mesoporous Silica with Unique Structure. *Nature Materials* **2003**, *2*, 801–805, DOI: https://doi.org/10.1038/nmat1022.

[7] Huo, Q.; Margolese, D. I.; Ciesla, U.; Feng, P.; Gier, T. E.; Sieger, P.; Leon, R.; Petroff, P. M.; Schüth, F.; Stucky, G. D. Generalized Synthesis of Periodic Surfactant/Inorganic Composite Materials. *Nature* **1994**, *368*, 317–332, DOI: https://doi.org/10.1038/368317a0.

[8] Zhao, D.; Feng, J.; Huo, Q.; Melosh, N.; Fredrickson, G. H.; Chmelka, B. F.; Stucky, G. D. Triblock Copolymer Syntheses of Mesoporous Silica with Periodic 50 to 300 Ångstrom Pores. *Science* **1998**, *279*, 548–552, ISSN: 0036-8075, DOI: https://doi.org/10.1126/science.279.5350.548.

[9] Shimojima, A.; Kuroda, K. Direct Formation of Mesostructured Silica-Based Hybrids from Novel Siloxane Oligomers with Long Alkyl Chains. *Angewandte Chemie International Edition* **2003**, *42*, 4057–4060, DOI: https://doi.org/10.1002/anie.200351419.

[10] Huo, Q.; Margolese, D. I.; Stucky, G. D. Surfactant Control of Phases in the Synthesis of Mesoporous Silica-Based Materials. *Chemistry of Materials* **1996**, *8*, 1147–1160, DOI: https://doi.org/10.1021/cm960137h.

[11] Brinker, C. J.; Scherer, G. W., *Sol-Gel Science*; Academic Press: San Diego, 1990, pp 786–837, ISBN: 978-0-08-057103-4, DOI: https://doi.org/10.1016/B978-0-08-057103-4.50018-0.

[12] Leontidis, E. Hofmeister anion effects on surfactant self-assembly and the formation of mesoporous solids. *Current Opinion in Colloid and Interface Science* **2002**, *7*, 81–91, ISSN: 1359-0294, DOI: https://doi.org/10.1016/S1359-0294(02)00010-9.

[13] Gérardin, C.; Reboul, J.; Bonne, M.; Lebeau, B. Ecodesign of Ordered Mesoporous Silica Materials. *Chem. Soc. Rev.* **2013**, *42*, 4217–4255, DOI: https://doi.org/10.1039/C3CS35451B.

[14] Yang, H.; Du, C.; Jin, S.; Tang, A.; Li, G. Enhanced Photoluminescence Property of $SnO_2$ Nanoparticles Contained in Mesoporous Silica Synthesized with Leached Talc as Si Source. *Microporous and Mesoporous Materials* **2007**, *102*, 204–211, ISSN: 1387-1811, DOI: https://doi.org/10.1016/j.micromeso.2006.12.031.

[15] Du, C.; Yang, H. Investigation of the Physicochemical Aspects from Natural Kaolin to Al-MCM-41 mesoporous materials. *Journal of Colloid and Interface Science* **2012**, *369*, 216–222, ISSN: 0021-9797, DOI: https://doi.org/10.1016/j.jcis.2011.12.041.

[16] Yang, H.; Deng, Y.; Du, C.; Jin, S. Novel Synthesis of Ordered Mesoporous Materials Al-MCM-41 from Bentonite. *Applied Clay Science* **2010**, *47*, 351–355, ISSN: 0169-1317, DOI: https://doi.org/10.1016/j.clay.2009.11.050.

[17] Fowler, C. E.; Hoog, Y.; Vidal, L.; Lebeau, B. Mesoporosity in Diatoms via Surfactant Induced Silica Rearrangement. *Chemical Physics Letters* **2004**, *398*, 414–417, ISSN: 0009-2614, DOI: https://doi.org/10.1016/j.cplett.2004.09.102.

[18] Liou, T.-H. A Green Route to Preparation of MCM-41 Silicas with Well-ordered Mesostructure Controlled in Acidic and Alkaline Environments. *Chemical Engineering Journal* **2011**, *171*, Special Section: Symposium on Post-Combustion Carbon Dioxide Capture, 1458–1468, ISSN: 1385-8947, DOI: https://doi.org/10.1016/j.cej.2011.05.074.

[19] Chumee, J.; Grisdanurak, N.; Neramittagapong, S.; Wittayakun, J. Characterization of AlMCM-41 Synthesized with Rice Husk Silica and Utilization as Supports for Platinumiron Catalysts. *Brazilian Journal of Chemical Engineering* **2009**, *26*, 367–373, ISSN: 0104-6632.

[20] Bhagiyalakshmi, M.; Yun, L. J.; Anuradha, R.; Jang, H. T. Utilization of Rice Husk Ash as Silica Source for the Synthesis of Mesoporous Silicas and their Application to $CO_2$ Adsorption through TREN/TEPA Grafting. *Journal of Hazardous Materials* **2010**, *175*, 928–938, ISSN: 0304-3894, DOI: https://doi.org/10.1016/j.jhazmat.2009.10.097.

[21] Chang, H.-L.; Chun, C.-M.; Aksay, I. A.; Shih, W.-H. Conversion of Fly Ash into Mesoporous Aluminosilicate. *Industrial & Engineering Chemistry Research* **1999**, *38*, 973–977, DOI: https://doi.org/10.1021/ie980275b.

[22] Hui, K.; Chao, C. Synthesis of MCM-41 from Coal Fly Ash by a Green Approach: Influence of Synthesis pH. *Journal of Hazardous Materials* **2006**, *137*, 1135–1148, ISSN: 0304-3894, DOI: https://doi.org/10.1016/j.jhazmat.2006.03.050.

[23] Chandrasekar, G.; Ahn, W.-S. Synthesis of Cubic Mesoporous Silica and Carbon Using Fly Ash. *Journal of Non-Crystalline Solids* **2008**, *354*, 4027–4030, ISSN: 0022-3093, DOI: https://doi.org/10.1016/j.jnoncrysol.2008.06.011.

[24] Chandrasekar, G.; Son, W.-J.; Ahn, W.-S. Synthesis of Mesoporous Materials SBA-15 and CMK-3 from Fly Ash and Their Application for $CO_2$ Adsorption. *Journal of Porous Materials* **2009**, *16*, 545–551, ISSN: 1573-4854, DOI: https://doi.org/10.1007/s10934-008-9231-x.

[25] Jeong, S.-Y.; Suh, J.-K.; Lee, J.-M.; Kwon, O.-Y. Preparation of Silica-Based Mesoporous Materials From Fluorosilicon Compounds: Gelation of $H_2SiF_6$ in Ammonia Surfactant Solution. *Journal of Colloid and Interface Science* **1997**, *192*, 156–161, ISSN: 0021-9797, DOI: https://doi.org/10.1006/jcis.1997.4974.

[26] Liu, T.; Jin, F.; Wang, X.; Fan, Y.; Yuan, M. Synthesis of Titanium Containing MCM-41 from Industrial Hexafluorosilicic Acid as Epoxidation Catalyst. *Catalysis Today* **2017**, *297*, Catalytic science and technology in Sustainable Environment II (EECAT 2016), 316–323, ISSN: 0920-5861, DOI: https://doi.org/10.1016/j.cattod.2017.03.011.

[27] Jin, F.; Wang, X.; Liu, T.; Xiao, L.; Yuan, M.; Fan, Y. Synthesis of ZSM-5 with the Silica source from Industrial Hexafluorosilicic Acid as Transalkylation Catalyst. *Chinese Journal of Chemical Engineering* **2017**, *25*, 1303–1313, ISSN: 1004-9541, DOI: https://doi.org/10.1016/j.cjche.2016.11.004.

# 4

# $H_2S$ removal and Mesostructured $SiO_2$-based Sorbent Materials

*After giving a brief outlook about liquid fossil fuels and coal, this chapter delves into the topic of $H_2S$ removal from sour syngas. In particular, it details about the mainstream integrated gasification combined cycle (IGCC) systems and proceeds with providing particulars about the possible utilization of mesostructured sorbents for this purpose.*

## 4.1 Liquid Fossil Fuels: An Energy Outlook

The increasing demand of energy required to sustain the current economic development has compelled the scientific community to find alternatives to liquid fossil fuels, the commonest sources of energy to date. However, despite being high in demand, liquid fossil fuels are not renewable and finding new easily exploitable, and thus economically sustainable, oil wells has become more and more arduous.[1]

Renewable (may it be in the form of solar, wind, hydroelectric, biomass, geothermal, *etc.*) and nuclear energy represent the most promising long-term alternative to liquid fossil fuels. The former, however, are unfortunately expensive and would take several years to be aptly implemented and be cost-effective. Moreover, their energy output may not be steady in every given circumstance or may even be utterly unpredictable. As for nuclear energy, despite being relatively cost-effective *per se* with a steady energy output, its full development is severely thwarted by the high upfront expenses to be sustained,

the environmental concerns about uranium extraction,* burdensome long-term management of radioactive waste, questionable intrinsic safety of nuclear plants, and the vocal opposition of part of the public opinion.[2]

In this catch-22 situation, where conventional liquid and gaseous fossil fuels are to be abandoned but with reliable, cost-effective, and environmental-friendly alternatives still far from being economically sustainable, other alternative fossil sources, albeit non-renewable themselves, have been recently regarded as alluring solutions in short- and mid-term energetic scenarios, given their relatively lower cost and easier accessibility. These energy fossil sources include oil shale, tar sands, heavy crude, and coal.

## 4.2 Coal: Energy Source and Technology

Coal is the most uniformly distributed fossil energy source and is widely available worldwide. In this sense, coal may be considered as a strategic commodity, unaffected by the typical oil and gas price fluctuations during international crises. However, its composition is characterized by non-negligible amounts of N and S with potential polluting effects on the environment. Nevertheless, such high is the interest in coal as an energy source that several clean coal technologies have been come up to overcome its environmental drawbacks. Among these technology, gasification is of particular relevance inasmuch as allows both power generation (such as in IGCC power plants, *vide infra*) and hydrogen, a pivotal commodity in the chemical industry.[3,4]

### 4.2.1 Integrated Gasification Combined Cycle Systems (IGCC)

IGCC systems consist in gasifying coal or other fossil fuels at high pressure. By reacting it with either steam, oxygen or air, a gas (known as syngas) is eventually produced which is then purified from pollutants and particulates before being conveyed into a gas turbine. The hot gas from the gas turbine exhaust flows through a waste recovery system. The resulting steam sets in

*a non-renewable energy source itself

motion a steam turbine, producing electricity. A simplified process flow of IGCC system is depicted in Figure 4.1.

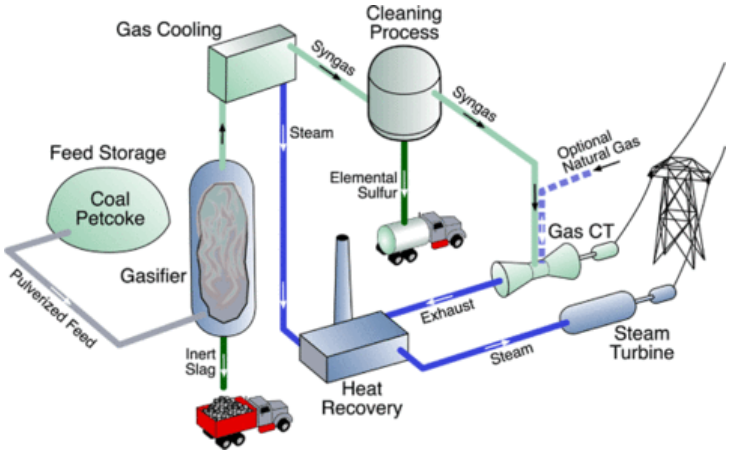


***Figure 4.1*** *Simplified flow chart of the IGCC process.*[5]

The chemical composition of the so-obtained fuel gas is directly related to the coal fed in the process and mainly contains CO, $CO_2$, $H_2$, $CH_4$, $N_2$, and $H_2S$. Hydrogen sulfide represents a significant problem both environmentally and industrially. In fact, $H_2S$ is a potent poison affecting multiple systems in the majority of the living organisms and also contributes to the phenomenon of acid rains. For this reason, strict environmental policies have been implemented to minimize its obnoxious effects. Interestingly enough, the industry is alike concerned as $H_2S$ corrosive properties may pose a risk for the structural integrity of industrial plants themselves. Usually, gasifier exhaust may contain $H_2S$ up to 15000 ppmv that should be reduced to 150 ppmv as a precondition to attain the best conditions whereby carry out the IGCC process. Therefore, processes capable of removing $H_2S$ from syngas are needed.

### 4.2.2 $H_2S$ Removal and Mid-Temperature Conditions

In order to tackle the problem with $H_2S$, acid gas removal systems (*sweetening processes*) have been designed and set up. These include adsorption by condensation, chemical oxidation, and dry/wet absorption.[4,6] The main drawback of these strategies is the necessity to cool down the syngas to less than 150 °C, or directly at room temperature, and then heat it again before being conveyed to the gas turbine. This results in a decrease in the process thermal efficiency. As a result, it is easy to figure out that processes not involving any

cooling and reheating steps should be preferred in terms of both thermal and $H_2S$ removal efficiency.[4,7] To remove acid gas in IGCC systems, two processes may be currently carried out. The first involves the use of aqueous solutions of methyldiethanolamine or MDEA (chemical route) whereas the other is a physical solvent-based method (Selexol®) which consists in using mixtures of polyethylene glycol and dimethyl ether.[8] Solvent-based physical methods are usually equally effective when compared with its chemical counterparts, but they are more expensive.

In this context, mid-temperature desulfidation is one of the most promising for this purpose. It consists in using regenearable metal oxides as $H_2S$ sorbents either individually or in mixtures at temperatures about 350 °C. Some adsorbents such, the ZnO-based Katalco 32-5, are unsupported whereas others may be supported on an inert carrier which enhances mechanical stability and provides a surface on which the active phase can be dispersed. Among them, mesostructured materials stand out for their unique properties such as high surface area, pore volume, providing with the opportunity to disperse an active phase even inside the pores (refer to Section 4.3.3). Several other metal oxides (transition, earth-alkaline, and lanthanides) have been reported to be efficient and numerous tests have been performed at different development scales to assess their suitability for the process and their performances.[4,9,10]

### 4.2.3 Sulfidation and Regeneration in $H_2S$ Removal: Reactions and Mechanism

Equations 18, 19, and 20 exemplify the reaction involved in a cycle of a generic sulfidation and regeneration cycle:

$$MO_x \longrightarrow MO_y\,(\text{with y} \leq \text{x})\,\text{in}\,H_2, CO \quad \textbf{Reduction} \quad (\textbf{Eq. } 18)$$

$$MO_y + y\,H_2S \longrightarrow MS_y + y\,H_2O \quad \textbf{Sulfidation} \quad (\textbf{Eq. } 19)$$

$$MS_y + O_2 \longrightarrow MO_y + y\,SO_2 \quad \textbf{Regeneration} \quad (\textbf{Eq. } 20)$$

Reactions between $H_2S$ and the metal oxide are affected by pore and/or lattice diffusion. Hydrogen sulfide molecules usually interact with the metal adsorption sites (Figure4.2) whereas interactions with the oxygen sites are deemed unimportant.

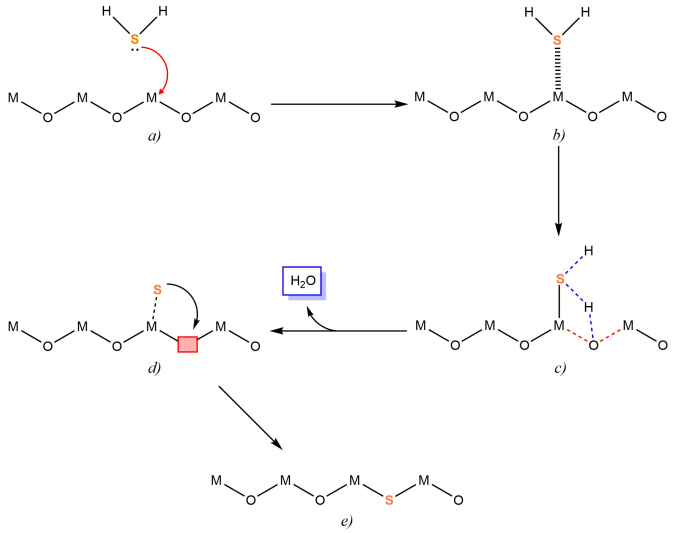


***Figure 4.2*** *Mechanism of Sulfurization by $H_2S$ of a generic metal (M) oxide.*

Currently, sulfidation is thought to begin when a $H_2S$ molecule approaches the adsorption site of the metal oxide surface ($a$). Then, $H_2S$ is chemisorbed implying the formation of a chemical bond ($b$). One of the hydrogen atom belonging to $H_2S$ interacts with an oxygen atom located on the metal oxide surface ($c$). Eventually, a molecule of $H_2O$ is generated leaving a vacant site ($d$) which is promptly occupied by the sulfur atom, with the formation of the metal sulfide ($e$).

## 4.3 Sorbents: A Concise Overview

### 4.3.1 Generalities

A sorbent is defined as a solid substance that is able to adsorb or absorb another phase. Sorption is an important phenomenon exploited in many industrial separation processes in a variety of fields. Sorption as phenomenon is distinguished in absorption and adsorption. Absorption is a purely physical phenomenon whereby the fluid phase is adsorbed into the bulk of the absorbant: no chemical reactions occur and Van Der Waals interactions are the solely to be established between the phases. On the other hand, adsorption involves the formation of chemical bonds between adsorbent and adsorptive and, thus, is a localized phenomenon coming about solely at the interface of the two phases. These reactions that take place upon adsorption are examples of gas-solid reactions. Adorbents ought to feature specific characteristics in order to be aptly used in industrial settings. Among them:[4]

- suitable selectivity derivable from equilibrium, kinetic, or steric effect;
- good mechanical strength;
- fast adsorption kinetics;
- apt adsorption capacity;
- inexpensiveness;
- regenerable with ease.

Concerning the morphological properties of the adsorbent itself, it should feature large internal specific surface area, large internal pore volume, controlled pore size distribution, controlled surface properties, and suitable interactions between adsorbant and adsorbate.[4]

In recent years, a new generations of materials has been developed, including MOFs[11], carbon nanotubes and fibres,[12] metal oxide xerogels and aerogels,[13], mesoporous molecular sieves, and nanocomposite. Their discovery may paved the way to improve existing adsorption processes or lay the foundations for new ones in the forthcoming future.

### 4.3.2 Mechanisms Involved in the Adsorptive Separation

The mechanisms whereby a given adsorbent is able to perform its function are ascribable to three different effects:[14]

- adsorption kinetics effect, which stems from the rate differences at which adsorbate molecules diffuse into the internal structure of the adsorbent;
- adsorption equilibrium effect, associated with the different values of $K_{eq}$ of the thermodynamic equilibria for the adsorbent/adsorbant interactions;
- molecular sieving effect, brought about by the particular morphology that some adsorbents feature enabling them to behave exactly as a sieve would do: adsorbent pores of a given width allow the diffusion of small molecules at the expense of the larger ones. An example may be provided by zeolites, which are exploited by in petroleum industry for a variety of processes.[15–17]

### 4.3.3 Mesostructures, Metal Oxides, and Nanocomposites

Materials such as MCM-41, as described in Chapter 3, feature interesting properties: high specific surface area, high pore volume, suitable particle dimension for this type of applications, apt pore width in the mesoporous range, and good hydrothermal stability. These characteristics render them suitable candidates as support also in the case of $H_2S$ removal from syngas, since they are able to efficiently disperse an active phase all over their exposed surface.[18–22] This is particular relevant to facilitate reactant diffusivity into the sorbent, allowing the full involvement of the active phase in the catalytic process. Moreover, nanoparticles composing the active phase are so well dispersed that sintering phenomena are unlikely to occur. The final product obtained by combining a mesostructure with a well-dispersed nanomaterial is known by the name of nanocomposite.

Several synthetic procedures have been reported in the literature to obtain $SiO_2$-based nanocomposites. These approaches may be broadly classified as either "*direct*" or "*post-synthesis*". The former approach consists in adding the metal oxide precursor in the early stages of the reaction, before the formation of the mesostructure occurs while the latter in first synthesizing the mesostructure and then adding the metal oxide precursor. The aforementioned post-synthesis approach is actually the preferred in virtue of its versatility and reproducibility.[4] Impregnation is one of the most widely used post-synthesis techniques and is especially popular for its easiness of execution. During impregnation, the contact of a solid mesostructured material with a liquid containing the metal oxide precursor is realized. The resulting mixture is then dried so that the active phase may adhere all over the accessible surface of the solid.

Three variants of impregnation exist known as "*wet impregnation*"and "*incipient wetness impregnation*", respectively. Wet impregnation occurs when a volume of impregnating solution is added in excess the total pore volume of the solid. However, this variant entails the possibility of obtaining an overly loaded material with inhomogeneous distribution of the active phase. On the other hand incipient wetness impregnation, sometimes referred as "dry impregnation" consists in adding a precise amount of impregnating solution that equals the pore volume of the solid. In doing so, the impregnated solid appears dry at the

end of the procedure, hence the given adjective. Among the "*incipient wetness impregnation*" techniques, two-solvent impregnation is based on first dispersing a mesostructured material in an apolar solvent and then adding dropwise a volume of aqueous solution containing the metal oxide precursor that, again, is equal to the total pore volume of the solid. When adding the aqueous solution dropwise, the drops containing the precursor will instantly head towards the solvent-prewetted hydrophilic surface of $SiO_2$, given the much greater affinity of water for silanols than for any apolar solvent. It is thought that this mechanism leads to a more effective wettability of the siliceous support and, therefore, impregnation especially inside the pores. This latter technique was singled out for the manufacture of active phase-bearing MCM-41 nanocomposites synthesized from FSA, suitable to be used as sorbents for $H_2S$ removal from syngas[23,24] (see Chapter 7).

# References

[1] U.S. Energy Information Administration Office of Energy Analysis Annual Energy Outlook 2019 with Projections to 2050. https://www.eia.gov/outlooks/aeo/pdf/aeo2019.pdf.

[2] Wheatley, S.; Sovacool, B. K.; Sornette, D. Reassessing the Safety of Nuclear Power. *Energy Research & Social Science* **2016**, *15*, 96–100, ISSN: 2214-6296, DOI: https://doi.org/10.1016/j.erss.2015.12.026.

[3] Pettinau, A.; Frau, C.; Ferrara, F. Performance Assessment of a Fixed-Bed Gasification Pilot Plant for Combined Power Generation and Hydrogen Production. *Fuel Processing Technology* **2011**, *92*, 1946–1953, ISSN: 0378-3820, DOI: https://doi.org/10.1016/j.fuproc.2011.05.014.

[4] Mureddu, M. Mesostructured Metal Oxide-Based Nanocomposites as Sorbents for $H_2S$ Removal from Syngas Coal Gasification., PhD Thesis, University of Cagliari, 2014.

[5] https://i0.wp.com/thefraserdomain.typepad.com/energy/images/igcc_flow_diagram.gif.

[6] Sage P. W. and Mills, S. J. In *Desulfurization of Hot Coal Gas*, ed. by Atimtay, A. T.; Harrison, D. P., Springer Berlin Heidelberg: Berlin, Heidelberg, 1998, pp 21–39, ISBN: 978-3-642-58977-5.

[7] Ko, T.-H.; Chu, H.; Chaung, L.-K. The Sorption of Hydrogen Sulfide from Hot Syngas by Metal Oxides over Supports. *Chemosphere* **2005**, *58*, 467–474, ISSN: 0045-6535, DOI: https://doi.org/10.1016/j.chemosphere.2004.09.029.

[8] Ben-Slimane, R.; Hepworth, M. T. Desulfurization of Hot Coal-Derived Fuel Gases with Manganese-Based Regenerable Sorbents. 3. Fixed-Bed Testing. *Energy & Fuels* **1995**, *9*, 372–378, DOI: https://doi.org/10.1021/ef00050a024.

[9] Deng, S. Sorbent Technology. *Encyclopedia Chem., Process* **2006**, DOI: https://doi.org/10.1081/E-ECHP-120007963,2825-2845.

[10] Mondal, P.; Dang, G.; Garg, M. Syngas Production through Gasification and Cleanup for Downstream Applications — Recent Developments. *Fuel Processing Technology* **2011**, *92*, 1395–1410, DOI: https://doi.org/10.1016/j.fuproc.2011.03.021.

[11] Wen, M.; Li, G.; Liu, H.; Chen, J.; An, T.; Yamashita, H. Metal–organic Framework-based Nanomaterials for Adsorption and Photocatalytic Degradation of Gaseous Pollutants: Recent Progress and Challenges. *Environ. Sci.: Nano* **2019**, *6*, 1006–1025, DOI: https://doi.org/10.1039/C8EN01167B.

[12] Zhang, S.; Shao, T.; Kose, H. S.; Karanfil, T. Adsorption of Aromatic Compounds by Carbonaceous Adsorbents: A Comparative Study on Granular Activated Carbon, Activated Carbon Fiber, and Carbon Nanotubes. *Environmental Science & Technology* **2010**, *44*, PMID: 20704238, 6377–6383, DOI: https://doi.org/10.1021/es100874y.

[13] Ahmed, M. S.; Attia, Y. A. Multi-metal oxide aerogel for Capture of Pollution Gases from Air. *International Conference on Aerospace Sciences and Aviation Technology* **1997**, *7*, 1–13, ISSN: 2090-0678, DOI: https://doi.org/10.21608/asat.1997.25455.

[14] Yang, R. T., *Adsorbents: Fundamentals and Applications*; John Wiley & Sons: 2003, ISBN: 9780471444091.

[15] Halgeri, A. B.; Das, J. Recent Advances in Selectivation of Zeolites for para-disubstituted Aromatics. *Catalysis Today* **2002**, *73*, 65–73, ISSN: 0920-5861, DOI: https://doi.org/10.1016/S0920-5861(01)00519-3.

[16] Ruthven, D. M.; Reyes, S. C. Adsorptive Separation of Light Olefins from Paraffins. *Microporous and Mesoporous Materials* **2007**, *104*, Special Issue: Dedicated to the Late Lovat Rees in Appreciation of His Outstanding Contribution to Zeolite Science, 59–66, ISSN: 1387-1811, DOI: https://doi.org/10.1016/j.micromeso.2007.01.005.

[17] Kulprathipanja, S., *Zeolites in Industrial Separation and Catalysis*; Wiley: 2010, ISBN: 9783527629572, DOI: https://doi.org/10.1002/9783527629565.

[18] Dhage, P.; Samokhvalov, A.; Repala, D.; Duin, E. C.; Bowman, M.; Tatarchuk, B. J. Copper-Promoted $ZnO/SiO_2$ Regenerable Sorbents for the Room Temperature Removal of $H_2S$ from Reformate Gas Streams. *Industrial & Engineering Chemistry Research* **2010**, *49*, 8388–8396, DOI: 10.1021/ie100209a.

[19] Wu, M.; Shi, L.; Lim, T.; Veksha, A.; Yu, F.; Fan, H.; Mi, J. Ordered Mesoporous Zn-Based Supported Sorbent Synthesized by a new Method for High-Efficiency Desulfurization of Hot Coal Gas. *Chemical Engineering Journal* **2018**, *353*, 273–287, ISSN: 1385-8947, DOI: https://doi.org/10.1016/j.cej.2018.07.134.

[20] Mureddu, M.; Ferino, I.; Rombi, E.; Cutrufello, M.; Deiana, P.; Ardu, A.; Musinu, A.; Piccaluga, G.; Cannas, C. ZnO/SBA-15 Composites for Mid-Temperature Removal of $H_2S$: Synthesis, Performance and Regeneration Studies. *Fuel* **2012**, *102*, Special Section: ACS Clean Coal, 691–700, ISSN: 0016-2361, DOI: https://doi.org/10.1016/j.fuel.2012.05.013.

[21] Liu, T.; Jin, F.; Wang, X.; Fan, Y.; Yuan, M. Synthesis of Titanium Containing MCM-41 from Industrial Hexafluorosilicic Acid as Epoxidation Catalyst. *Catalysis Today* **2017**, *297*, Catalytic science and technology in Sustainable Environment II (EECAT 2016), 316–323, ISSN: 0920-5861, DOI: https://doi.org/10.1016/j.cattod.2017.03.011.

[22] Wang, X.; Jia, J.; Zhao, L.; Sun, T. Mesoporous SBA-15 Supported Iron Oxide: a Potent Catalyst for Hydrogen Sulfide Removal. *Water Air Soil Pollut.* **2008**, *193*, 247–257.

[23] Cara, C.; Rombi, E.; Musinu, A.; Mameli, V.; Ardu, A.; Sanna Angotzi, M.; Atzori, L.; Nižňanský, D.; Xin, H. L.; Cannas, C. MCM-41 Support for Ultrasmall $\gamma$-$Fe_2O_3$ Nanoparticles for $H_2S$ Removal. *J. Mater. Chem. A* **2017**, *5*, 21688–21698, DOI: http://dx.doi.org/10.1039/C7TA03652C.

[24] Cara, C.; Rombi, E.; Ardu, A.; Vacca, M. A.; Cannas, C. Sub-Micrometric MCM-41 Particles as Support to Design Efficient and Regenerable Maghemite-Based Sorbent for $H_2S$ Removal. *Journal of Nanoscience and Nanotechnology* **2019**, *19*, 5035–5042, ISSN: 1533-4880, DOI: https://doi.org/10.1166/jnn.2019.16800.

# 5

# Precipitated Silica from FSA for Tyre Reinforcement

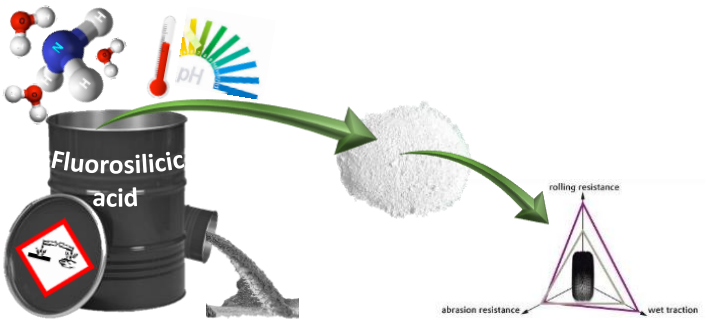


*The synthesis of precipitated silica (PS) from FSA for possible application in tyre reinforcement is reported hereinafter in this chapter. With the aim of obtaining suitable surface area values for the desired application, the effects of pH, temperature, flow rate, and concentration of the reactants were investigating. Attempts to utilizing the supernatant from previous reactions were also carried out. The samples deemed to be the most promising were used to prepare tread compounds and their performances were tested.*

## 5.1 Introduction and Description of Syntheses and Analyses

This chapter is devoted to describing a series of experiments aimed at obtaining precipitated silica suitable for being used as a tyre reinforcing agent by

reacting $H_2SiF_6$ with $NH_3$ (Eq. 21). The choice of $NH_3$ over other bases was made considering its cost, wide availability and, in particular, for the opportunity of its own recovery from $NH_4F$ (Eq. 22).[1,2]

$$6\,NH_3 + H_2SiF_6 + 2\,H_2O \longrightarrow SiO_2 + 6\,NH_4F \qquad \textbf{(Eq. 21)}$$

$$NH_4F \longrightarrow NH_3 + HF \qquad \textbf{(Eq. 22)}$$

The syntheses were performed in a jacketed glass vessel where FSA was added into the $NH_3$ solution by means of a peristaltic pump. The only exceptions were the experiments where the supernatant derived from previous syntheses was utilized as the reaction *medium* (section 5.5). A simplified diagram of the reactor is depicted in Figure 5.1. In all the experiments, stirring was set at 200 rpm, both during the addition of FSA and the post-synthesis stirring. pH was carefully monitored by regular measurements with a fluoride-resistant electrode, with more frequent controls when the desired pH value was about to be approached. Once reached the desired pH, FSA addition was stopped and the so-formed slurry was then left under continuous stirring for 90 minutes. Temperature was monitored as well. The obtained silica was recovered by vacuum filtration and washed (see paragraph 5.2). Finally, the sample was in part dried in a oven at 105 °C overnight and the rest kept wet as obtained. A diagram of the synthetic process is shown in Figure 5.2.

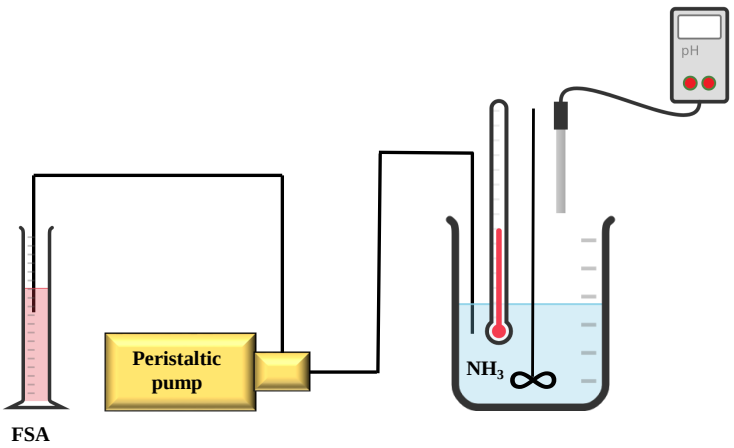


***Figure 5.1*** *Simplified diagram of the equipment used for the synthesis of precipitated silica.*

On the dried fraction, **$N_2$-physisorption** measurements, loss on ignition, and wavelength dispersive x-ray fluorescence (**WD-XRF**) were systematically

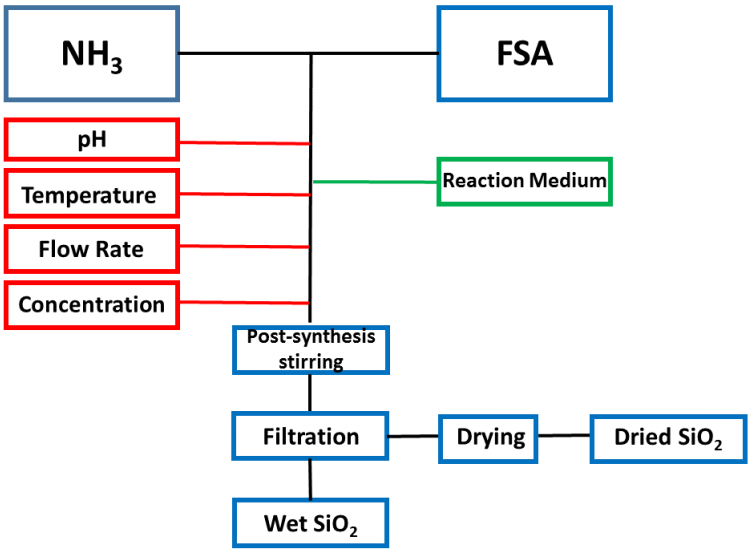


***Figure 5.2*** *Diagram of the synthetic procedure for obtaining precipitated silica from $H_2SiF_6$. The investigated parameters are highlighted in red. Change of reaction medium, a peculiar synthesis performed, is boxed in green.*

performed on all the samples while the most promising samples underwent further characterization by means of thermogravimetry (**TGA**) and transmission electronic microscopy (**TEM**) on the wet fraction.Throughout this work, several experimental conditions such as final pH, temperature, reactant concentration, rate of addition, and reaction *medium* with the simultaneous addition of the reactants were varied to assess their effect on the final product. If not stated otherwise, both FSA and $NH_3$ concentrations are intended to be between 23 and 24 % w/w.

### 5.1.1 Sample Labelling

Given the number of parameters changed, the samples were labelled according to the following layout:

PS-T**X**_pH**Y**_R**Z**_**LABEL**

where **X** indicates the temperature reached inside the reactor jacket by flowing either:

- hot silicone oil (100 °C), indicated as T**100**;
- mains water (20 °C), T**20**;

- a chilled 1:1 solution of $H_2O$ and ethylene glycol (0 °C), T**0**;

**Y** stands for the final pH reached at the end of the reaction;

and **Z** is the addition rate of the reactants expressed in mL $min^{-1}$. Occasionally, g $min^{-1}$ will be used and a conversion in mL $min^{-1}$ will be given.

A **LABEL** may be added for better identification.

## 5.2 Assessing the Washing Process

When considering the use of FSA-derived $SiO_2$ in tyres, it is necessary that fluorine content in the final product should be as low as possible. Therefore, the first step before setting up the actual experimental work was to assess the best conditions for an effective washing procedure. To do this, a few syntheses were specially performed at room temperature to simply obtain apt amounts of silica to be washed. Addition of FSA into $NH_3$ (approximately 200 mL) was allowed for one hour, fluxing rate was set at 4 mL $min^{-1}$, and stirring rate was set at 200 rpm. Once the addition of FSA was over, the slurry was stirred for 90 minutes and $SiO_2$ was then recovered by vacuum filtration. The so-obtained silica underwent different washing regimes in terms of quantity of water, number of washing rounds, and water temperature. To reduce the number of parameters involved, stirring rate (200 rpm), quantity of wet silica (100 g), and washing time (1 h) were kept constant. Before analysis, samples were dried in an oven at 105 °C overnight. The content of $F^-$ in $SiO_2$ was determined by **WD-XRF**, which allows rapid and cost-effective measurements. Throughout the following experiments, only the samples whose $F^-$ content was below the limit of detection (BLD) of the instrument were considered suitable for the intended application. Table 5.2 reports the results of these washing tests. For the sake of conciseness, only a partial summary of the tests actually performed is given.

As a result of these attempts, **5** and **6** yielded silica with a content of fluorine inferior to the instrumental detection limit but **5** was preferred over **6**, despite being more time consuming, to ensure the purity of the final product in particular for those samples featuring higher surface areas.
In the next page, the precipitated silica samples synthesized in this chapter are

***Table 5.1*** *Washing tests performed by varying different parameters. BLD stands for below the limit of detection.*

| Test | Quantity of $H_2O$ (L) | Temperature (°C) | Washing Rounds (number) | $F^-$ Content % |
|---|---|---|---|---|
| **1** | 0.5 | 25 | 1 | 0.60 |
| **2** | 0.5 | 25 | 3 | 0.39 |
| **3** | 0.5 | 50 | 1 | 0.24 |
| **4** | 1.0 | 25 | 1 | 0.19 |
| **5** | 1.0 | 50 | 3 | BLD |
| **6** | 1.0 | 50 | 2 | BLD |

reported in table 5.2

***Table 5.2*** *Precipitated $SiO_2$ samples synthesized in this chapter and the synthesis condition under which they were obtained.*

| Sample Name | T (°C) | pH | Flow Rate (mL $min^{-1}$) | Yield (%) | Ratio $NH_3$/FSA (mol/mol) |
|---|---|---|---|---|---|
| **PS-T20_pH9.2_R4** | 20 | 9.2 | 4 | 80.3 | 6.6 |
| **PS-T20_pH8.7_R4** | 20 | 8.7 | 4 | 79.2 | 6.4 |
| **PS-T20_pH8.4_R4** | 20 | 8.4 | 4 | 82.8 | 6.2 |
| **PS-T20_pH8.1_R4** | 20 | 8.1 | 4 | 80.7 | 5.7 |
| **PS-T20_pH7.8_R4** | 20 | 7.8 | 4 | 79.6 | 5.5 |
| **PS-T100_pH8.4_R4** | 100 | 8.4 | 4 | 67.8 | 6.3 |
| **PS-T100_pH8.1_R4** | 100 | 8.1 | 4 | 70.2 | 5.8 |
| **PS-T100_pH7.8_R4** | 100 | 7.8 | 4 | 69.7 | 5.5 |
| **PS-T0_pH8.4_R4** | 0 | 8.4 | 4 | 66.8 | 5 |
| **PS-T0_pH8.1_R4** | 0 | 8.1 | 4 | 65.2 | 4.3 |
| **PS-T0_pH7.8_R4** | 0 | 7.8 | 4 | 64.7 | 3.5 |
| **PS-T0_pH8.1_R2** | 0 | 8.1 | 2 | 77.3 | 6.0 |
| **PS-T0_pH8.1_R0.5** | 0 | 8.1 | 0.5 | 76.2 | 5.5 |
| **PS-T20_pH8.4_R4_HC** | 20 | 8.4 | 4 | 79.7 | 8.9 |
| **PS-T20_pH8.1_R4_HC** | 20 | 8.1 | 4 | 77.2 | 9.6 |
| **PS-T20_pH8.4_SN** | 8.4 | 73.2 | 4.8 | * | * |
| **PS-T20_pH8.1_SN** | 8.1 | 70.7 | 5.5 | * | * |

** See section 5.5 for values in g $min^{-1}$ of flow rate and molar ratios. $F^-$ content assessed in these samples are always below the limit of detection of the WA-XRF instrument in use.*

## 5.3 Effect of Temperature

### 5.3.1 Effect of pH at room temperature

As stated in section 1.2.4, there is a paucity of reports about systematic comparisons of the properties of precipitated silica obtained in one-step synthesis by reacting FSA and $NH_3$. In this context, the seminal work of Yu and colleagues addressed the effect of final reaction pH on surface area when FSA is reacted with $NH_3$ *via* a two-step ammoniation reaction.[3] By analogy, a similar study is herein reported with the relationship between pH and surface area by reacting FSA and ammonia in a one-step reaction. This was carried out over the range of pH values whereby Yu and colleagues had obtained $SiO_2$, featuring surface area values close to those of interest for tyre reinforcement. Therefore, a batch of five experiments was set up; water was fluxed into the reactor jacket while a solution of FSA was added into 200 mL of a solution of $NH_3$ through a peristaltic pump at a rate fixed at 4 mL $min^{-1}$. The addition of FSA was then stopped when the desired pH values of 9.2, 8.7, 8.4, 8.1, and 7.8 were obtained after the ninety minute post-synthesis stirring step. To achieve this, a trial-and-error approach was adopted. During the experiments, temperatures about 20 °C were reached. The products obtained were recovered by vacuum filtration, washed as described in section 5.2 and analysed. The data collected are reported in Table 5.3 and 5.4. Yields were calculated by considering FSA as the limiting reactant.

***Table 5.3*** *Study of the pH effect on precipitated silica in the pH range 7.8-9.2 by flowing mains water (4 mL $min^{-1}$) at room temperature into the reactor jacket.*

| Sample | Yield (%) | Ratio $NH_3$/FSA (mol/mol) | LoI (%) | Surface Area ($m^2$ $g^{-1}$) | Mean Pore Size (nm) |
|---|---|---|---|---|---|
| **PS-T20_pH9.2_R4** | 80.3 | 6.6 | 6.29 | 20 | - |
| **PS-T20_pH8.7_R4** | 79.2 | 6.4 | 7.2 | 91 | - |
| **PS-T20_pH8.4_R4** | 82.8 | 6.2 | 10.7 | 259 | 3.5 |
| **PS-T20_pH8.1_R4** | 80.7 | 5.7 | 9.8 | 201 | 3.4 |
| **PS-T20_pH7.8_R4** | 79.6 | 5.5 | 8.1 | 193 | 3.1 |

*Relative standard deviation: %RSD($S_{BET}$)=2.1%; ; %RSD (Mean Pore Size)=1.8%*

***Table 5.4*** *Relative volume per pore size class.*

| Sample | Micropores (%) | Mesopores (%) | Macropores (%) |
|---|---|---|---|
| **PS-T20_pH9.2_R4** | 1.81 | 82.62 | 15.54 |
| **PS-T20_pH8.7_R4** | 3.89 | 76.84 | 19.27 |
| **PS-T20_pH8.4_R4** | 10.47 | 87.37 | 2.17 |
| **PS-T20_pH8.1_R4** | 6.59 | 88.91 | 4.50 |
| **PS-T20_pH7.8_R4** | 5.85 | 88.97 | 5.18 |

All the samples were free from fluorine impurities, confirming the adequacy of the washing step. Figure 5.3 reports the **FT-IR** characterization of these samples and confirm the nature of the product as silica, with the typical bands related to the symmetric stretching modes of the siloxanes at 1240 $cm^{-1}$, 1060 $cm^{-1}$, and 800 $cm^{-1}$. A band located at 460 $cm^{-1}$ is ascribable to the bending mode of the same group while the stretching mode of silanols is located at 960 $cm^{-1}$. The spectra confirm the absence of vibrational modes related to $NH_4^+$ at 1400 and 3140 $cm^{-1}$, possibly ascribable to $NH_4F$.

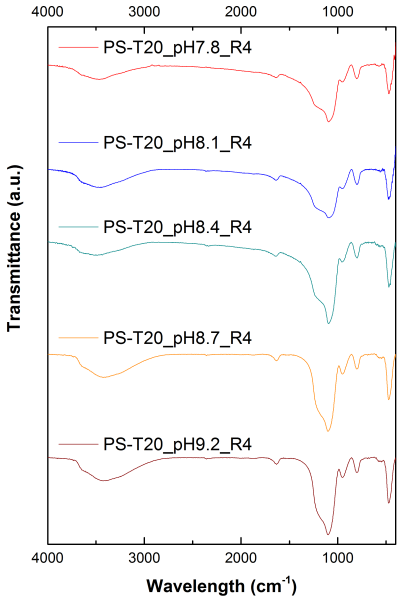


***Figure 5.3*** *FT-IR spectra of the samples synthesized to assess the effect of pH on the properties of precipitated silica from FSA.*

Excluding PS-T20_pH9.2_R4 (figures 5.4a-b) and PS-T20_pH8.7_R4 (figures 5.4c-d), the **$N_2$-physisorption** isotherms obtained from the other samples (figure 5.5a-f) can all be either classified as IIb (figure 5.5c-f), with the hysteresis indicating mesoporosity of such materials ascribable to interparticle interstices.[4]

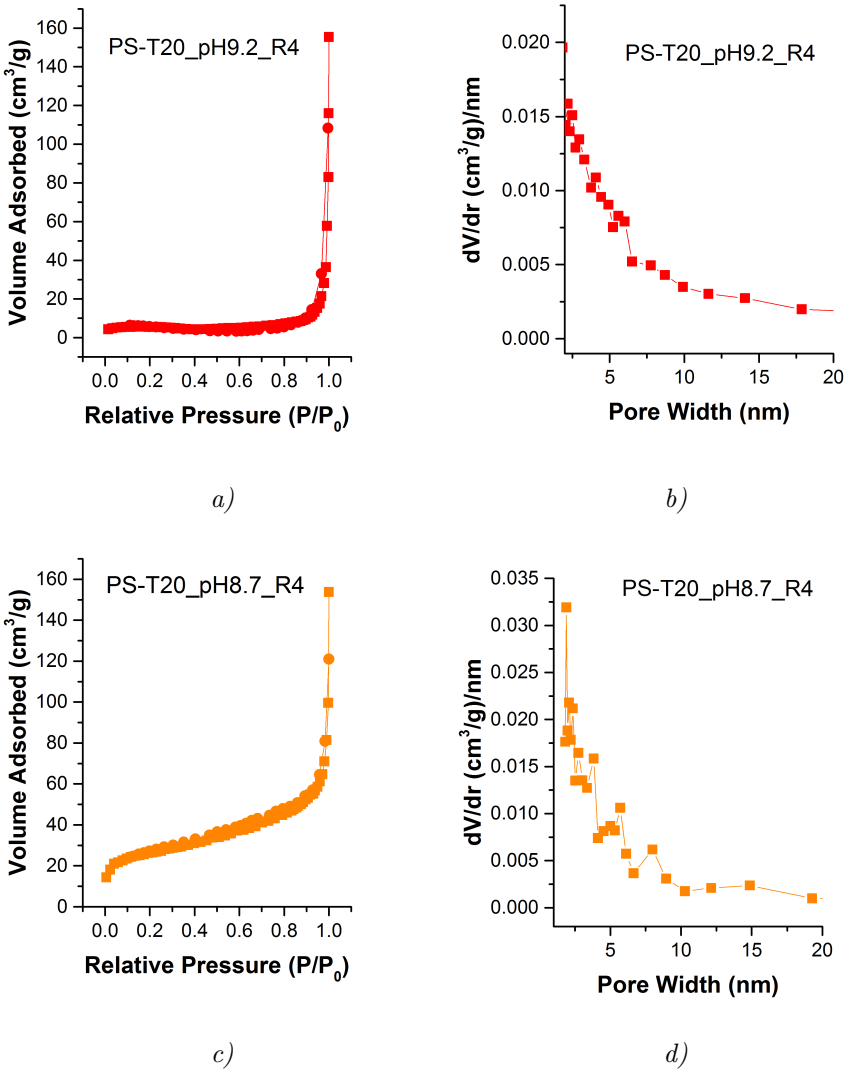


***Figure 5.4*** *Isotherms and pore size distributions for the samples PS-T20_pH9.2_R4 (a-b) and PS-T20_pH8.7_R4 (c-d).*

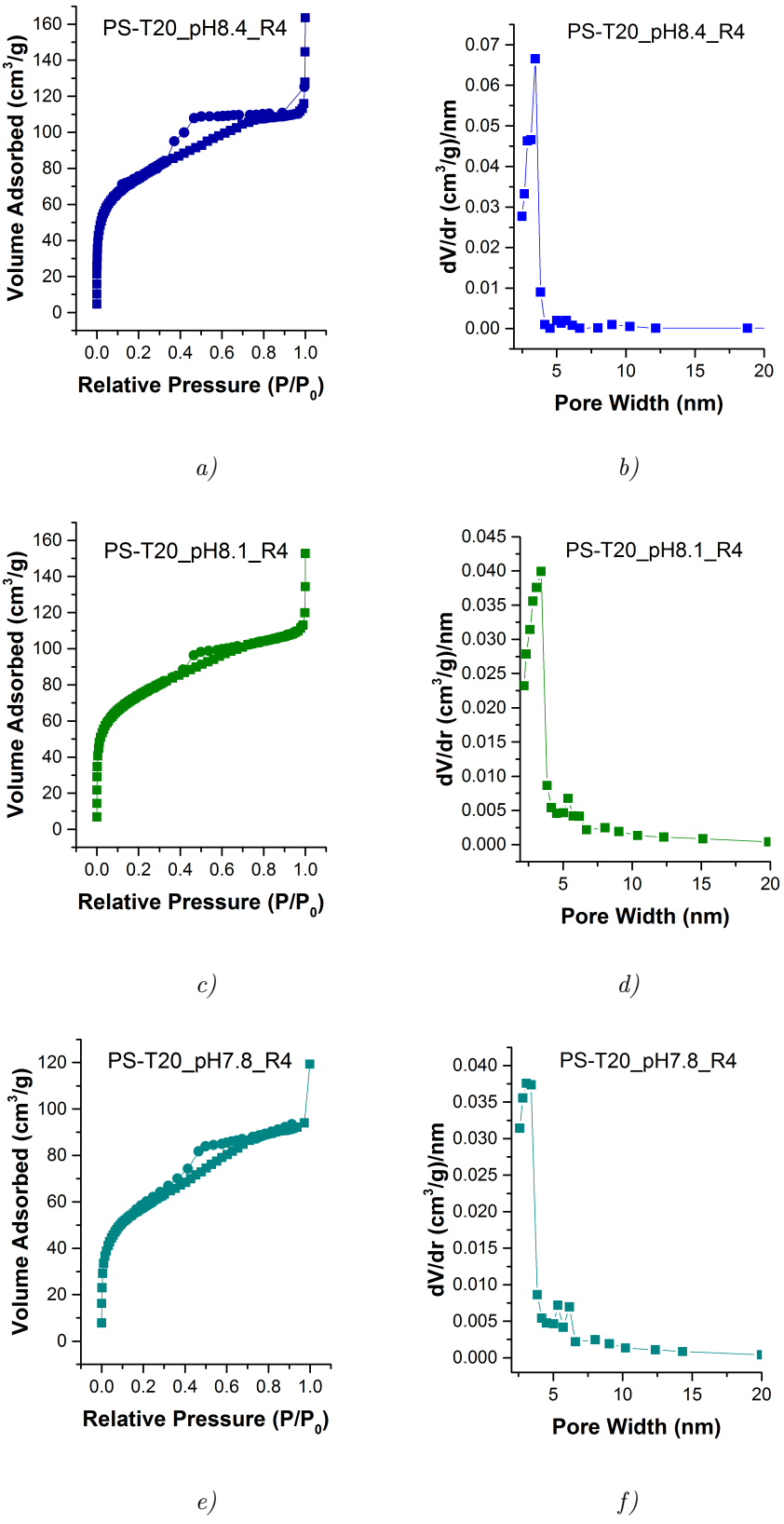


***Figure 5.5*** *Isotherms and pore size distributions for the samples PS-T20_pH8.4_R4 (a-b), PS-T20_pH8.1_R4 (c-d), and PS-T20_pH7.8_R4 (e-f).*

Mean pore sizes confirm the mesoporosity of the three samples, ranging from 3.1 to 3.5 nm, with the negligible contributions of wider mesopores. As for the sample synthesized at pH=9.2, its isotherm can be classified as type III, typical for non-porous or macroporous materials. The low surface area (just 20 $m^2$ $g^{-1}$) and pore size of the sample distribution (5.4b) may back up this finding. Classifying the isotherm of PS-T20_pH8.7_R4 is more problematic. Compared with 5.4c, a *point B* can be spotted[5] just before $P/P_0$=0.1 that might lead to conclude that a type IIa isotherm should be considered. Observations from table 5.4 suggest that low surface area in the samples (pH=9.2 and 8.7) can be mainly associated with the small contribution of micropores, being the amount of mesopores very similar. On the other hand, the content of micropores in the other samples (pH=8.4, 8.1, and 7.8), from 6 to 10 % confirm the higher surface area values. The trend of surface area values (figure 5.6) versus pH highlights a maximum at pH=8.4, however the its own asymmetry points to consider the range of pH between 7.8 and 8.4 as the most suitable for the intended application. Therefore, this pH range will be the only one to be investigated in the following sections.

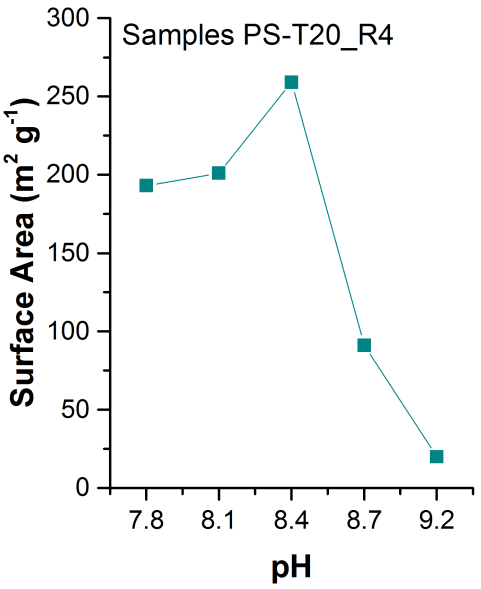


***Figure 5.6*** *Trend of surface area values of the precipitated $SiO_2$ synthesized in the range of pH 7.8-9.2 at room temperature.*

TEM images at high magnifications of the most promising sample, synthesized at pH=8.4 (figure 5.7), highlight the formation aggregates of spheroidal particles, consisting in smaller primary nanoparticles, which aggregates leaving micro- and mesoporous interstices among nanoparticles. These interstices may justify the high surface area obtained and the hysteresis shown in the isotherms.

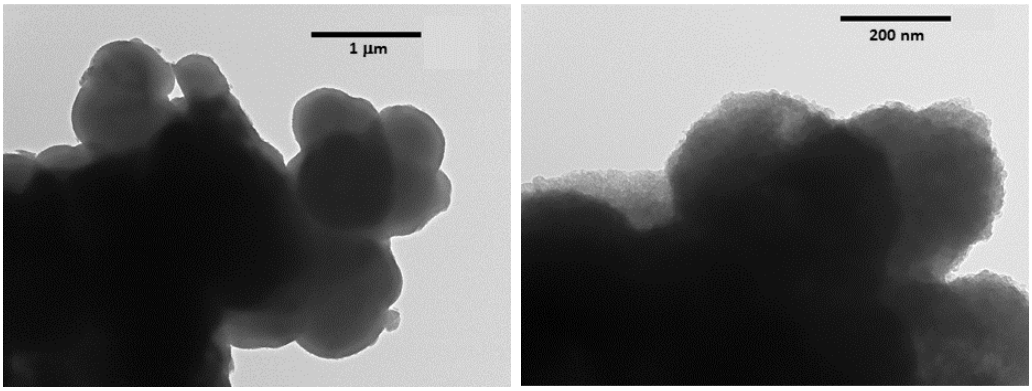


***Figure 5.7*** *TEM micrographs at different magnification of the sample PS-T20_pH8.4_R4.*

### 5.3.2 Effect of High Temperature at different pH Values

Once pinpointed the range of pH from 7.8 to 8.4, a systematic study on the temperature was carried out. In lieu of water, the reactions were performed by fluxing in the reactor jacket silicon oil at 100 °C. The actual temperature reached by the reaction mixture was 65 °C. Apt amounts of FSA (determined again through a trial-and-error process) were added to reach the desired pH values (7.8; 8.1; 8.4) once the post-synthesis stirring was stopped. Usual characterizations were performed and the results are given in Table 5.5. **$N_2$-physisorption** isotherms with pore size distributions are depicted in figure and 5.8, respectively.

In these three samples synthesized at high temperature, surface area values ranges from 23 to 30 $m^2$ $g^{-1}$. When synthesis is performed in an alkali *medium* and above 60 °C, as it is the case, primary particles are usually non-porous, eliciting the formation and the assembly of non-porous primary particles that inevitably leads to obtaining silica with low surface area.[6,7] So low are the values that these samples are unlikely to be suitable candidates for tyre reinforcement when compared with the PS-T20 ones.[8] The three **$N_2$-physisorption** isotherms can be classified as type III, typical for non-porous or macroporous materials.

***Table 5.5*** *Study of the pH effect at 100 °C from FSA.*

| Sample | Yield (%) | Ratio $NH_3$/FSA (mol/mol) | LoI (%) | Surface Area ($m^2$ $g^{-1}$) | Mean Pore Size (nm) |
|---|---|---|---|---|---|
| **PS-T100_pH8.4_R4** | 67.8 | 6.3 | 6.8 | 27 | - |
| **PS-T100_pH8.1_R4** | 70.2 | 5.8 | 10.0 | 23 | - |
| **PS-T100_pH7.8_R4** | 69.7 | 5.5 | 8.2 | 30 | - |

*Relative standard deviation: %RSD($S_{BET}$)=2.1%; %RSD (Mean Pore Size)=1.8%.*

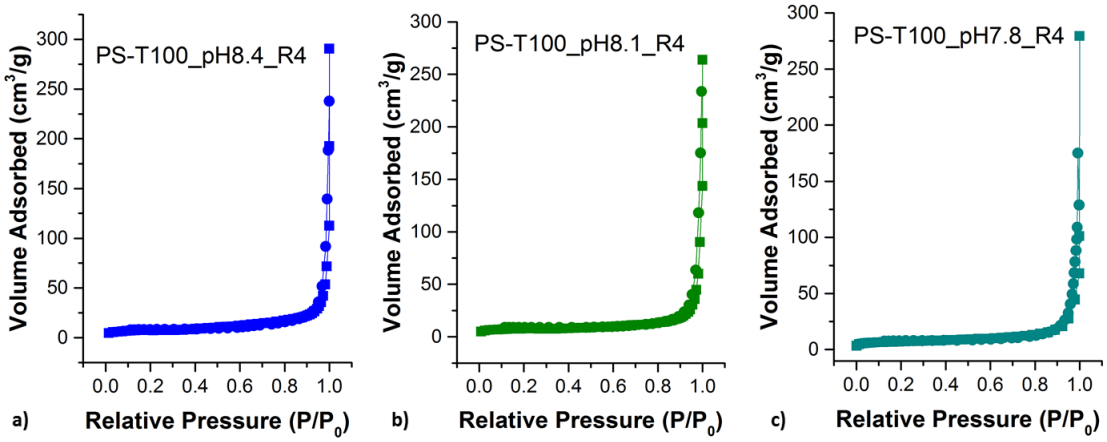


***Figure 5.8*** *Isotherms of the samples a) PS-T100_pH8.4_R4 , b) PS-T100_pH8.1_R4 , and c) and PS-T100_pH7.8_R4.*

### 5.3.3 Effect of Low Temperature at different pH

Experiments at low temperature were carried out by fluxing a mixture 50 % w/w of ethylene glycol in water cooled at 0 °C with the aid of a chiller but the actual reaction temperatures reached during the syntheses were about 3 °C. The usual pH range 7.8 - 8.4 was explored. As usual, **WD-XRF**, and **LoI**, and **$N_2$-physisorption** were performed on the samples. Tables 5.6 and figures 5.9, 5.10 report the results of these analyses. The three $N_2$-physisorption isotherms can be classified as type IIa, with a mesoporous contribution given by particle interstices.

From figure 5.10, it is possible to observe that in selected pH range the most promising samples synthesized at low temperature are those obtained at pH

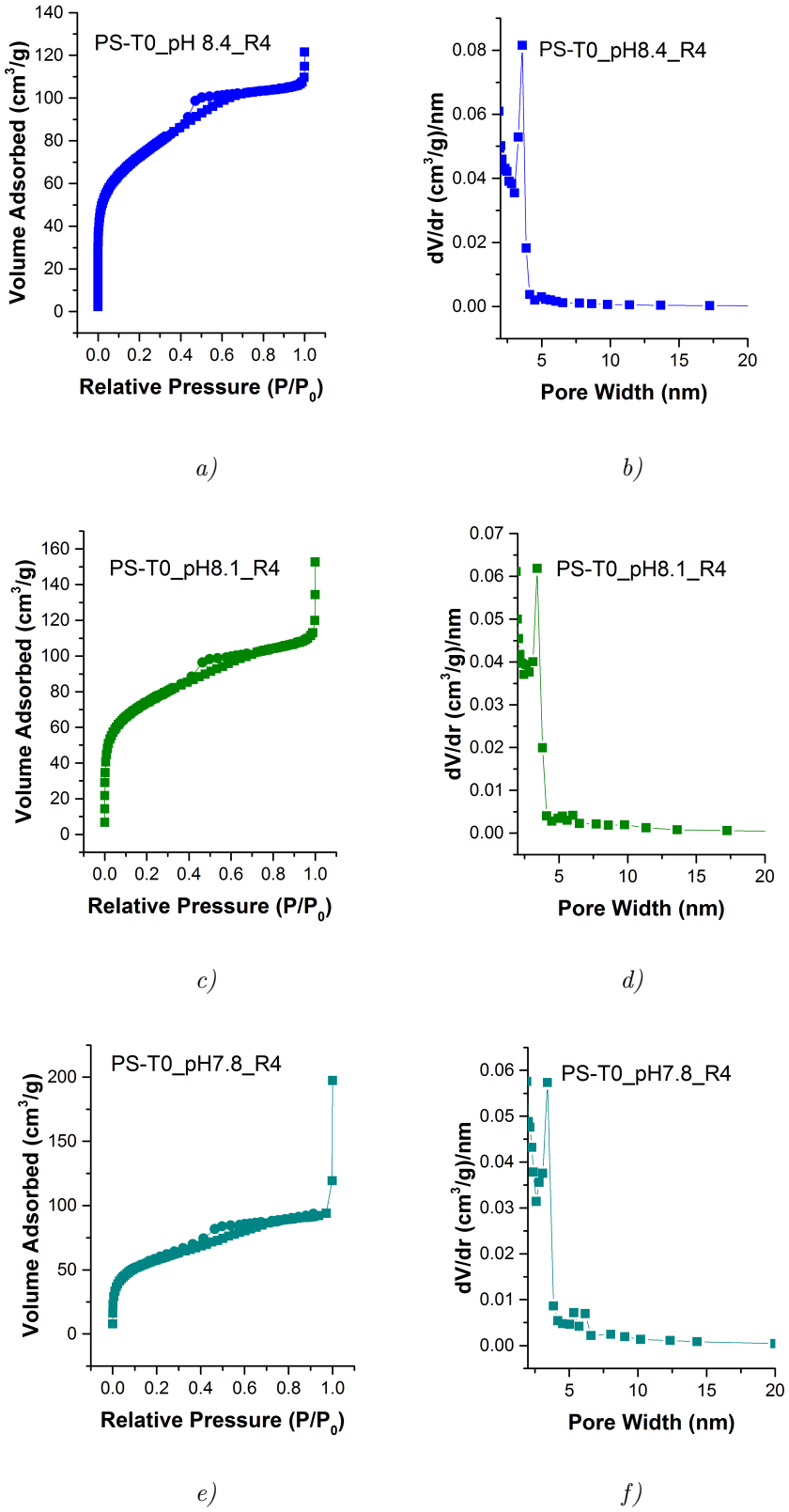


***Figure 5.9*** *Isotherms and pore size distributions for the samples PS-T0_pH8.4_R4 (a-b), PS-T0_pH8.1_R4 (c-d), and PS-T0_pH7.8_R4 (e-f).*

***Table 5.6*** *Study of the pH effect at T=0 °C on precipitated silica from FSA.*

| Sample | Yield (%) | Ratio $NH_3$/FSA (mol/mol) | LoI (%) | Surface Area $m^2\ g^{-1}$ | Mean Pore Size nm |
|---|---|---|---|---|---|
| **PS-T0_pH8.4_R4** | 66.8 | 5 | 6.1 | 253 | 3.5 |
| **PS-T0_pH8.1_R4** | 65.2 | 4.3 | 6.8 | 256 | 3.4 |
| **PS-T0_pH7.8_R4** | 64.7 | 3.5 | 6.1 | 81 | 3.1 |

*Relative standard deviation: %RSD($S_{BET}$)=2.1%; %RSD (Mean Pore Size)=1.8%*

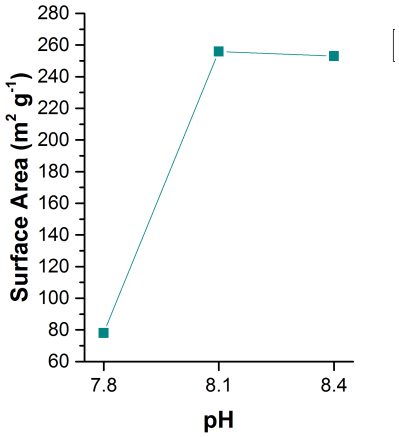


***Figure 5.10*** *Trend of surface area values of the precipitated $SiO_2$ synthesized in the range of pH 7.8-8.4 at low temperature.*

values of 8.1 and 8.4, while, as for the sample at 7.8, a drop in the value of surface area was observed. TEM (figure 5.11 e 5.12) images allow to confirm the similarities between the two samples, with the sample PS_T0_pH8.4_R4 showing of large aggregates of spheroidal particles made up of tiny nanoparticles which in turn form micro- and mesointerstices. No morphological differences can be evidenced concerning surface areas.

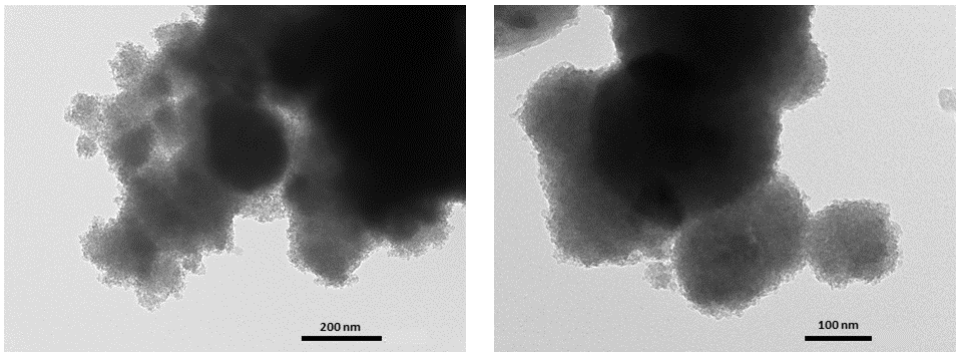


***Figure 5.11*** *TEM micrographs at different magnification of the sample PS-T0_pH8.4_R4.*

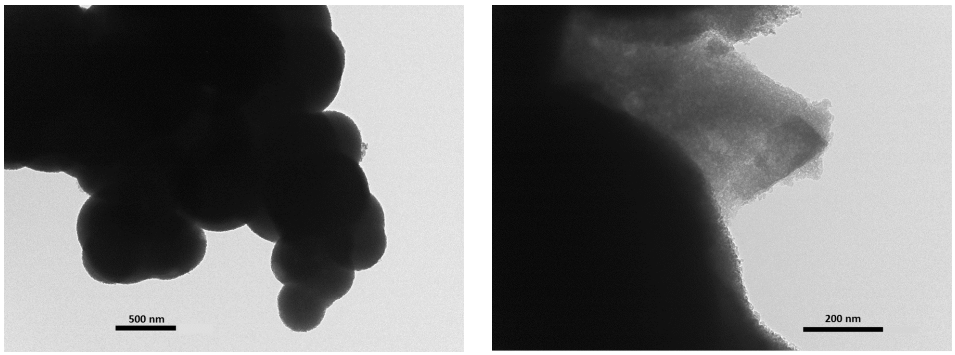


***Figure 5.12*** *TEM micrographs at different magnification of the sample PS-T0_pH8.1_R4.*

In conclusion, temperature effect on precipitated $SiO_2$ affects specific surface area values at different pH but a general trend can not be drawn, especially for samples obtained at pH=7.8. However, at pH=8.4, high surface values was found for both low and room temperature syntheses and similar high value of surface area characterized the sample synthesized at low temperature at pH=8.1. Conversely, syntheses at high temperatures consistently yield precipitated silica with low surface area, as expected by the literature concerning precipitation using sodium silicate and here confirmed when FSA is used. For the envisaged purpose of obtaining precipitated $SiO_2$ for tyre reinforcement, low temperature samples were deem to be the most promising as they show a wide range of relevant surface area values for the intended purpose, by simply changing pH.

## 5.4 Miscellaneous Tests: FSA addition rate and concentration of reactants

This supplementary chapter will be devoted to describing briefly a few exploratory syntheses performed to assess how FSA addition rate and concentration of the reactants affect $SiO_2$ surface area.

### 5.4.1 FSA Addition Rate Effect

In these batch of experiments, FSA addition rate effect was assessed by reducing its flow rate to *2 mL min$^{-1}$* and *0.5 mL min$^{-1}$* at pH value of 8.1. Table 5.7 attests how addition rate influences the textural properties of precipitated $SiO_2$ obtained from FSA at low temperature at pH = 8.1. While **LoI**, relative porosity contributions, and mean pore size distributions are minimally affected by addition rate, surface area values significantly. Although reducing addition rate to 2 mL min$^{-1}$ has no effect on surface area, the sample synthesized by adding FSA at a rate of 0.5 mL min$^{-1}$ reaches a surface area value of 301 m$^2$ g$^{-1}$ (table 5.7). $N_2$-physisorption measurements confirm that these samples show isotherms ascribable to the type IIb.

***Table 5.7*** *Addition rate effect on precipitated $SiO_2$ synthesis from FSA at pH = 8.1 at low temperature.*

| Sample | Yield (%) | Ratio $NH_3$/FSA (mol/mol) | LoI (%) | Surface Area ($m^2$ $g^{-1}$) | Mean Pore Size (nm) |
|---|---|---|---|---|---|
| **PS-T0_pH8.1_R4*** | 65.2 | 4.3 | 6.8 | 256 | 3.4 |
| **PS-T0_pH8.1_R2** | 77.3 | 6.0 | 10.6 | 259 | 3.5 |
| **PS-T0_pH8.1_R0.5** | 76.2 | 5.5 | 11.6 | 301 | 3.4 |

*Relative standard deviation: %RSD($S_{BET}$)=2.1%; %RSD (Mean Pore Size)=1.8%. *Sample's data already presented earlier in this thesis (Table 5.6).*

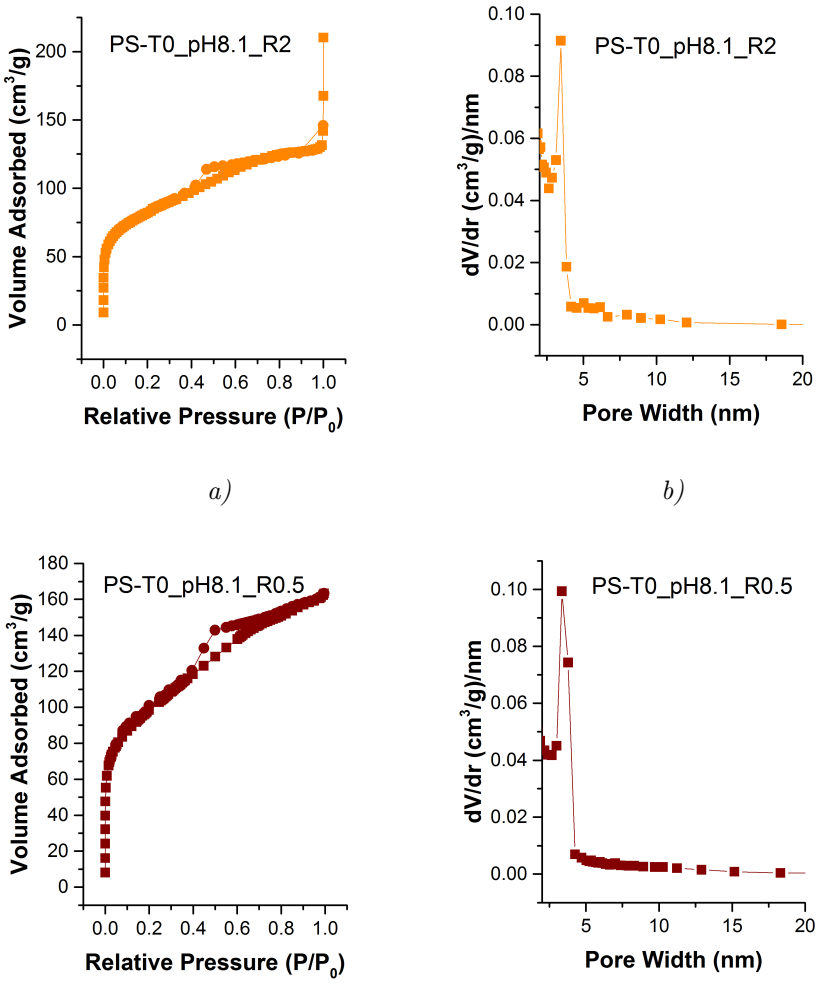


***Figure 5.13*** *Isotherms and pore size distributions for the samples PS-T0_pH8.1_R2 (a-b) and PS-T0_pH8.1_R0.5 (c-d).*

### 5.4.2 Concentration Effect

The effect of reducing the concentrations of the two reactants to 13 % w/w by flowing mains water into the reactor jacket, are reported in table 5.8. The temperature was set at 20 °C in virtue of the similar surface area values obtained at the pH of 8.1 and 8.4. The sample were labelled with the letter HC, which stands for halved concentration of reactants. By comparing these data with those relative to the samples PS-T20_pH8.4_R4 and PS-T20_pH8.1_R4 (Table 5.3 and 5.4), it is possible to evince that surface area values are higher for the HC samples (approximately 25 % more), with comparable values of mean pore size and **LoI**.

***Table 5.8*** *Effect on surface area of $SiO_2$ synthesized at room temperature from 13 % w/w FSA and $NH_3$ solutions for pH values of 8.1 and 8.4.*

| Sample | Conc. $NH_3$ (%) | Conc. FSA (%) | Yield (%) | Ratio $NH_3$/FSA (mol/mol) | LoI (%) | Surface Area ($m^2$ $g^{-1}$) | Mean Pore Size (nm) |
|---|---|---|---|---|---|---|---|
| **PS-T20_pH8.4_R4*** | 82.8 | 22 | 23 | 6.2 | 10.7 | 259 | 3.5 |
| **PS-T20_pH8.4_R4_HC** | 79.7 | 13 | 23 | 6.1 | 8.9 | 289 | 3.3 |
| **PS-T20_pH8.1_R4*** | 80.7 | 22 | 23 | 5.7 | 9.8 | 201 | 3.4 |
| **PS-T20_pH8.1_R4_HC** | 77.2 | 13 | 23 | 5.3 | 9.6 | 286 | 3.5 |

*Relative standard deviation: %RSD($S_{BET}$)=2.1%; %RSD (Mean Pore Size)=1.8%. *Sample's data already presented earlier in this thesis (Table 5.3).*

In light of these preliminary results reported in this paragraph, reducing addition and reactant concentration lead both to increasing surface area while leaving the other parameters unchanged. This may be of particular interest in applications in which higher values of surface are required.

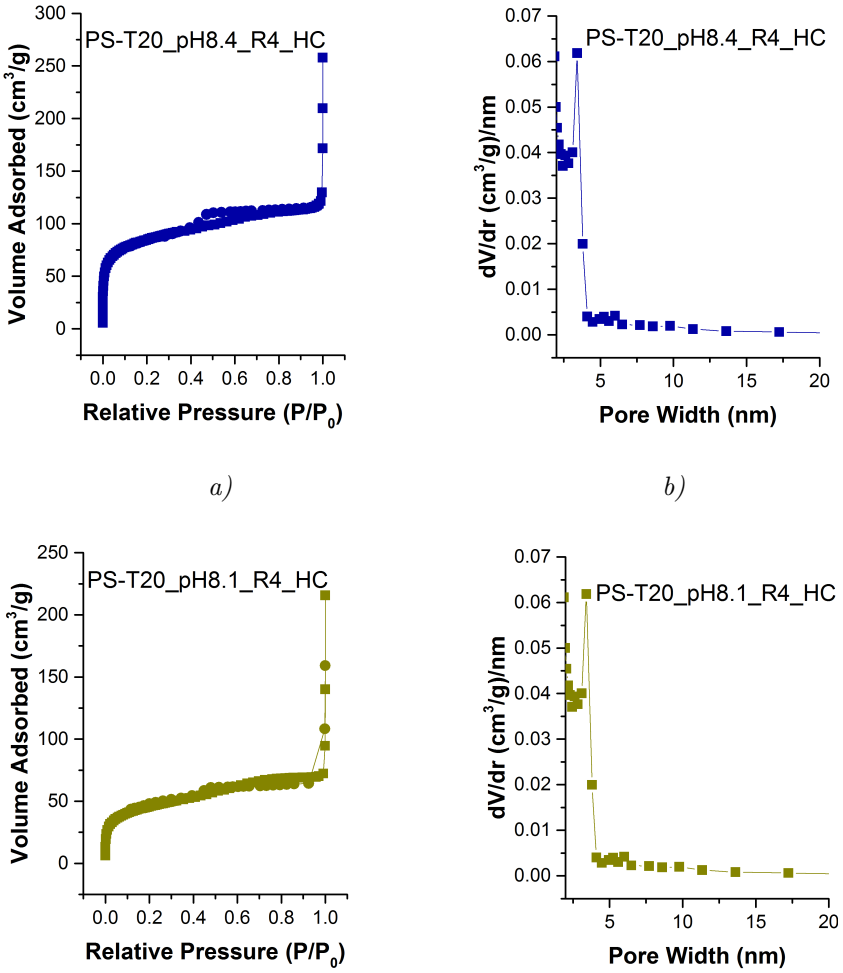


***Figure 5.14*** *Isotherms and pore size distributions for the samples PS-T20_pH8.4_R4_HC (a-b) and PS-T20_pH8.1_R4_HC (c-d).*

## 5.5 Reusing the Supernatant as the Reaction Medium

Upon vacuum filtration of the slurry, a supernatant (containing $NH_3$, $NH_4F$, and dissolved nonfilterable $SiO_2$) is obtained which can be utilized as an alternative reaction medium in the framework of industrial process. In this sense, the syntheses reported in this section consisted in simultaneously adding a 22 % $NH_3$ solution and a 23 % FSA solution into the supernatant in such a way that pH would not drift from the range (initial pH ± 0.1). Before trying the syntheses directly in the reactor, a series of attempts were performed in a plastic beaker to assess beforehand the apt flow rates of $NH_3$ and FSA *via* a trial-and-error procedure. As a rule of thumb, pH values had to remain stable during the syntheses for at least 60 minutes before deemed suitable to be reproduced in the reactor. The investigated pH values were 8.4 and 8.1.

It ought to be remarked again that the supernatant used during these experiments contain dispersible nonfilterable silica. Consequently, nucleation process may be affected as $SiO_2$ in solution can serve as nucleation centres and possible differences can be detected when compared with pristine-nucleation derived silica. In this sense, the main purpose of these experiments is to show the feasibility of using supernatant as reaction *medium*. Usual characterizations were carried out as ever, instrumental in drawing a comparison with the samples obtained *via* the usual synthetic procedure (section 5.3.1). The samples were labelled by adding the ending SN.

### 5.5.1 Experimental

Before the synthesis, supernatant pH was adjusted to reach the desired initial values by adding either $NH_3$ and/or HF. Then, 200 mL of the so-adjusted supernatant was put into the reactor, cooled by flowing room temperature mains water. Stirring was set at 200 rpm, as usual. Addition of FSA and ammonia was performed by using two peristaltic pumps as pictured in Figure 5.15 and was interrupted after exactly 60 minutes.

Flow rates for FSA and $NH_3$ set during the experiments are reported in Table 5.9. Please note that addition rates are here given in mass of solution *per* minute (g $min^{-1}$) instead of the customary volume of solution *per* minute (mL $min^{-1}$).

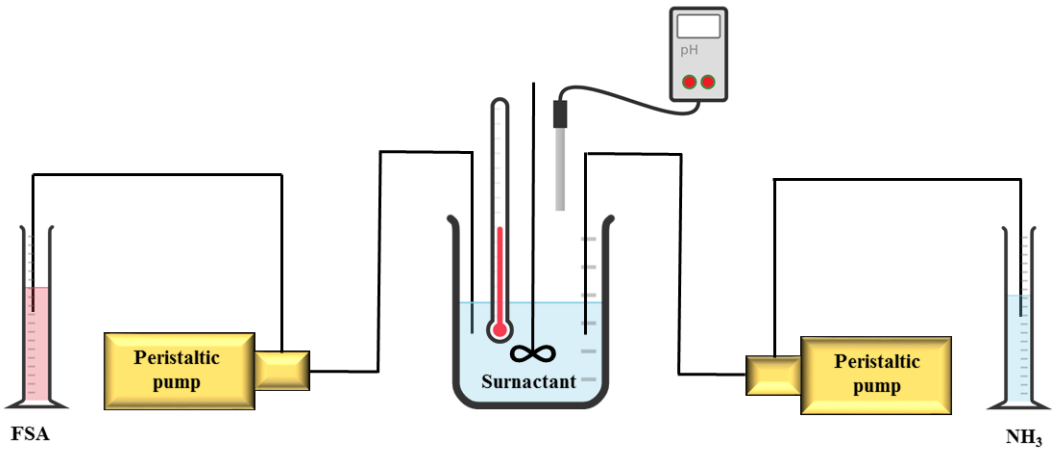


***Figure 5.15*** *Simplified diagram of the equipment used for the synthesis of precipitated silica by using a supernatant as the reaction medium.*

This change in unit of measure is justified by mere practical reasons during the trial-and-error phase of these experiments.

***Table 5.9*** *Flow rates for 23 % FSA and 22 % $NH_3$ in the syntheses with supernatant as reaction medium. Flow rates are expressed as mass of solution supplied per minute.*

| Sample | 23 % FSA flow rate (g $min^{-1}$) | 22 % $NH_3$ flow rate (g $min^{-1}$) | Duration (min) |
|---|---|---|---|
| **PS-T20_pH8.4_SN** | 1.8 | 1.1 | 60 |
| **PS-T20_pH8.1_SN** | 2.1 | 1.0 | 60 |

After the simultaneous addition of the two reactants, the resulting slurry underwent the usual ninety minute post-synthesis stirring while pH was monitored with regular measurements. $SiO_2$ was then recovered by filtration, dried, and characterized. Table 5.10 report the results of these analyses while figure 5.16 depicts the **$N_2$-physisorption** isotherms with pore size distributions, respectively.

The samples obtained using the supernatant of previous syntheses as reaction medium differ from those synthesized through the customary "titration" method at the same pH and temperature, especially in the case of the sample synthesized at pH = 8.4. In particular, surface area is lower in PS-T20_pH8.4_SN (213 $m^2$ $g^{-1}$) than in similarly synthesized sample such as PS-T20_pH8.4_R4 and PS-T20_pH8.4_HC ($\geq$ 250 $m^2$ $g^{-1}$). A decrease in microporous ad mesoporous contribution is also observed in favour of macroporosity.

***Table 5.10*** *Supernatant use effect on precipitated $SiO_2$ synthesis from simultaneous addition of 23 % FSA solution and 22 % $NH_3$ solution with final pH of 8.1 and 8.4. Calculated mean values are also reported with the standard deviation.*

| Sample | Yield (%) | Ratio $NH_3$/FSA (mol/mol) | LoI (%) | Surface Area ($m^2$ $g^{-1}$) |
|---|---|---|---|---|
| **PS-T20_pH8.4_SN (1)** | 73.2 | 4.8 | 10.3 | 213 |
| **PS-T20_pH8.4_SN (2)** | 74.5 | 4.8 | 10.1 | 209 |
| **PS-T20_pH8.4_SN (3)** | 73.7 | 4.8 | 10.0 | 215 |
| **PS-T20_pH8.4_SN (Mean)** | 73.8 ± 0.7 | 4.8 | 10.1 ± 0.2 | 212 ± 3.1 |
| **PS-T20_pH8.1_SN (1)** | 70.7 | 5.5 | 10.6 | 199 |
| **PS-T20_pH8.1_SN (2)** | 71.8 | 5.5 | 10.9 | 189 |
| **PS-T20_pH8.1_SN (3)** | 71.4 | 5.5 | 10.4 | 195 |
| **PS-T20_pH8.1_SN (Mean)** | 71.3± 0.6 | 5.5 | 10.6 ± 0.3 | 194 ± 5.0 |

*Relative standard deviation: %RSD($S_{BET}$)=2.1%.*

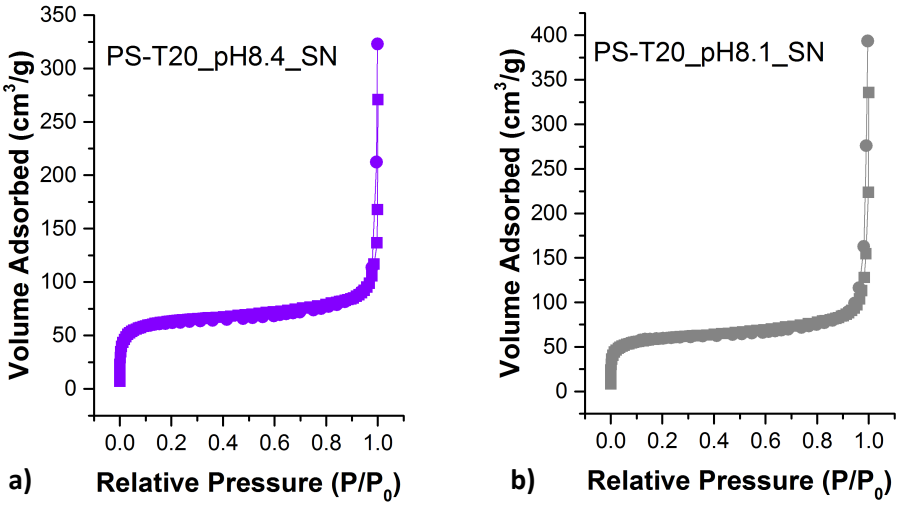


***Figure 5.16*** *Isotherms of the samples a) PS-T20_pH8.4_SN b) and PS-T20_pH8.1_SN.*

Conversely, **LoI** values are fairly similar. As for PS-T20_pH8.1_SN, its surface area value is actually similar to PS-T20_pH8.1_SN (about 200 $m^2$ $g^{-1}$) but not to PS-T20_pH8.1_R4_HC (286 $m^2$ $g^{-1}$). However, lower mesoporous and macroporous contributions were found for PS-T20_pH8.1_SN (Tables 5.3 and 5.8). The differences between "titration" and supernatant sample may be ascribable to the fact that the nucleation events in the reactions carried out in the supernatant are not "original". In other words, it is possible that the soluble silica particles contained in the supernatant might serve as the actual non-original nucleation *loci* instead of the freshly formed silica nucleation centres in the "titration" syntheses. However, the study of this phenomenon lies outside the scope of this thesis and should be dealt with separately.

In conclusion, figure 5.17 report the specific surface area of all the samples synthesized in this chapter. The graph highlights that the most promising are those prepared at low temperature, in particular concerning the range of values of specific surface area obtainable by ending the addition of FSA to reach a given value of pH. In fact, at pH values of 8.4 and 8.1, the samples show high surface area (up to 256 $m^2$ $g^{-1}$) while at 7.8 a surface area value of 81 $m^2$ $g^{-1}$ was obtained. However, for the intended application, all the three samples result to be promising and, therefore, chosen to prepare the tread compounds.

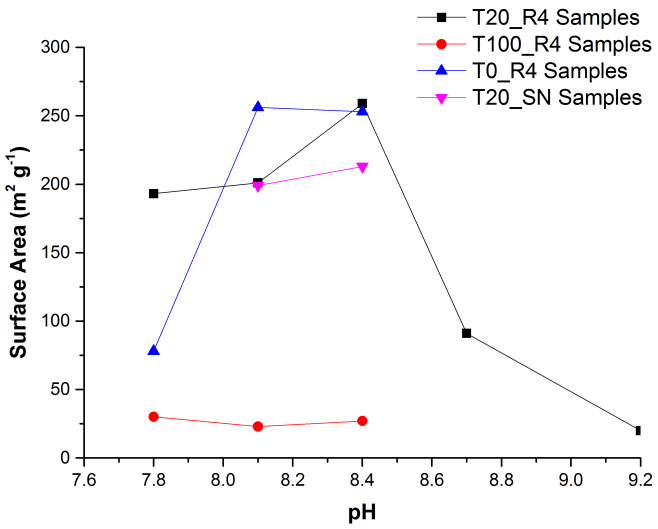


***Figure 5.17*** *Specific surface area values of the samples synthesized described in this chapter.*

## 5.6 Tests of Tread Compounds

### 5.6.1 Sample Choice

The batches of experiments described so far were instrumental in obtaining silica of apt surface area values to be used as reinforcing agents in the tyre industry. The samples deemed to be suitable for the preparation of the tread compounds were the ones that, despite being synthesized in similar experimental conditions, feature a relatively wide range of surface area within the commonly agreed range given in the literature[8] (from 125 to 250 $m^2$ $g^{-1}$) in any case. This choice was made to assess performance differences in tear compounds behaviour obtained using $SiO_2$ synthesized in fairly similar situation but showing different textural properties. The samples that met these requirements were found in the three from the T0 (low temperature) series (section 5.3.3). In fact, these samples feature a range of values of surface area ranging between 81 and 256 $m^2$ $g^{-1}$, and uniform values of **LoI**.

***Table 5.11*** *Characterization of the samples chosen for the preparation of tread compounds.*

| Sample | Yield (%) | Ratio $NH_3$/FSA (mol/mol) | LoI (%) | Surface Area ($m^2$ $g^{-1}$) | Mean Pore Size (nm) |
|---|---|---|---|---|---|
| **PS-T0_pH8.4_R4** | 66.8 | 5 | 6.1 | 253 | 3.5 |
| **PS-T0_pH8.1_R4** | 65.2 | 4.3 | 6.8 | 256 | 3.4 |
| **PS-T0_pH7.8_R4** | 64.7 | 3.5 | 6.1 | 81 | 3.1 |

*Relative standard deviation: %RSD($S_{BET}$)=2.1%; ; %RSD (Mean Pore Size)=1.8%*

The characterization already performed on these three samples was complemented by **TGA** analysis, both on wet and dried fraction, as reported on Figure 5.18 and Table5.12.

### 5.6.2 Preparation of the Tread Compounds

Preparation of the tread compounds was performed in the laboratories of the University of Milan "Bicocca" led by Prof. Roberto Scotti in collaboration with the University of Milan "Statale", in virtue of a shared instrumentation agreement, and the Pirelli Research Centre where vulcanization and the actual

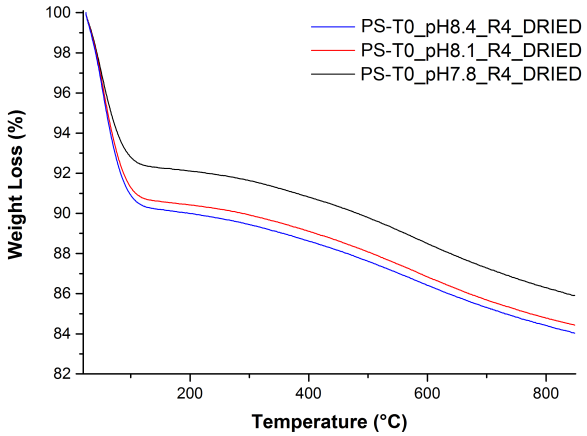


***Figure 5.18*** *Thermogravimetric analysis of the samples used for the preparation of the tread compounds upon drying.*

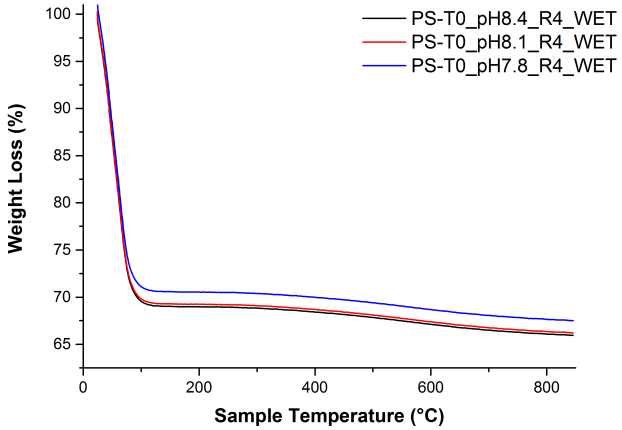


***Figure 5.19*** *Thermogravimetric analysis of the wet samples used for the preparation of the tread compounds.*

***Table 5.12*** *Weight loss over thermogravimetric analysis of the samples (dried and wet) used in the preparation of the tread compounds.*

| Sample | Weight Loss at 150 °C (%) | Weight Loss (150 ° - 850 °C) (%) | Cumulative Weight Loss (%) |
|---|---|---|---|
| **PS-T0_pH8.4_R4_DRIED** | 9.81 | 6.41 | 15.97 |
| **PS-T0_pH8.4_R4_WET** | 30.98 | 3.09 | 34.07 |
| **PS-T0_pH8.1_R4_DRIED** | 9.41 | 6.16 | 15.57 |
| **PS-T0_pH8.1_R4_WET** | 30.71 | 3.11 | 33.82 |
| **PS-T0_pH7.8_R4_DRIED** | 7.74 | 6.36 | 14.10 |
| **PS-T0_pH7.8_R4_WET** | 29.42 | 3.25 | 32.67 |

testing phase were carried out.

The tread compounds were prepared using the same compounding rubber (KER® 1500) and following the same recipe. KER® 1500 is a standard grade styrene-butadiene, produced by emulsion copolymerization based on soaps of rosin and fatty acids containing 23.5 % of chemically bonded styrene.[9] They were then compared with another tread compound obtained in the same manner by adding a commercially available reinforcing silica named Rhodia-Zeosil®, a highly dispersible precipitated silica produced by Solay and obtained from sodium silicate through its reaction with sulfuric and hydrochloric acids. Typical surface area ranges from 115 to 215 $m^2$ $g^{-1}$.[10]

The four tread compounds were prepared by mixing with a Brabender®:

- 11 g of precipitated $SiO_2$;
- 0.9 g of a silane coupling agent;
- 31.5 g of KER® 1500, divided in approximately 1 cm pieces;
- 0.7 g of stearic acid, as a softener and filler-dispersing agent;
- 0,7 g of 6PPD: an antioxidant agent, N-(1,3-Dimethylbutyl)-N'-phenyl-p-phenylenediamine;
- 1.1 g of ZnO as a vulcanization activator.

***Table 5.13*** *Relative composition expressed in percentage by weight per component of the prepared tread compounds.*

| Component | (% w/w) |
|---|---|
| $SiO_2$ | 24.0 |
| Silane Coupling Agent | 2.0 |
| KER® 1500 | 68.5 |
| Stearic Acid | 1.5 |
| 6PPD | 1.5 |
| ZnO | 2.5 |

Temperature and mixing speed were set at 145 °C and 60 rpm, respectively. Mixing was performed for 10 minutes. Force applied by the mixer was set at 25 N·m.

### 5.6.3 Finalizing the Preparation for the Vulcanization

To be effectively vulcanized, sulfur and a vulcanization accelerator (such as CBS, N-cyclohexyl-2-benzothiazole sulfenamide) must be incorporated into the so-obtained tread compounds. For this reason, Brabender was used setting temperature at 95 °C and mixing speed at 60 rpm. Three quarters of the compound was coarsely divided and laid into the mixing unit of the Brabender. After 10 minutes, 0.6 g of sulfur and 0.9 g of CBS were added. After another ten minutes, the mixing was stopped and the vulcanization-ready tread compound was recovered.

The tread compounds were vulcanized in the facilities located at the Pirelli Research Centre in Milan and then tested. Unfortunately, the details and the results of these tests are considered sensitive information and will not be disclosed here.

*The research activity described in this chapter was carried out at Fluorsid S.p.A. over a period of twelve months.*

# References

[1] Pala, L. and Lavanga, M. High Purity Synthetic Fluorite, Process for Preparing the Same and Apparatus Therefor., WO 2016/156969 A1.

[2] Eyal, A. M. Recovery of Ammonia and Hydrogen Fluoride from Ammonium Fluoride Solutions., 0-286-449-A1.

[3] Yu, H. S.; Rhee, K.-I.; Lee, C. K.; Yang, D.-H. Two-Step Ammoniation of By-Product Fluosilicic Acid to Produce High Quality Amorphous Silica. *Korean Journal of Chemical Engineering* **2000**, *17*, 401–408, ISSN: 1975-7220, DOI: https://doi.org/10.1007/BF02706850.

[4] Sing, K. S. W. Reporting Physisorption Data for Gas/Solid Systems with Special Reference to the Determination of Surface Area and Porosity (Recommendations 1984). *Pure and Applied Chemistry* **1985**, *57*, 603–619, DOI: https://doi.org/doi:10.1351/pac198557040603.

[5] Rouquerol, F.; Rouquerol, J.; Sing, K. In *Adsorption by Powders and Porous Solids*, Rouquerol, F., Rouquerol, J., Sing, K., Eds.; Academic Press: London, 2014, pp 439–447, ISBN: 978-0-12-598920-6, DOI: https://doi.org/10.1016/B978-012598920-6/50007-5.

[6] Iler, R. K., *The Chemistry of Silica*; Wiley: 1979, ISBN: 047102404X.

[7] Wilhelm, S.; Kind, M. Influence of pH, Temperature and Sample Size on Natural and Enforced Syneresis of Precipitated Silica. *Polymers* **2015**, *7*, 2504–2521, ISSN: 2073-4360, DOI: https://doi.org/10.3390/polym7121528.

[8] Hewitt, N.; Ciullo, P., *Compounding Precipitated Silica in Elastomers: Theory and Practice*; Plastics Design Library; Elsevier Science: 2007, ISBN: 9780815516538.

[9] Synthos Rubbers KER® 1500 Styrene-Butadiene Rubber-ESBR. https://www.synthosrubbers.com/fileadmin/user_files/rubbers/pdf/eng/esbr/TDS_en_KER_1500_1000757.pdf.

[10] Kopylov, V. M.; Kostyleva, E. I.; Kostylev, I. M.; Koviazin, A. V. Silica Fillers for Silicone Rubber. *International Polymer Science and Technology* **2011**, *38*, 35–47, DOI: https://doi.org/10.1177/0307174X1103800408.

# 6

# MCM-41 from FSA

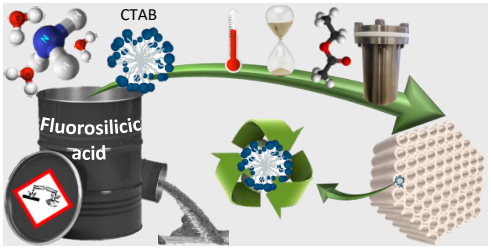


*In this chapter, industrial waste hexafluorosilicic acid ($H_2SiF_6$ or FSA) has been proven to be an economical alternative to the most common Si-precursos (such as, TEOS and TMOS) in the synthesis of MCM-41. To assess the feasibility of its utilization in lieu of these silicate esters, a head-to-head comparison was carried out between tetraethylorthosilicate (TEOS) and FSA, exploring the effect of different parameters such as temperature, time, hydrothermal treatment, and the presence of ethyl acetate by studying the textural, structural, and morphological features of the resulting materials. Moreover, in the perspective of envisaging a completely zero-waste approach, a recovery processes of the templating agent have been proposed.*

## 6.1 Introduction

Silicon-containing materials (such as, precipitated and mesostructured silica along with zeolites) have attracted a great deal of interest for their variety of possible applications.[1–4] Among these, mesostructured materials stand out as

high value-added products with their unique textural properties, epitomized by high surface area, high pore volume values, regular pore distribution, and pore diameter between 2-50 nm.[5] In particular, the utilization of M41S mesoporous materials has been proposed in applications ranging from drug delivery, chromatography, catalysis, to environmental remediation. Among the various industrial wastes from which synthesis of siliceous mesostructured materials may be possible, FSA represents an ideal liquid reactant that can be used without any other pretreatments, both for silicon- and fluoride-based compounds. To the best of our knowledge, only one study[2] has been carried out for the synthesis of MCM-41 materials from FSA. In this study, Liu *et al.* reported the synthesis of FSA-derived MCM-41 and Ti-containing MCM-41, focusing on the preparation of efficient Ti-containing MCM-41 catalysts for cyclohexene epoxidation to produce cyclohexene oxide.

The aim of the work described in this chapter is twofold: demonstrating the feasibility of utilizing FSA in the synthesis of high value-added materials such as MCM-41 and assessing the ability of FSA to effectively replace TEOS in the synthesis of such materials. It was performed by drawing a direct head-to-head comparison of the properties between TEOS- and FSA-derived MCM-41 when some experimental variables, such as temperature, reaction duration, presence of acetyl acetate, and hydrothermal treatment were changed. It ought to be stated that the reaction mechanisms involved in the manufacture of TEOS- and FSA-derived MCM-41 are quite different. While MCM-41 from TEOS involves a base-catalysed reactions of the precursor as reported in Eq. 23-25, polymerization of $SiO_2$ by using FSA as precursor is actually brought about by neutralization reactions in which the base does not serve as a mere catalyst, but as a stoichiometric reactant. This reaction is exemplified in Eq. 26-27.

$$\equiv\mathrm{Si}-\mathrm{OR} + \mathrm{H_2O} \overset{\text{hydrolysis}}{\rightleftharpoons} \equiv\mathrm{Si}-\mathrm{OH} + \mathrm{ROH} \qquad (\textbf{Eq. } 23)$$

$$\equiv\mathrm{Si}-\mathrm{OH} + \mathrm{HO}-\mathrm{Si}\equiv \overset{\text{water cond}\cdot}{\rightleftharpoons} \equiv\mathrm{Si}-\mathrm{O}-\mathrm{Si}\equiv + \mathrm{H_2O} \qquad (\textbf{Eq. } 24)$$

$$\equiv\mathrm{Si}-\mathrm{OR} + \mathrm{HO}-\mathrm{Si}\equiv \overset{\text{alcohol cond}\cdot}{\rightleftharpoons} \equiv\mathrm{Si}-\mathrm{O}-\mathrm{Si}\equiv + \mathrm{ROH} \qquad (\textbf{Eq. } 25)$$

$$\mathrm{H_2SiF_6} + 2\,\mathrm{NH_4OH} \longrightarrow (\mathrm{NH_4})_2\mathrm{SiF_6} + 2\,\mathrm{H_2O} \qquad (\textbf{Eq. } 26)$$

$$(\mathrm{NH_4})_2\mathrm{SiF_6} + 4\,\mathrm{NH_4OH} \longrightarrow \mathrm{SiO_2} + 6\,\mathrm{NH_4F} + 2\,\mathrm{H_2O} \qquad (\textbf{Eq. } 27)$$

## 6.2 Exploratory Synthesis of MCM-41 from FSA

The first attempts to synthesize MCM-41 from FSA reported hereinafter are based upon previous research developed by the author's research group,[6,7] and the same synthetic route was followed by replacing TEOS with $H_2SiF_6$. Table 6.1 and the flowchart in figure 6.1 schematizes all the samples synthesized in this chapter.

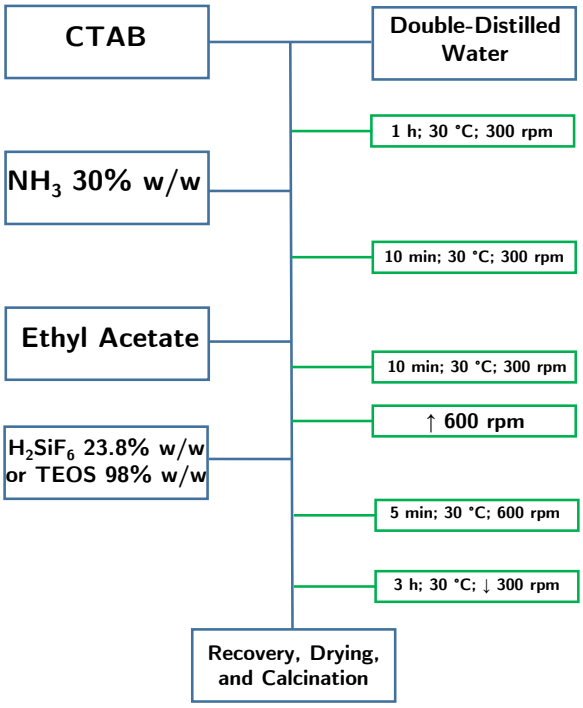


***Figure 6.1*** *Flowchart of the explorative synthesis of MCM-41 from $H_2SiF_6$ and TEOS.*

***Table 6.1*** *Reactants and experimental conditions used in the preliminary syntheses.*

| Reactant | Volume (mL) | Mass (g) | Mass Quantity (mol) | Molar Ratio |
|---|---|---|---|---|
| **CTAB** | - | 1 | $2.74 \cdot 10^{-3}$ | 1 |
| **$H_2O$** | 200.00 | 200.00 | 11.10 | $\sim$ 4400 |
| **$NH_3$ 30 %** | 21.00 | 18.06 | 0.33 | 120 |
| **Ethyl Acetate 99.9 %** | 3.85 | 3.47 | $3.84 \cdot 10^{-2}$ | 14 |
| **$H_2SiF_6$ 23.8 %** | 7.37 | 9.00 | $1.64 \cdot 10^{-2}$ | 6 |
| **TEOS 98 %** | 3.79 | 3.43 | $1.64 \cdot 10^{-2}$ | 6 |

This synthesis was carried out as follows: one gram of CTAB (hexadecyltrimethylammonium bromide) was dissolved in 200 mL of double-distilled water and the resulting solution was stirred at 300 rpm for one hour at 30 °C. Then, 21 mL of a 30 % w/w solution of $NH_3$ was added. Ten minutes later, 3.85 mL of ethyl acetate was added and the resulting solution was

left under stirring for further 10 minutes. Afterwards, stirring rate was increased to 600 rpm and 9.0 g of a 23.8 % solution of $H_2SiF_6$ was injected into the reaction mixture all at once. Stirring at 600 rpm was kept for five minutes and then decreased again to 300 rpm, with the reaction mixture being left to react for three hours. The solid was recovered by centrifugation at 4500 rpm for five minutes, washed with three 75 mL aliquots of a 1:1 mixture of double-distilled water/ethanol, and finally dried in an oven at 60 °C overnight. Subsequent calcination was performed at 550 °C for four hours with a heating rate of 2 °C $min^{-1}$. A parallel synthesis under the same experimental conditions was performed using TEOS as the siliceous precursor. In both cases, very good and similar yields were achieved for both the sample 92 % and 93 % for TEOS and FSA, respectively.

### 6.2.1 Characterization

The calcined products were characterized by **Small-Angle XRD**, to reveal the mesostructured nature of the materials, **$N_2$-physisorption**, to study the textural properties, and **TEM** analysis, to asses the morphological properties and to verify the formation of ordered porous structures.
**SA-XRD** patterns of the two samples, shown in figure 6.2a, feature the three reflexes of a MCM-41 material namely, from left to right, (100), (110), and (200) typical of a 2-D hexagonal porous structure (P6mm). **$N_2$-physisorption** measurements are reported in figure 6.2b in which both the ad-/desorption isotherms feature the classic shape of a IVb isotherm. Lastly, figure 6.2c depicts their pore size distributions. Table 6.2 reports the textural properties, highlighting the close similarities between the two samples: very high surface area (about 1100 $m^2$ $g^{-1}$), narrow bimodal pore size distributions centred at about (2.6; 3.0) and (2.5; 3.1) nm for TEOS_MCM41 and FSA_MCM41, respectively, and similar $V_p$, $d_{100}$, $a_0$, and wall thickness ($w_t$) values.

In order to gauge pore size distribution, it ought to be acknowledged that the DFT model was used throughout this work. To compare these results with those obtained *via* the BJH model, whose adoption is likewise widespread in the literature, a comparison between the two models was drawn.

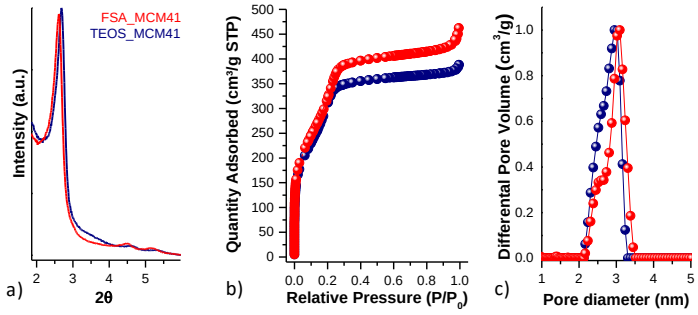


***Figure 6.2*** *a) SA-XRD, b) $N_2$-physisorption isotherms, and c) DFT-calculated pore size distributions of the samples TEOS_MCM41 and FSA_MCM41.*

***Table 6.2*** *Surface area ($S_{BET}$), pore volume ($V_p$), DFT-calculated pore diameter ($D_{P(DFT)}$), lattice spacing ($d_{100}$), hexagonal unit cell parameter ($a_0$), and wall thickness ($w_t$) of the materials during the tentative syntheses from TEOS and FSA 30 °C.*

| Sample | T (°C) | t (h) | $S_{BET}$ ($m^2$ $g^{-1}$) | $V_P$ ($cm^3$ $g^{-1}$) | $D_{P(DFT)}$ (nm) | $d_{100}$ (nm) | $a_0$ (nm) | $w_t$ (nm) |
|---|---|---|---|---|---|---|---|---|
| **TEOS_MCM41** | 30 | 3 | 1110 | 0.6 | (2.6; 3.0) | 3.3 | 3.8 | (1.2; 0.8) |
| **FSA_MCM41** | 30 | 3 | 1158 | 0.7 | (2.5; 3.1) | 3.4 | 3.9 | (1.4; 0.8) |

*Relative standard deviation: %RSD($S_{BET}$)=2.1%; %RSD ($V_p$)=1.1%; %RSD (Dp)=1.8%. $d_{100}$ and $a_0$ were obtained from XRD data. For bimodal pore size distributions, two values of $D_{p(DFT)}$ are provided.*

As can be easily seen in figure 6.3, the BJH-calculated pore size distributions for both the samples are shifted towards lower values if compared with the DFT-calculated ones. The BJH model, usually performed by taking into account the desorption branch of the isotherm, posits that materials have cylinder-like pores in which multilayer adsorption may result in capillary condensation and the pressure at which this phenomenon occurs is determined by pore size. Although this assumption describes the real adsorption-desorption process in most mesoporous materials, the sizes estimated from BJH normally have a relatively large difference with the actual one, especially with pore sizes smaller than 5 nm.[5] Conversely, density functional theory (DFT), estimates pore distribution through a molecular-level description of nonuniform fluid behaviours for adsorbate species confined in the pores and correlates the properties of gas molecules with their adsorption performance in pores of different size whereas BJH method is based on Kelvin equation. As a consequence, underestimation may be as large as 20 % and, concerning mesoporous materials, it could be even more significant.[5] Being this the case, pore size distributions assessed in this

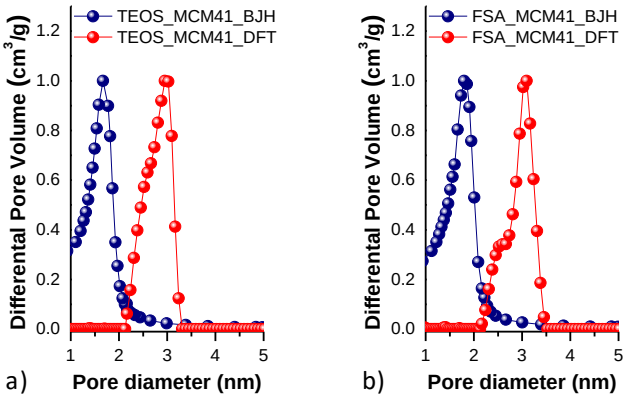


***Figure 6.3*** *Pore size distributions of the samples a) TEOS_MCM41 (TEOS_T30_3h_EA) and b) FSA_MCM41 (FSA_T30_3h_EA) calculated with the BJH (red) and DFT (blue) models.*

work were calculated by using the DFT model, which is based on the molecular modelling of the interaction between the adsorbate and the adsorbent surface.

**TEM** analysis was also performed (figure 6.4a, c, and e for the TEOS-derived sample and 6.4b, d, and f for its FSA-derived counterpart). Low magnification micrographs of the sample TEOS_MCM41 depict regular cylindrical-shaped sub-micrometric particles (about 300 nm widthwise and about 550 nm lengthwise, figure 6.4g), whereas FSA_MCM41 features rounded, hexagonal, or seed-shaped sub-micrometric particles with an average particle size about 220 nm with a broad particle size distribution (figure 6.4h). In spite of the different morphologies, high magnification images confirm the well-defined mesoporous order in both the samples (figures 6.4e and 6.4f).

These preliminary results have proven that FSA can be effectively used as a precursor in order to obtain high quality MCM-41 and spurred the set up of a series of experiments involving a systematic comparison between TEOS- and FSA-derived MCM-41 materials synthesized under a variety of experimental conditions with the purpose of assessing whether FSA might be able to effectively replace TEOS in the synthesis of MCM-41.

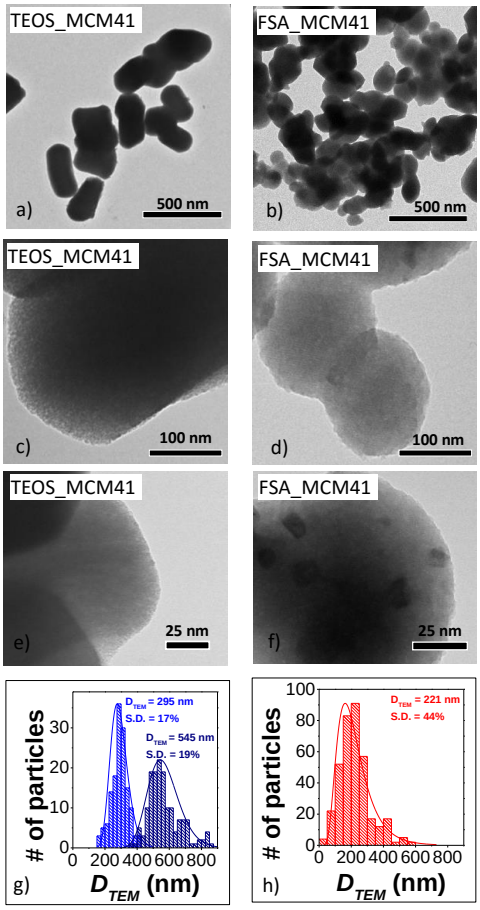


***Figure 6.4*** *TEM micrographs at different magnifications of the samples TEOS_MCM41 (a, c, and e) and FSA_MCM41 (b, d, and f), along with their respective particle size distributions (g for TEOS_MCM41 and h for FSA_MCM41).*

## 6.3 Studying the Effects of Different Synthetic Parameters

MCM-41 from TEOS and the effect of different parameters such as temperature, reaction time, hydrothermal treatment, pH, ratio between TEOS and CTAB, and ethyl acetate have been widely studied.[5,8] However, as an analogous comparison with FSA has been never reported, to the best of our knowledge, a systematic study on MCM-41 from FSA was carried out by changing various synthetic parameters. The so-obtained FSA-derived materials were then compared with their TEOS-derived counterparts. The flowchart in figure 6.5 and the table 6.3 summarizes the experimental conditions here adopted.

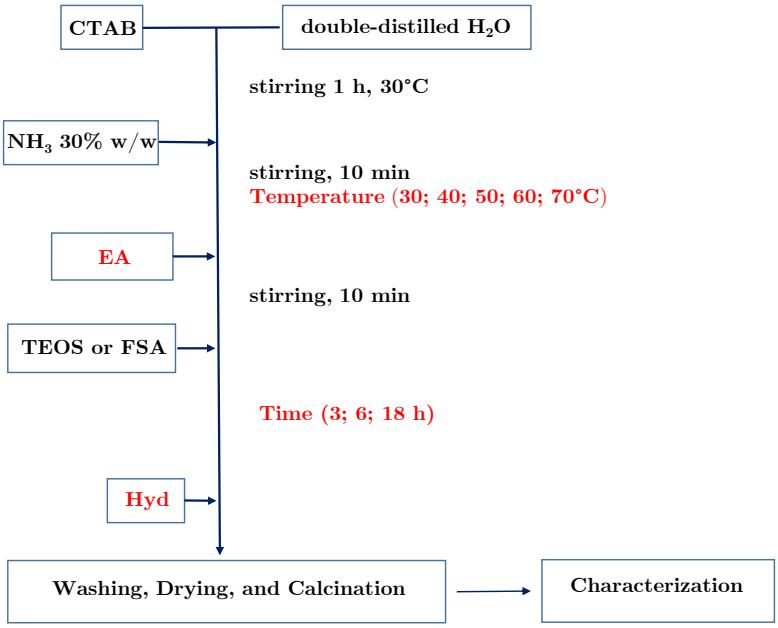


***Figure 6.5*** *Flowchart depicting the sets of the experiments for the TEOS/FSA comparison. The parameters investigated are written in red. EA=ethyl acetate, Hyd=hydrothermal treatment.*

***Table 6.3*** *Synthesis conditions adopted for the preparation of the silica samples: reaction temperature (T), reaction time (t), ethyl acetate (EA), and hydrothermal treatment (Hyd), with the indication of their use (X) or not (-) .*

| Sample | T (°C) | t (h) | EA | Hyd |
|---|---|---|---|---|
| **TEOS_MCM41 (TEOS_T30_3h_EA)** | **30** | 3 | X | - |
| **FSA_MCM41 (FSA_T30_3h_EA)** | **30** | 3 | X | - |
| **TEOS_T40_3h_EA** | **40** | 3 | X | - |
| **TEOS_T50_3h_EA** | **50** | 3 | X | - |
| **TEOS_T60_3h_EA** | **60** | 3 | X | - |
| **TEOS_T70_3h_EA** | **70** | 3 | X | - |
| **FSA_T40_3h_EA** | **40** | 3 | X | - |
| **FSA_T50_3h_EA** | **50** | 3 | X | - |
| **FSA_T60_3h_EA** | **60** | 3 | X | - |
| **FSA_T70_3h_EA** | **70** | 3 | X | - |
| **TEOS_T50_6h_EA** | 50 | **6** | X | - |
| **TEOS_T50_18h_EA** | 50 | **18** | X | - |
| **FSA_T50_6h_EA** | 50 | **6** | X | - |
| **FSA_T50_18h_EA** | 50 | **18** | X | - |
| **TEOS_T50_3h_EA_Hyd** | 50 | 3 | X | X |
| **FSA_T50_3h_EA_Hyd** | 50 | 3 | X | X |
| **FSA_T50_3h** | 50 | 3 | - | - |
| **TEOS_T50_3h_ Hyd (NMR_MCM41_TEOS)** | 50 | 3 | - | X |
| **FSA_T50_3h_ Hyd (NMR_MCM41_FSA)** | 50 | 3 | - | X |

## 6.4 Effect of Temperature

When choosing the temperature whereby carry out soft-templating syntheses, two parameters involving the templating agent are considered to be important: the critical micellar temperature (CMT) and the cloud point (CP). CMT is the minimum temperature for a given surfactant to form micelles, which is usually low in cationic surfactant such as CTAB, making synthesis at room temperature possible. Cloud point, instead, is defined as the temperature at which phase-separation of the mixture solvent-surfactant occurs. After synthesizing MCM-41 from either TEOS or FSA at the temperature of 30, 40, 50, 60, and 70 °C and allowing the reaction to continue after the injection of the siliceous precursor, the samples were thoroughly characterized.

**SA-XRD** patterns for all the samples synthesized form either TEOS or FSA (6.6a) feature the three typical peaks ((100), (110), and (200)) of a highly ordered hexagonal structure. As for MCM-41 deriving from TEOS (Figure 6.6a), the results indicate that the samples obtained at 30 and 40 °C show similar patterns with a narrow (100) peak. By increasing the temperature, the peaks move towards lower values of $2\theta$ with the co-occurring broadening of the main peak. **$N_2$-physisorption** analyses further confirm the similarities between the samples synthesized at 30 and 40 °C with comparable values of specific surface area, pore volume, and a bimodal pore size distribution. At 50 °C, unimodal pore size distribution was achieved along with a slight decrease in specific surface area and an increase in pore volume ($V_p$) and pore diameter ($D_p$). At 60 °C and 70 °C a bimodal pore size distribution was observed again. The sample obtained at 70 °C distinguished itself by a steep increase in the isotherm curve at high value of $P/P_0$ (close to 1), associated with intraparticle porosity.

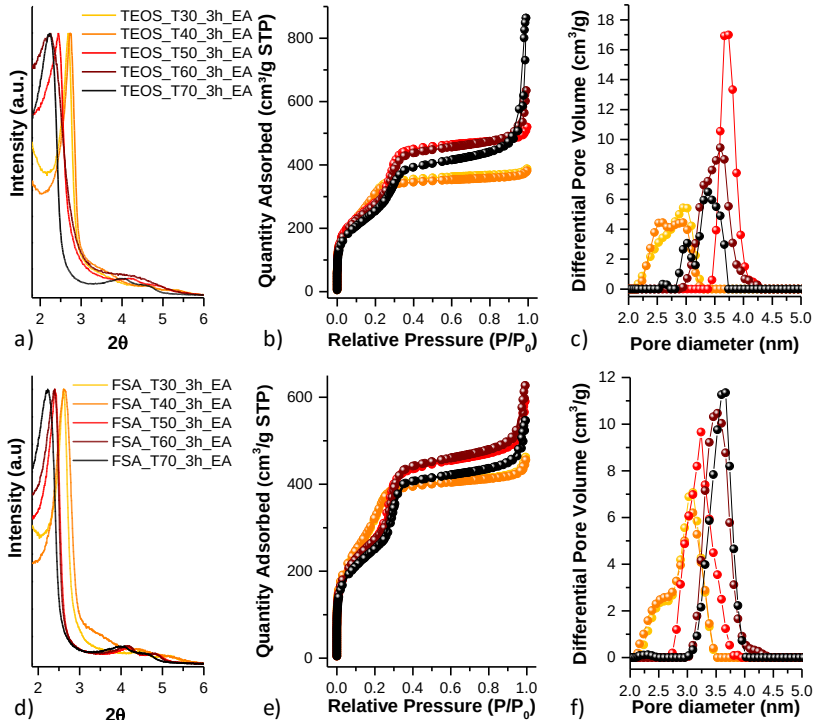


***Figure 6.6*** *(a, d) SA-XRD patterns, (b, e) $N_2$-physisorption isotherms, (c, f) and DFT-calculated pore size distributions of synthesized MCM-41 at different temperatures by using either (a-c) TEOS or (d-f) FSA.*

***Table 6.4*** *Surface area ($S_{BET}$), pore volume ($V_p$), DFT-calculated pore diameter, wall thickness ($w_t$), lattice spacing ($d_{100}$), hexagonal unit cell parameter ($a_0$), of the samples synthesized at different temperatures.*

| **TEOS** | **T (°C)** | **t (h)** | **EA** | **$S_{BET}$ ($m^2$ $g^{-1}$)** | **$V_p$ ($cm^3$ $g^{-1}$)** | **$D_{P(DFT)}$ (nm)** | **$w_t$ (nm)** | **$d_{100}$ (nm)** | **$a_0$ (nm)** |
|---|---|---|---|---|---|---|---|---|---|
| **TEOS_T30_3h_EA*** | 30 | 3 | X | 1110 | 0.6 | (2.6; 3.0) | (1.2; 0.8) | 3.3 | 3.8 |
| **TEOS_T40_3h_EA** | 40 | 3 | X | 1146 | 0.7 | (2.6; 2.9) | (1.1; 0.8) | 3.2 | 3.7 |
| **TEOS_T50_3h_EA** | 50 | 3 | X | 1021 | 0.7 | 3.8 | 0.5 | 3.7 | 4.3 |
| **TEOS_T60_3h_EA** | 60 | 3 | X | 1006 | 0.8 | 3.6 | 0.9 | 3.9 | 4.5 |
| **TEOS_T70_3h_EA** | 70 | 3 | X | 927 | 0.7 | (3.0; 3.4) | (0.9; 0.5) | 3.9 | 4.5 |
| **FSA** | **T (°C)** | **t (h)** | **EA** | **$S_{BET}$ ($m^2$ $g^{-1}$)** | **$V_p$ ($cm^3$ $g^{-1}$)** | **$D_{P(DFT)}$ (nm)** | **$w_t$ (nm)** | **$d_{100}$ (nm)** | **$a_0$ (nm)** |
| **FSA_T30_3h_EA*** | 30 | 3 | X | 1158 | 0.7 | (2.5; 3.1) | (1.4; 0.8) | 3.4 | 3.9 |
| **FSA_T40_3h_EA** | 40 | 3 | X | 1169 | 0.7 | (2.6; 3.1) | (1.3; 0.8) | 3.4 | 3.9 |
| **FSA_T50_3h_EA** | 50 | 3 | X | 933 | 0.7 | 3.4 | 0.9 | 3.7 | 4.3 |
| **FSA_T60_3h_EA** | 60 | 3 | X | 992 | 0.7 | 3.5 | 0.7 | 3.7 | 4.3 |
| **FSA_T70_3h_EA** | 70 | 3 | X | 913 | 0.6 | 3.7 | 0.9 | 4.0 | 4.6 |

** TEOS_T30_3h_EA and FSA_T30_3h_EA correspond to TEOS_MCM41 and FSA_MCM41 (see table 6.1), respectively. Relative standard deviation: %RSD($S_{BET}$)=2.1%; %RSD($V_p$)=1.1%; %RSD($D_p$)=1.8%. $d_{100}$ and $a_0$ were obtained from XRD data.*

**SA-XRD** patterns of the samples obtained from FSA (figure 6.6d) show a similar trend: by increasing the temperature, the peaks move towards lower angles with a slight broadening of the (100) peak and more discernible (110) and (200) peaks for the samples synthesized at 50 °C, 60 °C, and 70 °C. Textural proprieties were affected in the similar way the TEOS samples were. At 30 and 40 °C, a bimodal distribution was revealed with the highest specific surface areas and smallest pore diameter values found in the range from 50 to 70 °C. In the same temperature range, pore size distributions result unimodal and narrow. Therefore, 50 °C was chosen as the optimal temperature at which carry out the time-dependent experiments, being the minimum temperature at which a narrow unimodal pore size distribution was achieved in both precursors.

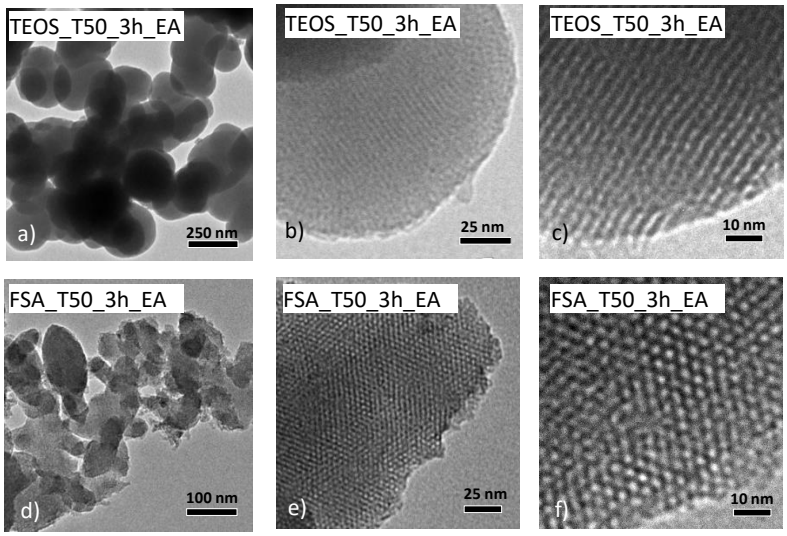


***Figure 6.7*** *TEM micrographs of the samples synthesized at 50 °C: (a-c) TEOS_ T50_ 3h_ EA and (d-f) FSA_ T50_ 3h_ EA.*

Figures 6.7a and 6.7d depict **TEM** images for the comparison between TEOS- and FSA- derived materials at the same temperature (50 °C) to verify the effect on their morphology according to the different precursor employed. In the case of TEOS (TEOS_T50_3h_EA), it is possible to verify that the increase of the temperature from 30 °C to 50 °C affected the particle shape from cylindrical to spheroidal, and the size that decreased to about 200-250 nm (figure 6.4a and c and figure 6.7j, respectively). On the contrary, no significant changes in the shape and size of the particles were observed for the FSA-derived counterpart (FSA_T50_3h_EA), still showing sub-micrometric particles of different shapes of about 200 nm (figure 6.4b and h and figure 6.7d). The images at high magnification

confirm the high degree of order in the porous system for both the samples (figure 6.7b and c and figure 6.7e and f, for TEOS and FSA, respectively).

## 6.5 Effect of Time

By comparing the textural properties of the mesoporous siliceous materials from TEOS and FSA at different reaction time (three, six, and eighteen hours) but keeping the same temperature determined in the previous set of experiments (T=50 °C), no remarkable effects were detected on both the sets of samples (figure 6.8). However, slight differences in the surface area can be revealed for the two sets but with opposite trend can be revealed for the two sets (table 6.5). As for SA-XRD patterns, TEOS-derived MCM-41 material show a slight drift towards lower values of 2θ as time reaction increases and the related increase of $d_{100}$ and $a_0$ were observed (table 6.5). Conversely, a more modest effect was observed in this sense for its FSA counterparts (figure 6.5d).

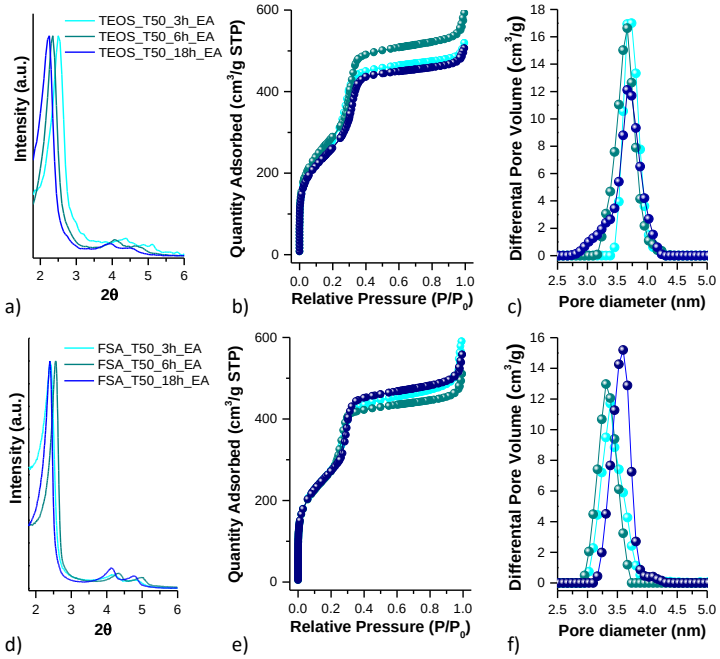


***Figure 6.8*** *SA-XRD patterns, $N_2$-physisorption isotherms, and DFT-calculated pore size distribution of MCM-41 synthesized allowing the reaction mixture to react for specified time intervals (3; 6; 18 h) using either a) TEOS (T=50 °C) or b) FSA (T=50 °C) with the addition of EA. SA-XRD patterns have been normalized for clarity's sake.*

***Table 6.5*** *Surface area ($S_{BET}$), pore volume ($V_p$), DFT-calculated pore diameter, wall thickness ($w_t$), lattice spacing ($d_{100}$), hexagonal unit cell parameter ($a_0$), of the samples synthesized at different temperatures.*

| **TEOS** | **T (°C)** | **t (h)** | **EA** | **$S_{BET}$ ($m^2$ $g^{-1}$)** | **$V_p$ ($cm^3$ $g^{-1}$)** | **$D_{P(DFT)}$ (nm)** | **$w_t$ (nm)** | **$d_{100}$ (nm)** | **$a_0$ (nm)** |
|---|---|---|---|---|---|---|---|---|---|
| **TEOS_T50_3h_EA*** | 50 | 3 | X | 1021 | 0.7 | 3.8 | 0.5 | 3.7 | 4.3 |
| **TEOS_T50_6h_EA** | 50 | 6 | X | 1005 | 0.8 | 3.7 | 0.7 | 3.8 | 4.3 |
| **TEOS_T50_18h_EA** | 50 | 18 | X | 949 | 0.7 | 3.7 | 0.8 | 3.9 | 4.5 |
| **FSA** | **T (°C)** | **t (h)** | **EA** | **$S_{BET}$ ($m^2$ $g^{-1}$)** | **$V_p$ ($cm^3$ $g^{-1}$)** | **$D_{P(DFT)}$ (nm)** | **$w_t$ (nm)** | **$d_{100}$ (nm)** | **$a_0$ (nm)** |
| **FSA_T50_3h_EA*** | 50 | 3 | X | 933 | 0.7 | 3.4 | 0.9 | 3.7 | 4.3 |
| **FSA_T50_6h_EA** | 50 | 6 | X | 983 | 0.7 | 3.4 | 0.6 | 3.4 | 4.0 |
| **FSA_T50_18h_EA** | 50 | 18 | X | 999 | 0.8 | 3.6 | 0.7 | 3.7 | 4.3 |

** TEOS_T50_3h_EA and FSA_T50_3h_EA correspond to TEOS_MCM41 and FSA_MCM41 (see table 6.4), respectively. Relative standard deviation: %RSD($S_{BET}$)=2.1%; %RSD ($V_p$)=1.1%; %RSD ($D_p$)=1.8%. $d_{100}$ and $a_0$ were obtained from XRD data. For bimodal pore size distributions, two values of $D_{p(DFT)}$ are reported.*

**TEM** micrographs at low magnification performed on FSA-derived samples (figure 6.9) show an increase in the mean dimensions of the irregularly shaped particles from about 200 nm up to about 500 nm for a reaction time going from 3 to 18 hours (FSA_T50_18h_EA). Three hours was chosen as the optimal reaction time for its practical convenience, especially considering possible applications in industrial settings.

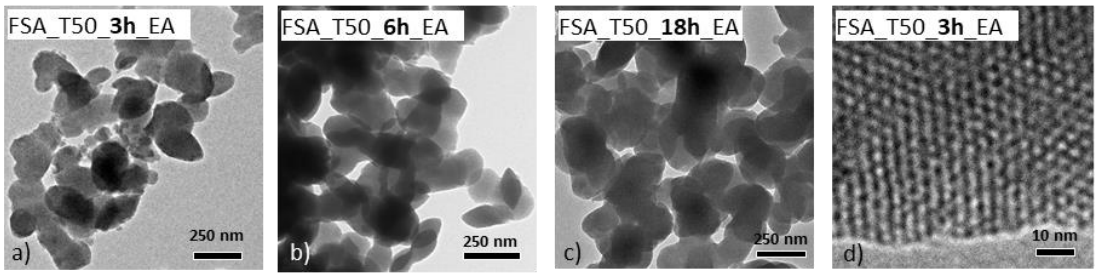


***Figure 6.9*** *TEM micrographs of MCM-41-derived from FSA synthesized at different reaction time: FSA_T50_3h_EA (a, d), FSA_T50_6h_EA (b), FSA_T50_18h_EA (c). High magnification TEM micrograph of the sample FSA_T50_3h_EA revealing the mesostructured nature of the material (d).*

## 6.6 Effect of Hydrothermal Treatment

Usually, an additional hydrothermal treatment is applied during the synthesis of the mesostructured silica in order to strengthen the porous structure. In the case of SBA-15,[9] this further treatment induces a decrease in the microporous contribution while for MCM-41 a small increase in the pore size and wall thickness, as well as an improvement in the mesoporous order, have been reported.[10] Moving in this direction, the synthetic strategy (50 °C, 3 h) was modified by adding a hydrothermal treatment at 100 °C for 18 hours. As shown in figure 6.10 and table 6.6, in both TEOS- and FSA-derived samples, the ancillary hydrothermal treatment brought about a better definition of the (110) and (200) peaks, indication of an improved order in the mesoporous structure, along with wider pores (+0.2 nm for both TEOS and FSA) with a corresponding decrease in specific surface area. TEOS_T50_3h_EA_Hyd is characterized by thicker pore walls compared with those of the untreated sample, in agreement with the literature.[10] As for the FSA-derived sample (FSA_T50_3h_EA_Hyd), wall thickness resulted to be unaffected by the hydrothermal treatment whilst pore diameter increased (from 3.4 to 3.6 nm) and pore size distribution became narrower.

***Table 6.6*** *Surface area ($S_{BET}$), pore volume ($V_p$), DFT-calculated pore diameter, wall thickness ($w_t$), lattice spacing ($d_{100}$), hexagonal unit cell parameter ($a_0$), of the samples synthesized with and without ancillary hydrothermal treatment.*

| **TEOS** | **T (°C)** | **t (h)** | **EA** | **$S_{BET}$ ($m^2$ $g^{-1}$)** | **$V_p$ ($cm^3$ $g^{-1}$)** | **$D_{P(DFT)}$ (nm)** | **$w_t$ (nm)** | **$d_{100}$ (nm)** | **$a_0$ (nm)** |
|---|---|---|---|---|---|---|---|---|---|
| **TEOS_T50_3h_EA*** | 50 | 3 | X | 1021 | 0.7 | 3.8 | 0.5 | 3.7 | 4.3 |
| **TEOS_T50_3h_EA_Hyd** | 50 | 3 | X | 996 | 0.8 | 4.0 | 0.9 | 4.2 | 4.9 |
| **FSA** | **T (°C)** | **t (h)** | **EA** | **$S_{BET}$ ($m^2$ $g^{-1}$)** | **$V_p$ ($cm^3$ $g^{-1}$)** | **$D_{P(DFT)}$ (nm)** | **$w_t$ (nm)** | **$d_{100}$ (nm)** | **$a_0$ (nm)** |
| **FSA_T50_3h_EA*** | 50 | 3 | X | 933 | 0.7 | 3.4 | 0.9 | 3.7 | 4.3 |
| **FSA_T50_3h_EA_Hyd** | 50 | 3 | X | 817 | 0.6 | 3.6 | 0.9 | 3.9 | 4.5 |

** TEOS_T50_3h_EA and FSA_T50_3h_EA correspond to TEOS_MCM41 and FSA_MCM41 (see table 6.4), respectively. Relative standard deviation: %RSD($S_{BET}$)=2.1%; %RSD ($V_p$)=1.1%; %RSD ($D_p$)=1.8%. $d_{100}$ and $a_0$ were obtained from XRD data. For bimodal pore size distributions, two values of $D_{p(DFT)}$ are reported.*

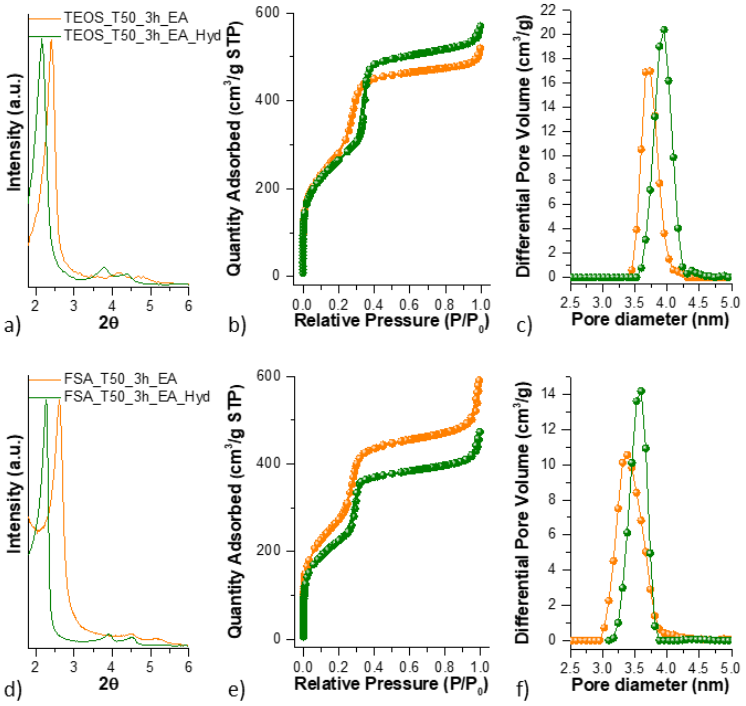


***Figure 6.10*** *(a, d) SA-XRD patterns, (b, e) $N_2$-physisorption isotherms, and (c, f) DFT-calculated pore size distributions of MCM-41 synthesized in the presence of ethyl acetate (EA), with and without hydrothermal treatment (Hyd) from either TEOS or FSA.*

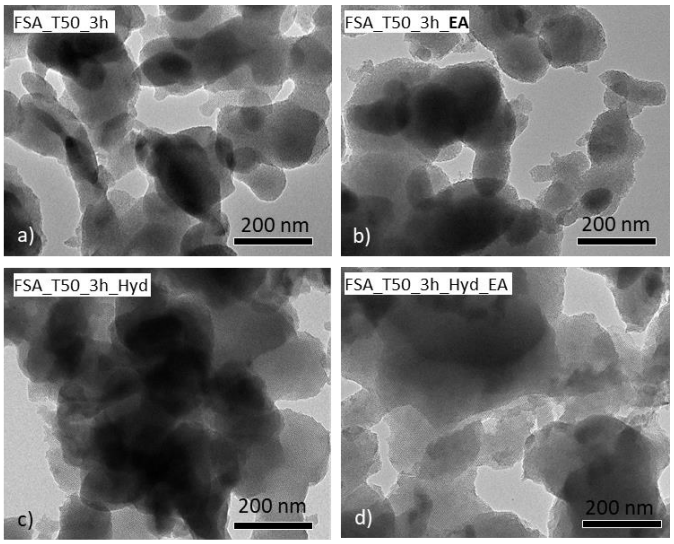


***Figure 6.11*** *TEM micrographs of the samples a) FSA_T50_3h, b) FSA_T50_3h_EA, c) FSA_T50_3h_Hyd, and d) FSA_T50_3h_EA_Hyd.*

The hydrothermal treatment also influences the morphology of the particles, in terms of size and shape: the FSA_T50_3h_EA_Hyd sample shows particles with irregular shapes and large dimensions in the 300-400 nm range (figure 6.11 c-d). This batch of experiments reveals the efficiency of hydrothermal treatment in improving the order of pores of both TEOS- and FSA-derived materials.

## 6.7 Effect of Acetyl Acetate

In all the syntheses proposed so far, ethyl acetate (EA) was employed. The effect of ethyl acetate as growth-inhibiting agent is known in the literature in the case of TEOS-derived silica, which is mainly due to the decrease in pH upon its hydrolysis, leading to the formation of acetic acid.[11] However, the effect of EA on FSA-derived silica synthesis is expected to be different due to its acidic nature, but it has never been an object of study. For this reason, two experiments were carried out to verify the possible changes in the textural and morphological properties of FSA-derived silicas in the absence of EA, with (FSA_T50_3h_Hyd) and without (FSA_T50_3h) a hydrothermal treatment. The two resulting samples were compared with FSA_T50_3h_EA_Hyd and FSA_T50_3h_EA. As expected, ethyl acetate does not cause any remarkable effect on silica, as confirmed by **SA-XRD** patterns, **$N_2$-physisorption** isotherms (let alone the effects of hydrothermal treatment), and pore size distribution in both the hydrothermally treated and untreated samples (table 6.7). **TEM** images ultimately confirm these findings, showing irregularly shaped particles in both the samples, with dimensions in the range of 300-400 nm (figures 6.11b and 6.11d for the samples FSA_T50_3h and FSA_T50_3h_Hyd, respectively).

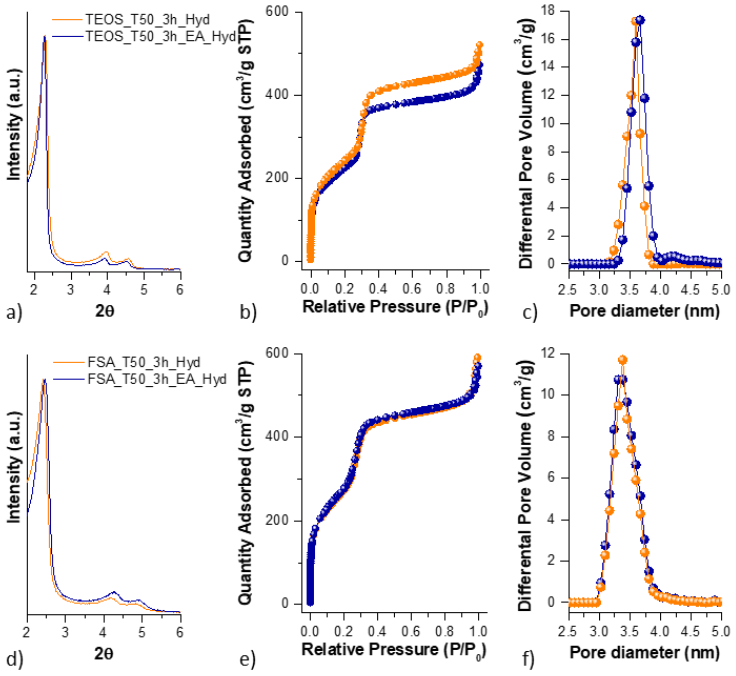


***Figure 6.12*** *(a, d) SA-XRD patterns, (b, e) $N_2$-physisorption isotherms, and (c, f) DFT-calculated pore size distributions of MCM-41 synthesized from FSA with and without ethyl acetate (EA) and with ancillary hydrothermal treatment. SA-XRD patterns have been normalized for clarity's sake.*

***Table 6.7*** *Surface area ($S_{BET}$), pore volume ($V_p$), DFT-calculated pore diameter, wall thickness ($w_t$), lattice spacing ($d_{100}$), hexagonal unit cell parameter ($a_0$), of the samples synthesized with and without ethyl acetate with hydrothermal treatment.*

| TEOS | T (°C) | t (h) | EA | $S_{BET}$ ($m^2\ g^{-1}$) | $V_p$ ($cm^3\ g^{-1}$) | $D_{P(DFT)}$ (nm) | $w_t$ (nm) | $d_{100}$ (nm) | $a_0$ (nm) |
|---|---|---|---|---|---|---|---|---|---|
| **TEOS_T50_3h_EA_Hyd*** | 50 | 3 | X | 966 | 0.8 | 4.0 | 0.9 | 4.2 | 4.9 |
| **TEOS_T50_3h_Hyd** | 50 | 3 | | 1083 | 0.8 | 3.7 | 0.8 | 3.8 | 4.4 |
| **FSA** | **T (°C)** | **t (h)** | **EA** | **$S_{BET}$ ($m^2\ g^{-1}$)** | **$V_p$ ($cm^3\ g^{-1}$)** | **$D_{P(DFT)}$ (nm)** | **$w_t$ (nm)** | **$d_{100}$ (nm)** | **$a_0$ (nm)** |
| **FSA_T50_3h_EA_Hyd*** | 50 | 3 | X | 817 | 0.6 | 3.6 | 0.9 | 3.9 | 4.5 |
| **FSA_T50_3h_Hyd** | 50 | 3 | | 886 | 0.7 | 3.6 | 0.8 | 3.8 | 4.4 |

** TEOS_T50_3h_EA_Hyd and FSA_T50_3h_EA_Hyd correspond to the samples already reported (see table 6.6), respectively. Relative standard deviation: %RSD($S_{BET}$)=2.1%; %RSD ($V_p$)=1.1%; %RSD ($D_p$)=1.8%. $d_{100}$ and $a_0$ were obtained from XRD data. For bimodal pore size distributions, two values of $D_{p(DFT)}$ are reported.*

In light of these results, it is possible to affirm that, the great differences in terms of chemical nature of the two precursors and the reactions involved, affect solely the morphologies of the silica particles while surface area, pore diameter, and pore size distributions, and porous order remained similar.

## 6.8 $^{29}$Si MAS Solid-State NMR Spectroscopy: Study of the Structural Properties

$^{29}$Si MAS Solid-State NMR spectroscopy was used to assess possible differences in terms of structural properties between the two samples TEOS_T50_3h_Hyd FSA_T50_3h_Hyd, *i.e.* different coordination of Si atoms, in terms of relative abundance of $Q_2$, $Q_3$, and $Q_4$ species (figure 6.13) between the FSA-derived sample (here relabelled NMR_MCM41_FSA) and its TEOS-derived counterpart (here NMR_MCM41_TEOS).

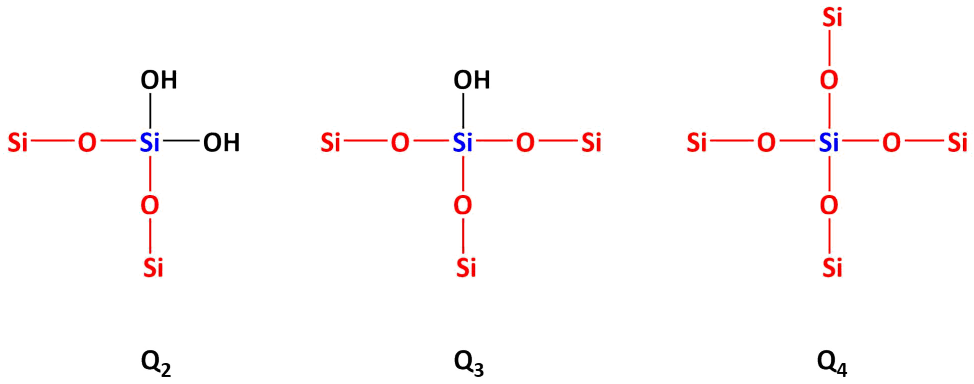


***Figure 6.13*** *Explanation of the $Q_n$ notation used in $^{29}$Si MAS Solid-State NMR Spectroscopy.*

The spectra are shown in figure 6.14. Both the spectra show three partially overlapping resonances centred at -90.7, -99.2, and -108.2 ppm ascribable to $Q_2$, $Q_3$, and $Q_4$ sites species , respectively.[12] The deconvolution with Gaussian components allowed to determine the relative abundance of the three different silicon coordination states exhibited by the samples. The results highlight the structural similarity between the two samples, justified by the great similarity in surface area and pore size distribution (table 6.8). Moreover, these values are also comparable to those reported in the literature for silicas treated at a similar temperature, including microporous, mesoporous, and mesostructured $SiO_2$.[13]

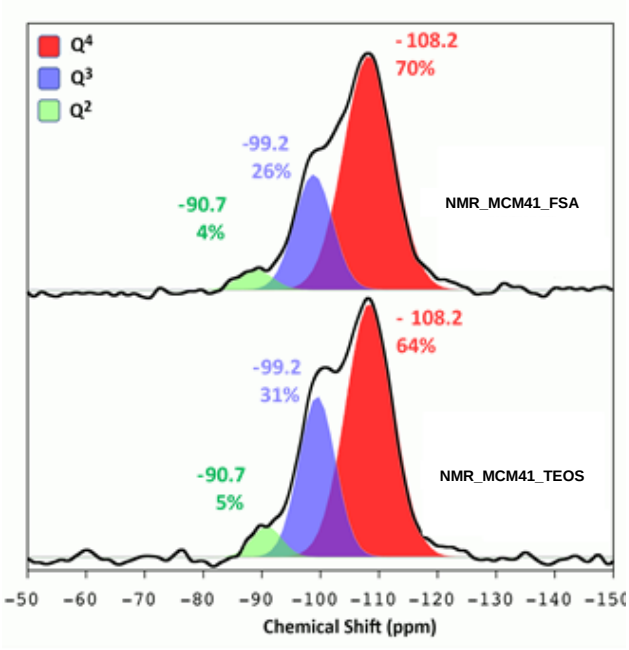


***Figure 6.14*** *$^{29}Si$ MAS Solid State NMR spectra relative to NMR_MCM41_TEOS and NMR_MCM41_FSA from TEOS and from FSA with the chemical shift (ppm) and the peak relative area (%) of the three revealed resonances.*

***Table 6.8*** *Comparison of the textural properties and the $Q_n$ composition between the sample FSA_T50_3h_Hyd (here labelled NMR_MCM41_FSA) with a TEOS-derived sample taken as reference (referred to as NMR_MCM41_TEOS).*

| Sample | $S_{BET}$ ($m^2\ g^{-1}$) | $V_p$ ($cm^3\ g^{-1}$) | $D_{P(DFT)}$ (nm) | $w_t$ (nm) | $d_{100}$ (nm) | $a_0$ (nm) | $Q_2$ (%) | $Q_3$ (%) | $Q_4$ (%) |
|---|---|---|---|---|---|---|---|---|---|
| **NMR_MCM41_TEOS** | 1083 | 0.8 | 3.7 | 0.8 | 3.7 | 4.3 | 64 | 31 | 5 |
| **NMR_MCM41_FSA** | 886 | 0.7 | 3.6 | 0.8 | 3.8 | 4.4 | 70 | 26 | 4 |

*Relative standard deviation: %RSD($S_{BET}$)=2.1%; %RSD ($V_p$)=1.1%; %RSD ($D_p$)=1.8%. $d_{100}$ and $a_0$ were obtained from XRD data. For bimodal pore size distributions, two values of $D_{p(DFT)}$ are reported.*

## 6.9 Recovering the Templating Agent

Usually, calcination is the preferred procedure to eliminate the templating agent and liberate the mesostructure. Despite its straightforwardness, calcination precludes the recovery of the templating agent with the loss of a valuable reactant. In envisaging a low-cost industrial process of siliceous mesostructured materials, recovering the templating agent through non-destructive procedure is critical and, along with using an alternative silicon source such as FSA, may contribute to lower the high cost associated with the synthesis of such materials. Extraction with a Soxhlet apparatus may be a viable alternative to calcination with the advantage of being adaptable in an industrial setting. In this sense, examples of Soxhlet extraction have been reported in the literature.[14–16] A typical Soxhlet apparatus is made up of a round-bottom flask, to be filled with the extracting solvent of choice, the siphon system where the thimble containing the sample is laid in and a refrigerator to condense the solvent vapours. A heating mantle is used to bring the extracting solvent to the boiling point.

### 6.9.1 Experimental Details

Approximately two grams of the as-synthesized bare support labelled FSA_MCM41_AS was specially prepared to recover the templating agent by extraction. The extraction procedure was retrieved in the literature and adapted for the present work. A portion of 750 mg was placed into a cellulose extraction thimble and carefully laid into a Soxhlet apparatus. The 500 $cm^3$ round-bottom flask of the apparatus was then filled with 200 mL of absolute EtOH and heated at 110 °C for 48h. Regular sampling was performed to assess the progress of the extraction *via* **FT-IR** spectroscopy at 15, 30 minutes, and 1, 3, and 6 hours, and finally 48 hours starting from the first observed reflux. For **FT-IR** analysis, approximately 15 mg was drawn from the apparatus, briefly washed with 1.5 mL of double-distilled water at room temperature, sonicated for 15 s, and then analysed. After 48 hours the product was recovered, quickly washed at room temperature with double-distilled water, and dried overnight (FSA_MCM41_ExE). Successively, a portion underwent calcination at 550 °C for 4 hours (rate 2 °C $min^{-1}$) to assess the thermal stability of the mesostructure. The extracting solution was then evaporated to recover the templating agent.

Furthermore, as a reference, the remaining portion of the as-synthesized sample (FSA) (250 mg) underwent calcination at 550 °C for 4 hours with a heating rate of 2 °C $min^{-1}$ (FSA_MCM41). An exactly similar extraction was also carried out by using 200 mL distilled water as the extracting solvent and the related samples were labelled as FSA_MCM41_ExW. The four so-obtained samples were characterized by means of **FT-IR**, **$N_2$-physisorption** measurements, and thermogravimetric analysis.

### 6.9.2 Extraction Evolution and Characterization of the Ehanol- and Water-Extracted MCM-41 Materials

**FT-IR** analyses performed to assess the evolution of the extraction of CTAB from the as-synthesized FSA_MCM41 are reported in figure 6.15a and b. The figures also feature the infrared spectrum of CTAB as reference. Instead, figure 6.16 depicts the thermogravimetric curves of the two extracted samples along with the as-synthesized. CTAB thermogravimetric curve was included again as reference.

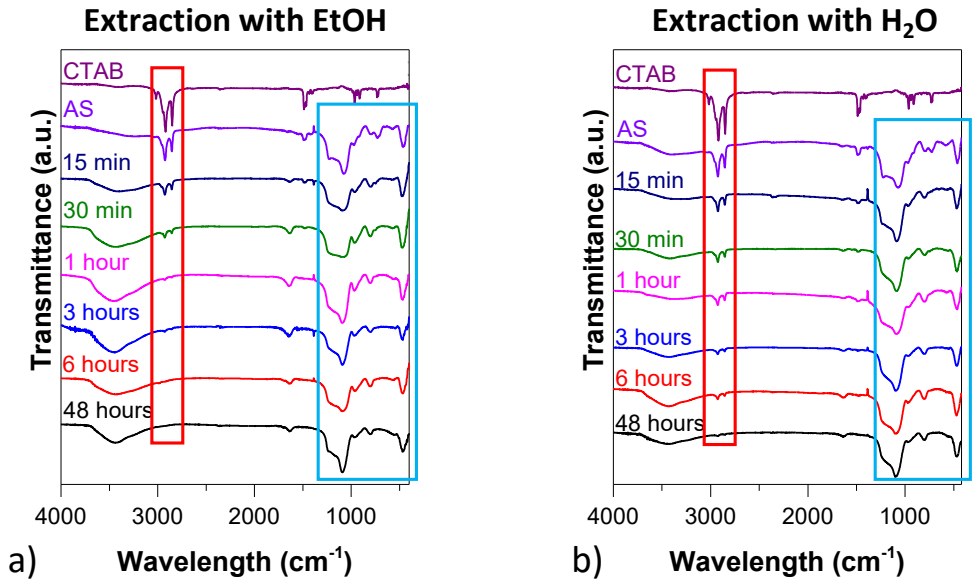


***Figure 6.15*** *Evolution of CTAB extraction with either a) ethanol or b) water assessed by collecting FT-IR spectra of the sample.*

As extraction time passes by, the signals associated with the presence of CTAB, in particular the symmetric and asymmetric stretching vibrations of C-H at 2847 and 2920 $cm^{-1}$, respectively, gradually wane, an indication of the

progressive extraction of the templating agent which results to be completed after one hour for ethanol but not completely finalized for water after 48 hours of extraction. All the samples, as expected, feature the typical vibration associated with $SiO_2$ in the range of wavelengths between (400-1600 $cm^{-1}$) without any significant variation (table 6.9.

***Table 6.9*** *Infrared bands found in a typical $SiO_2$ spectrum.*

| Mode | Group Involved | Frequencies ($cm^{-1}$) |
|---|---|---|
| Symmetric Stretching ( $\nu_s$) | Si-O-Si | 1240 |
| Asymmetric Stretching ($\nu_a$) | Si-O-Si | 1060 |
| Symmetric Stretching ($\nu_s$) | Si-OH | 960 |
| Asymmetric Stretching ($\nu_a$) | Si-O-Si | 800 |
| Bending ($\delta$) | O-Si-O | 460 |

The efficiency of the extraction with ethanol is confirmed by thermogravimetric analysis (figure 6.16.

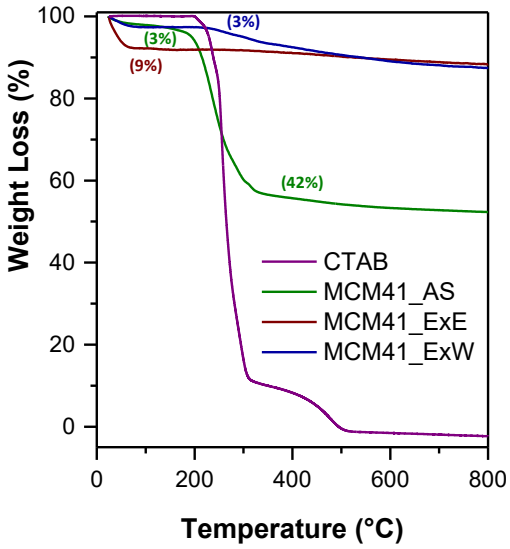


***Figure 6.16*** *Thermogravimetric analysis of the as-synthesized (FSA_MCM41_AS), extracted with ethanol (FSA_MCM41_ExE) and water (FSA_MCM41_ExW), and of the templating agent (CTAB) as reference.*

In fact, the sample FSA_MCM41_ExE shows the presence of a single step of weight loss (9 %), ascribable to adsorbed water. On the contrary, the sample FSA_MCM41_ExW, let alone the first weight loss of about 3 % related again to

adsorbed water, shows a second weight loss step of about 9 % due to CTAB still present after 48 hours of extraction. Taking into account that CTAB decomposition starts at about 250 °C and is completed at 500 °C, the FSA_MCM41_AS sample shows a first weight loss of about 3 % concluding at approximately 200 °C associated with the adsorbed water in the sample and a second weight loss of 42 %, which matches with the decomposition of CTAB. Upon evaporation of the extracting ethanolic solution, 316 mg of CTAB was obtained with a decrease of 42 % in weight from the initial 750 mg of the as-synthesized material (considering negligible the quantity taken out for the **FT-IR** analyses). This value is in good agreement with the loss in weight occurred upon thermogravimetric analysis. Another pivotal aspect to address is whether the mesostructure was preserved after performing the extraction. To do this, **$N_2$-physisorption** analyses were performed on the samples extracted after 48 hours both in ethanol (FSA_MCM41_ExE) and water (FSA_MCM41_ExW), and compared with the as-synthesized sample calcined at 550 °C to remove the template (FSA_MCM41). The textural proprieties of these samples were reported in table 6.10. The sample FSA_MCM41_ExE preserved its mesostructure, as confirmed by the isotherm (figure 6.17a) and the pore size distribution (figure 6.17b), that results almost superimposable with the sample FSA_MCM41.

***Table 6.10*** *Activation temperature, surface area, pore volume, pore width, wall thickness, $d_{100}$, and $a_0$ of the samples involved in the extraction with solvent of CTAB. Activation of the sample FSA_MCM41_ExE and FSA_MCM41_ExW was performed at 110 °C, the same temperature at which the extraction had been performed.*

| Sample | Treatment | Activation (°C) | $S_{BET}$ ($m^2$ $g^{-1}$) | $V_p$ ($cm^3$ $g^{-1}$) | $D_{P(DFT)}$ (nm) | $w_t$ (nm) | $d_{100}$ (nm) | $a_0$ (nm) |
|---|---|---|---|---|---|---|---|---|
| **FSA_MCM41** | Calcined at 550 °C | 250 °C 12 h | 873 | 0.7 | 3.67 | 0.96 | 3.92 | 4.53 |
| **FSA_MCM41_ExE** | Extracted with EtOH | 110 °C 12 h | 850 | 0.7 | 3.67 | 1.07 | 4.11 | 4.74 |
| **FSA_MCM41_ExE_C** | Extracted with EtOH and calcined at 550 °C | 250 °C 12 h | 356 | 0.4 | - | - | - | - |
| **FSA_MCM41_ExW** | Extracted with $H_2O$ | 110 °C 12 h | 247 | 0.7 | - | - | - | - |

*Relative standard deviation: %RSD($S_{BET}$)=2.1%; %RSD ($V_p$)=1.1%; %RSD ($D_p$)=1.8%. $d_{100}$ and $a_0$ were obtained from XRD data. For bimodal pore size distributions, two values of $D_{p(DFT)}$ are reported.*

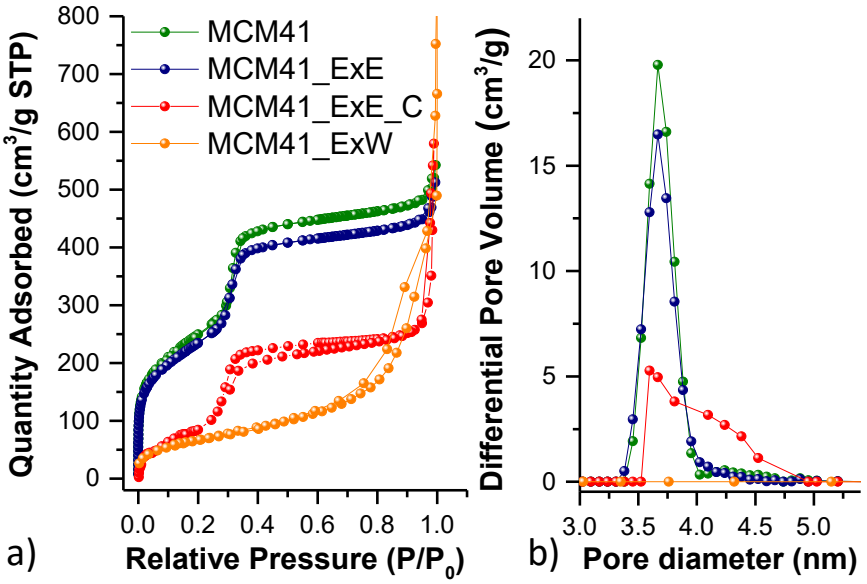


***Figure 6.17*** *a) $N_2$-physisorption isotherms and b) DFT-calculated pore size distribution of the samples FSA_MCM41, FSA_MCM41_ExE, FSA_MCM41_ExE_C,*

To verify the thermal stability of the mesostructure, FSA_MCM41_ExE was further treated at 550 °C (FSA_MCM41_ExE_C) for two hours, but a partial collapse of the porous structure occurred. Both the isotherm and the pore size distribution of the sample FSA_MCM41_ExW reveal the complete loss of the mesostructure centred a 2-3 nm. Moreover, no capillary condensation is observed in the range 0.1-0.3 $P/P_0$), which is typical for MCM-41 materials. Instead, capillary condensation phenomenon is observed at $\sim 0.7$ $P/P_0$, not relatable to a mesostructured material. This finding proves that water is not a suitable solvent for the complete removal of the template and the preservation of the mesostructure, probably because of possible reactions of silanol groups on the silica surface and water at the temperature at which the extraction was performed.

The results of **$N_2$-physisorption** were confirmed by **TEM** analysis: the sample FSA_MCM41_ExE retained its morphology in terms of size and shape of the particles as well as the porous order, (figure 6.18a-b) while the sample FSA_MCM41_ExW shows a worm-like mesoporous structure with pores in the 10-30 nm range size (Figure 6.18c-d).

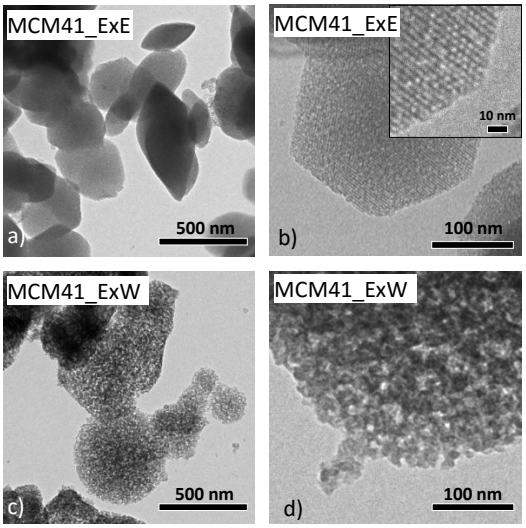


***Figure 6.18*** *TEM images at different magnification of the samples FSA_MCM41_ExE (a and b) and FSA_MCM41_ExW (c and d).*

In conclusion, ethanol should be preferred over water to carry out the recovery of the templating agent, making it possible to obtain a mesostructured material with similar textural properties when compared to the material obtained by conventional calcination. Moreover, complete extraction is achieved in less time with ethanol (approximately six hours) rather than the 48 hours required by using water.

## 6.10 Reusing the Supernatant as the Reaction Medium.

Following the synthesis route described in table 6.1, almost 60 % of the CTAB used as the templating agent will not take part into the set up of the micellar scaffold involved in mesostructure formation and remains in the supernatant solution upon centrifugation. If a proper recovery strategy were not be implemented, it would entail the waste of a valuable reactant that may be reusable for further synthesis cycles, resulting in an unacceptable shortcoming in the design of a zero-waste industrial process.

In this context, Lai *et al.* published an article concerning the reuse of the supernatant solution rich in CTAB for further soft-templating syntheses.[17] In their work, they studied the quality of calcined MCM-41 materials derived from

successive syntheses by using TEOS as the precursor. Five consecutive syntheses cycles were performed with a predictable progressive decrease in both the amount of final product and surface area values (from 1170; 916; 728; and 508 $m^2$ $g^{-1}$).[17] In regard to our system, the most straightforward approach would be the direct addition of the Soxhlet-recovered CTAB into the pH-adjusted supernatant. In fact, the supernatant derived from the synthesis features a pH values ranging from 9 to 10 and is made of a dispersion in water of different components, including CTAB (60 % of the total amount added during the synthesis), $NH_4F$, and $NH_3$ in solution along with small $SiO_2$ particles in suspension. After a few days, these silica particles start to sediment, whose removal is possible by high-speed centrifugation ($>$ 4500 rpm). Upon separation, the supernatant could be used again as the new basic reacting medium soon after the addition of $NH_3$ to reach a pH value of $\sim$ 13.5, typical of freshly prepared reacting mixture. This strategy should, theoretically, lead to the manufacture of MCM-41 materials with reproducible values of surface area. Figure 6.19 depicts the aforementioned procedure.

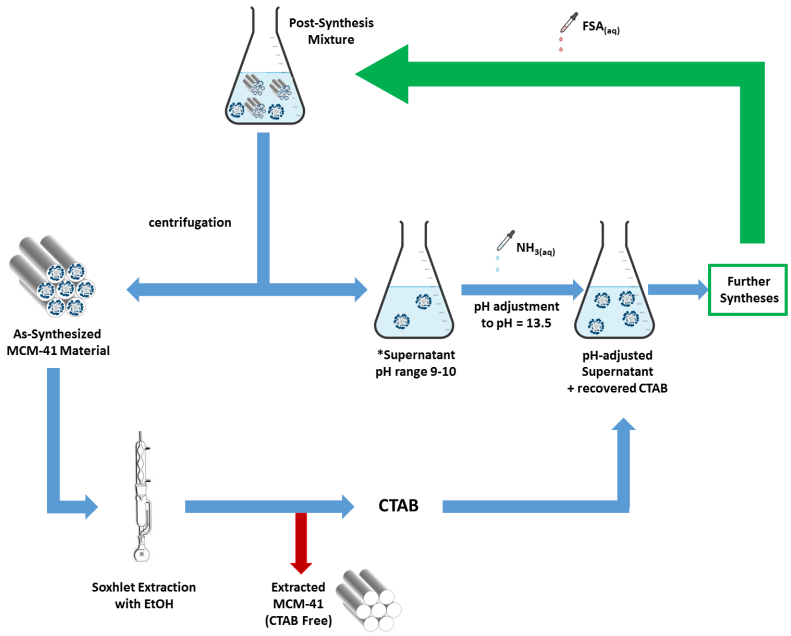


***Figure 6.19*** *Possible pathway to recover and reuse CTAB. * Supernatant may contain $SiO_2$ in suspension along with $NH_4F$ in solution. As this may affect the properties of the final product, performing the sedimentation and separation of $SiO_2$ a and the recovery of $NH_4F$ would be advisable (refer to the text).*

However, syntheses performed by utilizing the supernatant without any further treatment, besides pH adjustment, ought to be designed in order to

verify how particle nucleation and growth are affected by $SiO_2$ present in solution, still not having been completely removed by centrifugation. Another crucial aspect of this synthesis to be assessed is the presence of $NH_4F$ and its possible effect on MCM-41 synthesis and final features. Concerning the possible recover of $NH_4F$ itself, it might be done by means of fractional crystallization from water of the supernatant exploiting the different solubility that CTAB and $NH_4F$ exhibit (1.3 g/100 mL for CTAB and 37.1 g/100 mL for $NH_4F$, both at 20°C). A neater alternative approach would involve the precipitation of fluoride in the form of $CaF_2$, as suggested in the patent by Pala *et al.*,[18] with the associated advantage of obtaining a valuable commodity.

*Unfortunately, these further experiments, planned for March-April 2020, were not carried out as a consequence of the contingency related to the pandemic crisis.*

## 6.11 Conclusions

This chapter dealt with the topic of the feasibility of utilizing FSA to synthesize MCM-41. It was proven that FSA is actually capable of being successfully utilized as a precursor in soft-templating synthesis of MCM-41 replacing the most common precursor nowadays used, such as TEOS and TMOS. This was assessed by carried out by a careful comparison between TEOS and FSA and by varying experimental conditions. Temperature was investigated in the range from 30° to 70° C where an enhancement in textural properties was observed when carrying out the reaction at 50 °C was observed regardless of the precursor used while reaction time (three, six, and eighteen hours) affected very modestly the properties of the samples. Hydrothermal treatment brought about a slight increase in pore dimension when using either TEOS or FSA, but wall thickness remained unaffected when using FSA. Lastly, no significant variations were observed when ethyl acetate was not added in the reaction mixture. A variety of analytical techniques were used to investigate the materials obtained, it was observed that, in spite of consistent differences in morphology, the textural properties in terms of specific surface area, pore volume, and wall thickness were surprisingly similar, pointing out the actual feasibility of replacing TEOS with FSA for high-quality MCM-41 material. This chapter also put forward a successful recovery strategy of CTAB *via* solvent extraction with a Soxhlet

apparatus, by using either ethanol or water. The former was the preferred solvent, given the better textural properties exhibited by the extracted material. This strategy was proposed not only to recover a valuable reactant but also to further lower the cost associated with the synthesis of mesostructured materials. Coupling the utilization a low-cost precursor, such as FSA, with the recover of CTAB and $NH_4F$ might represent the first step in setting up an economically and environmentally sustainable zero-waste industrial process to manufacture MCM-41 materials. Moreover, as reported in the following chapter, their derived nanocomposites, bearing suitable active phases, may find application in important industrial processes, such as $H_2S$ removal from sour syngas.

# References

[1] Yu, H. S.; Rhee, K.-I.; Lee, C. K.; Yang, D.-H. Two-Step Ammoniation of By-Product Fluosilicic Acid to Produce High Quality Amorphous Silica. *Korean Journal of Chemical Engineering* **2000**, *17*, 401–408, ISSN: 1975-7220, DOI: https://doi.org/10.1007/BF02706850.

[2] Liu, T.; Jin, F.; Wang, X.; Fan, Y.; Yuan, M. Synthesis of Titanium Containing MCM-41 from Industrial Hexafluorosilicic Acid as Epoxidation Catalyst. *Catalysis Today* **2017**, *297*, Catalytic science and technology in Sustainable Environment II (EECAT 2016), 316–323, ISSN: 0920-5861, DOI: https://doi.org/10.1016/j.cattod.2017.03.011.

[3] Elineema, G.; Kim, J. K.; Hilonga, A.; Shao, G. N.; Kim, Y.-N.; Quang, D. V.; Sarawade, P. B.; Kim, H. T. Quantitative Recovery of High Purity Nanoporous Silica from Waste Products of the Phosphate Fertilizer Industry. *Journal of Industrial and Engineering Chemistry* **2013**, *19*, 63–67, ISSN: 1226-086X, DOI: https://doi.org/10.1016/j.jiec.2012.07.001.

[4] Sarawade, P.; Kim, J.; Hilonga, A.; Kim, H. T. Recovery of High Surface Area Mesoporous Silica from Waste Hexafluorosilicic Acid ($H_2SiF_6$) of Fertilizer Industry. *Journal of Hazardous Materials* **2009**, *173*, 576–580, DOI: https://doi.org/10.1016/j.jhazmat.2009.08.125.

[5] Zhao, D.; Wan, Y.; Zhou, W., *Ordered Mesoporous Materials*; Wiley: 2013, ISBN: 9783527326358.

[6] Cara, C. Siliceous and non-siliceous Mesostructured Iron Oxide Nanocomposites for $H_2S$ Removal from Syngas., PhD Thesis, University of Cagliari, 2017.

[7] Mureddu, M. Mesostructured Metal Oxide-Based Nanocomposites as Sorbents for $H_2S$ Removal from Syngas Coal Gasification., PhD Thesis, University of Cagliari, 2014.

[8] Meléndez-Ortiz, H.; García-Cerda, L.; Olivares-Maldonado, Y.; Castruita, G.; Mercado-Silva, J.; Perera-Mercado, Y. Preparation of Spherical MCM-41 Molecular Sieve at Room Temperature: Influence of the Synthesis Conditions in the Structural Properties. *Ceramics*

*International* **2012**, *38*, 6353–6358, ISSN: 0272-8842, DOI: https://doi.org/10.1016/j.ceramint.2012.05.007.

[9] Fulvio, P. F.; Pikus, S.; Jaroniec, M. Tailoring Properties of SBA-15 Materials by Controlling Conditions of Hydrothermal Synthesis. *J. Mater. Chem.* **2005**, *15*, 5049–5053, DOI: 10.1039/B511346F.

[10] Cara, C.; Rombi, E.; Mameli, V.; Ardu, A.; Sanna Angotzi, M.; Niznansky, D.; Musinu, A.; Cannas, C. $\gamma$-$Fe_2O_3$-M41S Sorbents for $H_2S$ Removal: Effect of Different Porous Structures and Silica Wall Thickness. *The Journal of Physical Chemistry C* **2018**, *122*, 12231–12242, DOI: 10.1021/acs.jpcc.8b01487.

[11] Suteewong, T.; Sai, H.; Lee, J.; Bradbury, M.; Hyeon, T.; Gruner, S. M.; Wiesner, U. Ordered Mesoporous Silica Nanoparticles with and without Embedded Iron Oxide Nanoparticles: Structure Evolution during Synthesis. *J. Mater. Chem.* **2010**, *20*, 7807–7814, DOI: 10.1039/C0JM01002B.

[12] Lippmaa, E.; Maegi, M.; Samoson, A.; Engelhardt, G.; Grimmer, A. R. Structural Studies of Silicates by Solid-State High-Resolution Silicon-29 NMR. *Journal of the American Chemical Society* **1980**, *102*, 4889–4893, DOI: 10.1021/ja00535a008.

[13] Steel, A.; Carr, S. W.; Anderson, M. W. 29Si solid-state NMR study of mesoporous M41S materials. *Chemistry of Materials* **1995**, *7*, 1829–1832, DOI: 10.1021/cm00058a012.

[14] Lai, J. Y. Enhanced Surfactant Template Recycling for Continuous Production of Mesoporous Silica Materials., PhD Thesis, Swinburne University of Technology Sarawak Campus, 2017.

[15] Thielemann, J. P.; Girgsdies, F.; Schlögl, R.; Hess, C. Pore Structure and Surface Area of Silica SBA-15: Influence of Washing and Scale-Up. *Beilstein journal of nanotechnology* **2011**, *2*, 110–118.

[16] Lai, J. Y.; Ngu, L. H.; Twaiq, F. Template Recycling and Reuse in Mobil Crystalline Material 41 Synthesis: Statistical Study. *Journal of Applied Science & Process Engineering* **2018**, *5*, 213–226.

[17] Lai, J.; Twaiq, F.; Ngu, L. Recycling of Surfactant Template in mesoporous MCM-41 Synthesis. *IOP Conference Series: Materials Science and Engineering* **2017**, *206*, 012044, DOI: 10.1088/1757-899X/206/1/012044.

[18] Pala, L. and Lavanga, M. High Purity Synthetic Fluorite, Process for Preparing the Same and Apparatus Therefor., WO 2016/156969 A1.

# 7

# Designing Sorbents for Midtemperature $H_2S$ Removal from Sour Syngas

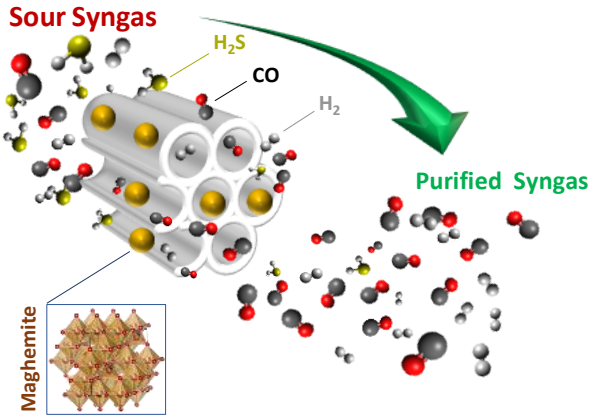


*Coupling ultrasmall active nanoparticles (< 3 nm) with mesostructured inorganic supports has been proven to be extremely effective in the design of highly active and regenerable materials, even in severe conditions, serving as $H_2S$ removal sorbents in the sweetening process of sour syngas. The siliceous mesostructure acts as a scaffold onto which it is possible to disperse homogeneously the active phase in the form of highly reactive ultrasmall nanoparticles. Its regular porosity and apt pore size make the active phase easily accessible whilst the mesochannels' walls prevent sintering phenomena from occurring, allowing the regeneration of the material. Depending on the nature of the active phase, it is possible to produce ultrasmall nanophases for a wide range of applications, including sorption and catalysis. Hereinafter, the FSA-derived sorbents, bearing either*

*$\gamma$-$Fe_2O_3$ or $ZnFe_2O_4$ as the active phase, were synthesized and the $\gamma$-$Fe_2O_3$-bearing samples were tested as $H_2S$ removers from syngas at mid-temperature, exhibiting high reactivity and regenerability. Their performances were also compared with those of Katalco 32-5, a commercial unsupported sorbent. Furthermore, the low regeneration temperature (about 300 °C), besides the high removal capacity, renders FSA-derived MCM41-based systems an low-cost alternative class of regenerable sorbents in thermally efficient cleaning up processes in Integrated Gasification Combined Cycles (IGCC) systems.*

## 7.1 Introduction

The design of highly efficient, stable, regenerable, and low-cost catalysts/sorbents for heterogeneous catalytic and adsorption processes governed by gas-solid or liquid-solid reactions has been one of the main focus of the scientific research. Metal oxides appear to be the most suitable candidates in term of price and stability. However, their efficiency gradually decline under harsh reaction conditions because of their unreacted core and sintering phenomena over repeated cycles of use. In this context, different types of metal oxides have been proposed as potential sorbents in a wide range of temperatures based on thermodynamic calculations.[1] Among them, ZnO has a high equilibrium constant for sulfidation leading to low $H_2S$ concentrations but with slow kinetics, which limits its sulfur loading capacity.[1–3] Iron oxide, on the other hand, features fast kinetics and a high sulfur loading capacity, but its equilibrium constant is lower than the one found for zinc oxide.[2,4,5] Solid sorbents made up of unsupported zinc or iron oxides, also in form of nanostructured materials, have been proposed in some pilot plants;[6] however sintering in these materials, which occurs during the successive mid-temperature or high-temperature cycles, leads to a dramatic decrease in their performances. Over the last decade, as a result of the potential benefit in terms of general thermal efficiency of the IGCC (Integrated Gasification Combined Cycles) plant, stemming from the use of mid-temperatures for sulfidation and regeneration cleaning plant, the research has been moving towards the development of supported active phases.[7,8] In this framework, one of the most attractive solution

consists in dispersing the metal oxide in a mesostructured matrix featuring pores smaller than 10 nm, which prevent sintering phenomena, in order to improve the accessibility towards the active phase, and to limit the growth of the metal oxide, thus forming highly reactive ultrasmall nanoparticles ($<$ 3 nm) by the intrinsic physical limitations placed by the mesochannels. The increase in the surface/volume ratio of the nanostructured active phase improves the extent of gas-solid and liquid-solid contacts, favouring heterogeneous reactions. However, characterization of such supported ultrasmall particles and the study of their modifications during the processes is not trivial, leading to a lack in the comprehension of the properties-performances correlations.[2,9] Nevertheless, some metal oxides exhibit specific physical properties that may be exploited for their characterization with highly sensitive techniques in respect to their local structure. For instance, iron oxides can be studied by $^{57}$Fe-Mössbauer spectroscopy and, because of their magnetic behaviour, by magnetometry,[10,11] even on complex materials, as demonstrated in the case of natural composites and mesostructured amorphous silica-based materials. Herein, in light of the promising $H_2S$ removal performance that had already been proved in the case of iron-based silica composite under a $H_2S$/He mixture at mid-temperature, highly active and regenerable sorbents composed of an ultrasmall iron-based phase and a mesostructured support are proposed as $H_2S$ removers for sour syngas.[12] Taking into account the harsh conditions of the sour syngas (reducing atmosphere), to which the active phase was exposed, and the gas-solid chemical reactions involved in the repeated sulfidation and regeneration processes, the characterization of the active phase was carried out by combining of $^{57}$Fe Mössbauer spectroscopy and magnetometry.

## 7.2 Experimental

A brief description of the main impregnation methods to obtain nanocomposites was given earlier on this thesis (section 4.3.3) and the so-called two-solvent impregnation technique was preferred over the others in virtue of its advantages over the other viable alternatives. Experimentally, a total of four sorbents were synthesized, by using either TEOS or FSA as the siliceous precursor to build the sorbent scaffold. They were then impregnated to obtain the corresponding nanocomposites bearing a given active phase, be either

γ-$Fe_2O_3$ or $ZnFe_2O_4$. Active phase loading was set at 10 % w/w, as previous works highlighted that such a loading ought to be regarded as a reasonable compromise between suitable dispersing capacity by the mesostructured material and obtaining a sorbent bearing insufficient amount of active phase. Table 7.1 recapitulates the synthesis conditions of the samples designated to be impregnated (TEOS_T50_3h_Hyd and FSA_T50_3h_Hyd.)

***Table 7.1*** *Experimental conditions for the synthesis of MCM-41 from either TEOS or FSA as a support for syngas sweetening sorbents.*

| | |
|---|---|
| **Temperature** | 50 °C |
| **Reaction Time** | 3 h |
| **Hydrothermal Treatment** | **YES** |
| **Acetyl Acetate** | **NO** |

Drying the bare support is the preliminary step involved in the two-solvent impregnation technique, with the samples being placed in an oven at 120 °C for 48 hours. Once dried and allowed to cool to room temperature in a desiccator, they were dispersed in hexane and the resulting mixtures was stirred for two hours at room temperature. Then, a suitable amount of an aqueous solution containing either $Fe(NO_3)_3 \cdot 9H_2O$ or a 2:1 mixture of $Fe(NO_3)_3 \cdot 9H_2O$ and $Zn(NO_3)_2 \cdot 6H_2O$ was slowly added dropwise into the silica dispersion in hexane in order to obtain γ-$Fe_2O_3$ or $ZnFe_2O_4$ as the dispersed active phase, respectively. The added amount of precursor was calculated by taking into account pore volume and the desired load. After two hours of uninterrupted strirring, the mixtures were heated to 80 °C until complete evaporation and then replaced in an oven at 80 °C overnight to finalize drying. Finally, the so-obtained solids were heated in a muffle furnace at 500 °C for two hours with a heating rate of 2 °C $min^{-1}$ to decompose the nitrate precursors into oxides (figure 7.1). Experimental data concerning the synthesis the four sample synthesized are reported in Table 7.2.

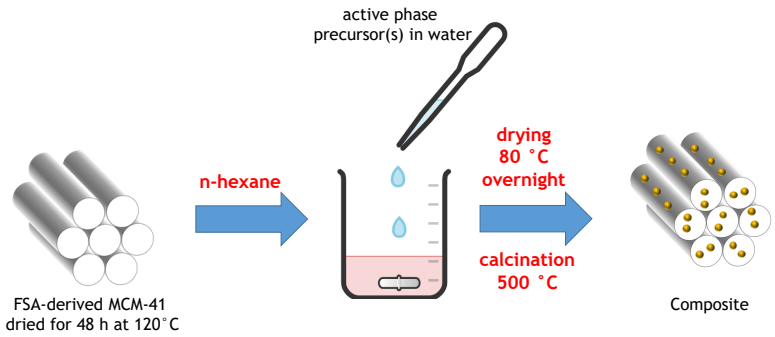


***Figure 7.1*** *Schematic representation of the two-solvent impregnation technique performed to obtain $\gamma$-$Fe_2O_3$ and $ZnFe_2O_4$-bearing nanocomposites with a 10 % loading of active phase.*

***Table 7.2*** *Experimental conditions adopted for the two-solvent impregnation technique to prepare the four nanocomposites.*

| Sample | Support Weight (mg) | Support Pore Volume ($cm^3\ g^{-1}$) | Volume of Aqueous Solution To Add (µL) | Load (w/w) (%) |
|---|---|---|---|---|
| **10Fe_TEOS_MCM41** | 250 | 0.69 | 172 | 9.7 |
| **10Fe_FSA_MCM41** | 250 | 0.73 | 203 | 10.2 |
| **10ZnFe_TEOS_MCM41** | 250 | 0.69 | 172 | 10.3 |
| **10ZnFe_FSA_MCM41** | 250 | 0.73 | 203 | 10.2 |

## 7.3 Characterization

A thorough characterization of the four composites was then carried out which includes small- and wide-angle X-ray diffraction, **$N_2$-physisorption** measurements, Mössbauer spectroscopy, magnetic measurements, and **TEM** imaging. Small angle X-ray diffraction patterns, depicted in figure 7.2, confirm that the mesostructure in the four composites was preserved upon impregnation whereas wide angle diffraction patterns highlight that the active phases are uniformly dispersed in the form of ultrasmall nanoparticles.

SA-XRD patterns of the four nanocomposites are almost completely superimposable with their related bare samples showing the reflexes ((100), (110), and (200)) typical of a long-range hexagonal order of the mesopores centred at the same values of 2θ. On the **Wide-Angle XRD** patterns (figure 7.2b), along with the typical reflex centred at 22° ascribable to the halo of amorphous silica, two weak broad reflexes at 35° and 63° reveal the formation of a highly dispersed iron-containing phase. **$N_2$-physisorption** measurements and pore size distribution show that all the nanocomposites feature the typical IVb

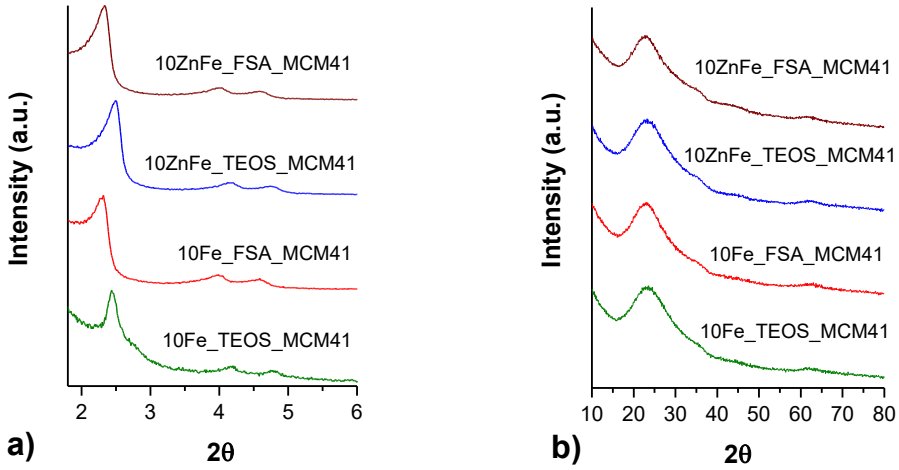


***Figure 7.2*** *a) SA- and b) WA-XRD patterns of the four nanocomposites synthesized from TEOS or FSA bearing either $\gamma$-$Fe_2O_3$ or $ZnFe_2O_4$.*

isotherm for a mesoporous material. The typical phenomenon of capillary condensation occurring in the range between 0.2-0.3 $P/P_0$ and show an expected reduction in surface area values upon impregnation accompanied by a slight reduction of pore volume. Other parameters such as $d_{100}$, $a_0$, and $w_t$ result to be unaffected (figure 7.3 and table 7.3).

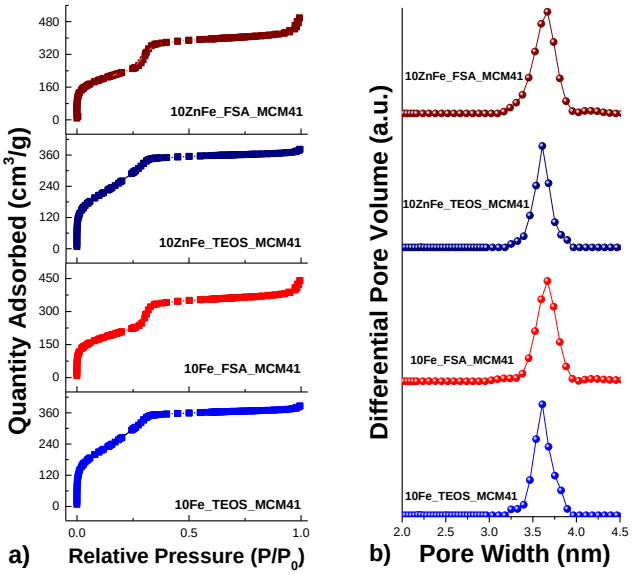


***Figure 7.3*** *a) $N_2$-physisoption isotherms and b) DFT-calculated pore size distribution of the four nanocompsites.*

***Table 7.3*** *Surface area ($S_{BET}$), pore volume ($V_p$)), DFT-determined pore diameter ($D_{P(DFT)}$), lattice spacing ($d_{100}$), hexagonal unit cell parameter ($a_0$), and wall thickness ($w_t$) of the two bare sorbents synthesized from TEOS and FSA, labelled with *, and the corresponding nanocomposites obtained by the two-solvent impregnation techniques from them.*

| Sample | $S_{BET}$ ($m^2$ $g^{-1}$) | $V_P$ ($cm^3$ $g^{-1}$) | $D_{p\ (DFT)}$ (nm) | $d_{100}$ (nm) | $a_0$ (nm) | $w_t$ (nm) |
|---|---|---|---|---|---|---|
| **TEOS_T50_3h_Hyd*** | 1083 | 0.7 | 3.7 | 3.8 | 4.4 | 0.7 |
| **10Fe_TEOS_MCM41** | 947 | 0.6 | 3.6 | 3.6 | 4.2 | 0.6 |
| **10ZnFe_TEOS_MCM41** | 924 | 0.6 | 3.6 | 3.6 | 4.2 | 0.7 |
| **FSA_T50_3h_Hyd*** | 886 | 0.7 | 3.6 | 3.8 | 4.4 | 0.8 |
| **10Fe_FSA_MCM41** | 754 | 0.6 | 3.7 | 3.8 | 4.4 | 0.7 |
| **10ZnFe_FSA_MCM41** | 837 | 0.6 | 3.7 | 3.8 | 4.4 | 0.7 |

*Relative standard deviation: %RSD($S_{BET}$)=2.1%; %RSD ($V_p$)=1.1%; %RSD ($D_p$)=1.8%. $d_{100}$ and $a_0$ were obtained from XRD data. For bimodal pore size distributions, two values of $D_{p(DFT)}$ are reported.*

To assess the nature of the iron-bearing phase, the combined use of RT $^{57}$Fe-Mössbauer spectroscopy on all the four nano, DC magnetometry, and HRTEM were performed on some composite. Fe Mössbauer spectroscopy has been proposed, being capable of distinguishing maghemite, from hematite and magnetite, even in nanostructured materials. The four nanocomposites were then analysed by means of room temperature **RT $^{57}$ Fe-Mössbauer spectroscopy** in order to assess the nature of Fe in the two active phases investigated. As can be seen in figure 7.4, all the four spectra show a doublet with an isomer shift of (0.34 ± 0.01) mm $s^{-1}$, typical of very small nanoparticles of either maghemite, as observed in previous works by the author's research group in the case of $\gamma$-$Fe_2O_3$,[12–14] or zinc ferrite, as reported by Kundu *et al.*.[15] The similar values are due to the presence of Fe III in isostructural phases (spinel structure).

The associated values of FWHM related to these peaks are: (0.48 ±0.01) mm $s^{-1}$ for 10Fe_TEOS_MCM41, (0.53 ± 0.01) mm $s^{-1}$ for 10Fe_FSA_MCM41, (0.52 ± 0.01) mm $s^{-1}$ for 10ZnFe_TEOS_MCM41, and (0.56 ± 0.01) mm $s^{-1}$ for 10ZnFe_FSA_MCM41 (table 7.4). The minimal differences observed may be related to the different particle size or different particle size distribution of the active phase embedded in the nanocomposites.

The presence of maghemite as the active phase is consistent with the magnetic behaviour observed for the sample 10Fe_FSA_MCM41 by magnetic field ($M$ *vs.* $H$) and temperature ($M$ *vs.* $T$) dependences of the magnetization. Indeed, the $M$

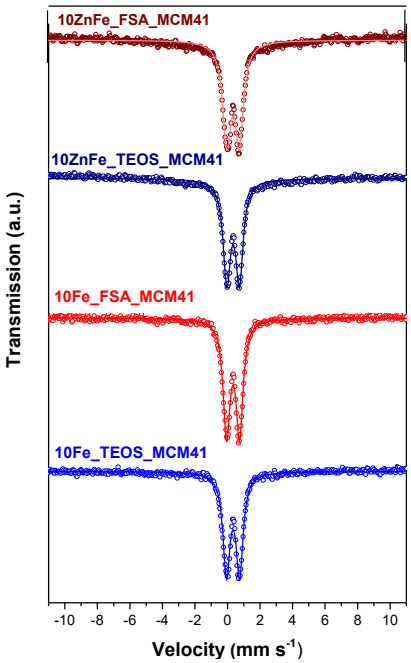


***Figure 7.4*** *RT $^{57}$Fe-Mössbauer spectra of the four nanocomposites.*

***Table 7.4*** *Isomer shift and FWHM values observed in the RT $^{57}$Fe-Mössbauer spectra of the four nanocomposites synthesized.*

| Sample | Isomer Shift (mm $s^{-1}$) | FWHM (mm $s^{-1}$) |
|---|---|---|
| **10Fe_TEOS_MCM41** | (0.34 ± 0.01) | (0.48 ± 0.01) |
| **10Fe_FSA_MCM41** | (0.34 ± 0.01) | (0.53 ± 0.01) |
| **10ZnFe_TEOS_MCM41** | (0.34 ± 0.01) | (0.52 ± 0.01) |
| **10ZnFe_FSA_MCM41** | (0.34 ± 0.01) | (0.56 ± 0.01) |

*vs. H* curves at 5K show the typical ferro/ferrimagnetic behaviour with a sigmoidal shape and a very small hysteresis loop ($H_c$ about 0.5 kOe) and a magnetization saturation of about 40 emu $g^{-1}$ of active phase (figure 7.5).

These features are ascribable to a ferrimagnetic phase and suggests the presence of maghemite nanoparticles. In fact, being the isomer shift of the doublet of the Mössbauer spectrum typical of Fe III, among the iron oxide phases, it is possible to exclude the presence of the ferrimagnetic magnetite and the presence of hematite, because of its antiferromagnetism. The low $M_s$ value could be justified by the presence of canted spins, as expected for ultrasmall particles.[13] The *M vs. T* curves show a typical superparamagnetic behaviour: the ZFC-FC curves appear overlapped at high temperature, up to about 18 K ($T_{irr}$), and in the ZFC curve exhibit a narrow peak with a maximum about 11 K ($T_{max}$). Assuming the presence

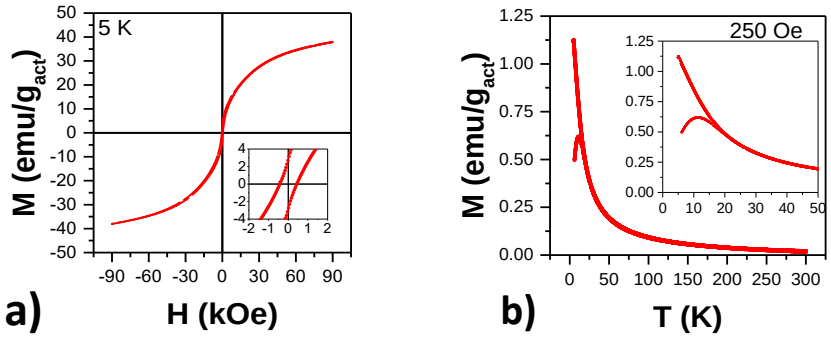


***Figure 7.5*** *Dependence of magnetization on a) magnetic field and on b) temperature of the sample 10Fe_FSA_MCM41.*

of negligible interparticle interactions, due to the low $Fe_2O_3$ loading, the $T_{max}$ value can be considered as directly related to the average volume of all the particles, while $T_{irr}$ is related to the volume of the biggest ones. Therefore, the ($T_{irr}$-$T_{max}$) values can provide a qualitative measure of the volume size distribution and for the sample 10Fe_FSA_MCM41 is an indication the narrow particle size distribution of its active phase. These results are in agreement with the presence of ultrasmall maghemite particles dispersed homogeneously all over the siliceous matrix and are similar those found for a homologous TEOS-derived sample.[13]

On the other hand, **HRTEM** imaging on the γ-$Fe_2O_3$-bearing nanocomposites (figures 7.6 and 7.7) confirmed the retention of the mesostructured order upon impregnation with the two-solvent technique. It is also possible to notice that the active phase is uniformly distributed all over the support and made up of well-crystallized spheroidal nanoparticles of about 2 nm having single inter-fringe distances of about 2 Å, ascribable to the plane (400) of maghemite (γ-$Fe_2O_3$, PDF card N. 00-039-1346, 2.09 Å, Intensity=19 %), in agreement with $^{57}$-Fe Mössbauer spectroscopy and DC magnetometry data ascribable to maghemite,[13] confirming both Mössbauer and magnetic measurements data.

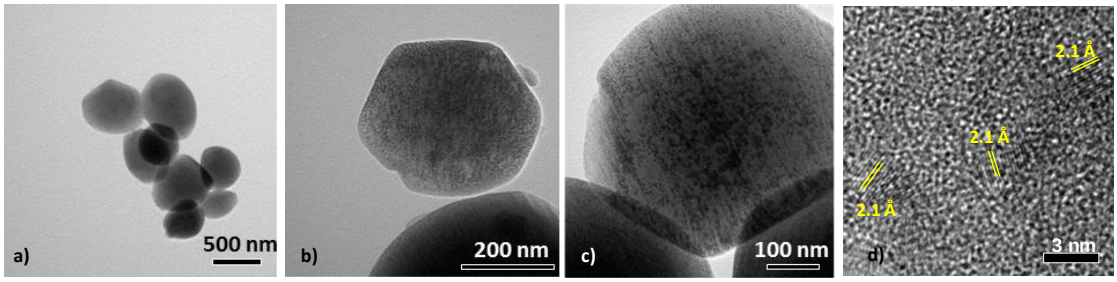


***Figure 7.6*** *HRTEM micrographs of the sample 10Fe_TEOS_MCM41 at different magnifications. Micrograph d) is reported with permission from Cara et al.*[16]

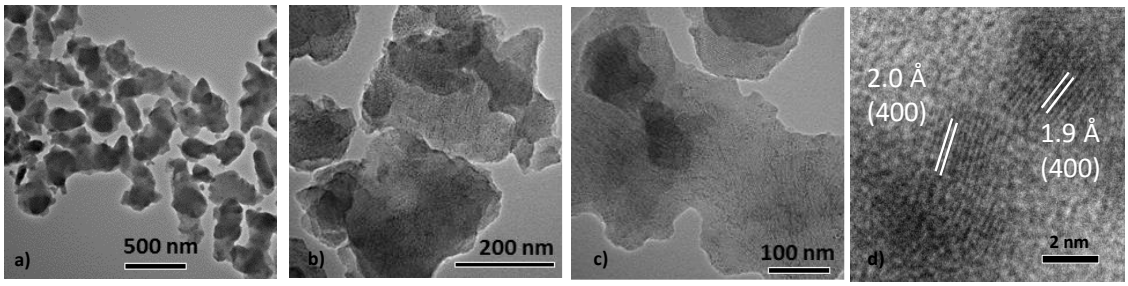


***Figure 7.7*** *HRTEM micrographs of the sample 10Fe_FSA_MCM41 at different magnifications.*

## 7.4 Thermal Stability of the Nanocomposites

The thermal stability in static air of the nanocomposites prepared from either TEOS or FSA was assessed by **WA-XRD** by means of a X-ray diffractometer equipped with a high temperature chamber (HTC). The investigated range of temperatures was 25-1300 °C, the pattern were acquired at every temperature, and an additional pattern was acquired after the heating process as soon as room temperature was reached again. Figure 7.8 depicts the collected patterns for each nanocomposite. All the patterns were collected in the range 10-45° and feature the typical silica halo centred at 22°, let alone the removed (111) Pt peak whose presence is due to the sample holder. Concerning the $\gamma$-$Fe_2O_3$-bearing nanocomposites (figures 7.8a and b), the two patterns show a progressive increase in intensity of the peak (311) centred at 35° starting in the range of temperature between 600-700 °C. From about 1200 °C, a further peak centred at 33° related to the most intense plane (104) of hematite is also visible in both these patterns, indicating the partial maghemite-hematite transition, being the latter the most thermodinamically stable phase. Similarly, the **WA-XRD** patterns of the $ZnFe_2O_4$-bearing nanocomposites (figures 7.8c and d) feature starting from 600-700 °C the emergence of three peaks related to the reflexes

(200), (311), and (400) ascribable to zinc ferrite where and gradual increase in intensity of the peaks is observed up to 1300 °C.

**Legend** ○: $\gamma$-$Fe_2O_3$, PDF Card No. 089-5894;
△: $ZnFe_2O_4$, PDF Card No. 082-1049;
□: Hematite, PDF Card No. 033-0664.

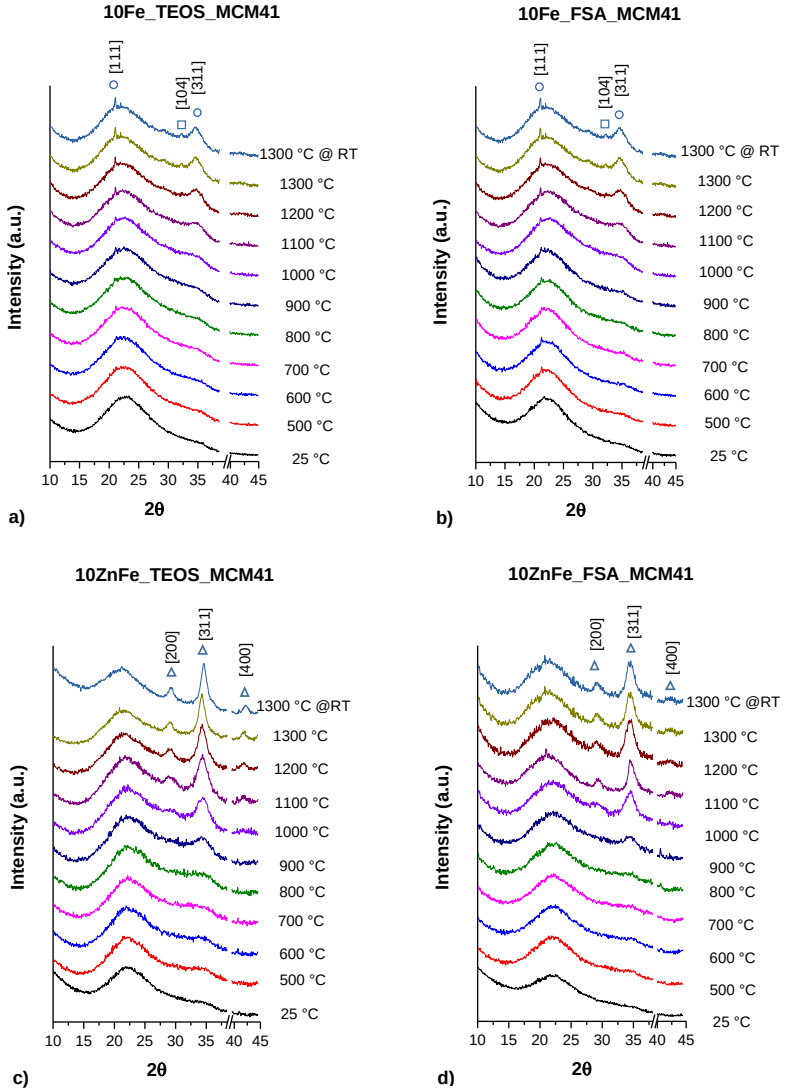


***Figure 7.8*** *WA-XRD patterns collected by using a high temperature chamber in the range of temperatures 25-1300 °C plus an additional spectrum recorded at room temperature at the end of the heating cycle (1300 °C @ RT) of the four nanocomposites. For clarity's sake, patterns have been normalized and the (111) peak associated with the reflex of the Pt foil used as the sample holder, centred at 39° has been removed.*

Single peak analysis, performed by means of the software Origin using pseudo-Voigt functions and the Scherrer equation, was performed for the four samples treated at 1300 °C and cooled down to room temperature. The patterns of the two γ-$Fe_2O_3$-bearing composites show crystallite size within the 4-9.5 nm range with an average size (7 ± 4) nm. The great difference in terms of crystallite size (more than the double) determined for the (311) and (200) reflexes is an indication of a preferred crystal growth along the (220) direction with the formation of rod-like particles. This phenomenon can be justified by taking into account the fact that the wall channels impose (4 nm) such physical limits while that the particles can grow only on the same direction of the porous channel. This behaviour is very similar in both TEOS and FSA-derived samples. Going to $ZnFe_2O_4$ nanocomposites, similar results were obtained but the same phenomenon resulted to be less evident. In fact, the average size is, once again, about 7 nm but with a much smaller standard deviation (1 nm), an indication of greater similiraties in $\bar{D}_{XRD}$ values for the different reflexes. However, a difference in the range of 1.6-2.4 nm can be revealed, confirming a preferred particle growth along the (220) plane. A further analysis was performed on 10ZnFe_TEOS_MCM41 at 1300° C as a shift of the (311) peak towards lower angles was observed in respect to the 1300 °C @ RT sample. As expected, a higher value (8,67 ± 0.02) nm of cell parameter was calculated if compared with the cooled one (8.59 ± 0.3) nm, caused by the expansion of the cell at such a high temperature. Cooling does not exert any significant effect on crystallite size, being (7.4 ± 1.4) nm for 1300 C and (7.2 ± 0.8) nm for the 1300 °C RT sample. Further information about the thermal stability of the mesostructure should be collected by measuring the samples at different temperature in the small-angle region of XRD. However, preliminary measurements pointed out that between 600-700 °C on MCM-41 derived from TEOS surface area start to diminish, indicating a partial collapse of the mesostructure.

***Table 7.5*** *Single peak analysis carried out on the WA-XRD patterns of the four nanocomposites. K represents a constant related to the crystillite shape, λ is the X-ray wavelength, and $D_{XRD}$ is the measured crystallite dimension; $a_0$ represents the lattice parameter. Mean values are indicated with a bar.*

| Sample | K | λ (Å) | [hkl] | 2θ (°) | $D_{XRD}$ (nm) | $\bar{D}_{XRD}$ (nm) | SD | $a_0$ (Å) | $\bar{a}_0$ (Å) | SD |
|---|---|---|---|---|---|---|---|---|---|---|
| **10Fe_MCM41_FSA 1300 °C @ RT** | 0.9 | 1.5418 | 220 | 29.27 | 9.49 | 6.70 | 4.92 | 8.63 | 8.61 | 0.05 |
| | 0.9 | 1.5418 | 311 | 34.73 | 3.95 | | | 8.57 | | |
| **10Fe_MCM41_TEOS 1300 °C @ RT** | 0.9 | 1.5418 | 220 | 29.27 | 9.40 | 6.67 | 3.87 | 8.73 | 8.70 | 0.06 |
| | 0.9 | 1.5418 | 311 | 34.73 | 3.93 | | | 8.64 | | |
| **10ZnFe_MCM41_FSA 1300 °C @ RT** | 0.9 | 1.5418 | 220 | 29.50 | 8.92 | 8.11 | 1.35 | 8.57 | 8.55 | 0.05 |
| | 0.9 | 1.5418 | 311 | 34.92 | 6.55 | | | 8.52 | | |
| | 0.9 | 1.5418 | 400 | 42.70 | 8.86 | | | 8.47 | | |
| **10ZnFe_MCM41_TEOS 1300 °C @ RT** | 0.9 | 1.5418 | 220 | 29.27 | 8.14 | 7.17 | 0.85 | 8.63 | 8.59 | 0.03 |
| | 0.9 | 1.5418 | 311 | 34.62 | 6.57 | | | 8.59 | | |
| | 0.9 | 1.5418 | 400 | 42.22 | 6.80 | | | 8.56 | | |
| **10ZnFe_MCM41_TEOS 1300 °C** | 0.9 | 1.5418 | 220 | 29.07 | 7.43 | 7.42 | 1.24 | 8.69 | 8.67 | 0.02 |
| | 0.9 | 1.5418 | 311 | 34.32 | 6.17 | | | 8.67 | | |
| | 0.9 | 1.5418 | 400 | 41.81 | 8.65 | | | 8.64 | | |

The results described in this section prove that FSA-derived nanocomposites show similar thermal stability featured by their TEOS-derived counterparts. It is also highlighted that the mesostructure sintering phenomena of the active phases are prevented from occurring, although its occurrence can be evidenced starting from 600-700 °C. The so-detected temperature range collocates itself well-above the ones required for mid-temperature treatment for the sweetening sour syngas, making the utilization of these nanocomposite possible for this process. In this framework, the delsulfidation and regeneration capabilities of the samples 10Fe_FSA_MCM41 and 10Fe_TEOS_MCM41 counterpart will be tested and the results discussed in the next section.

## 7.5 Assessing Desulfidation Performances and Regeneration Capability

In order to prove its $H_2S$ removal capacity, the sorbent 10Fe_FSA_MCM41 underwent three sulfidation and regeneration cycles. The $H_2S$ removal performances, expressed in terms of sulfur retention capacity (SRC) of the three sulfidation runs. For brevity's sake, only some of these profiles are reported in 7.9. A comparison with the anologous nanocomposite synthetized in the same conditions using TEOS as precursor and with Katalco 32-5, a commercial unsupported ZnO-based sorbent was also drawn.

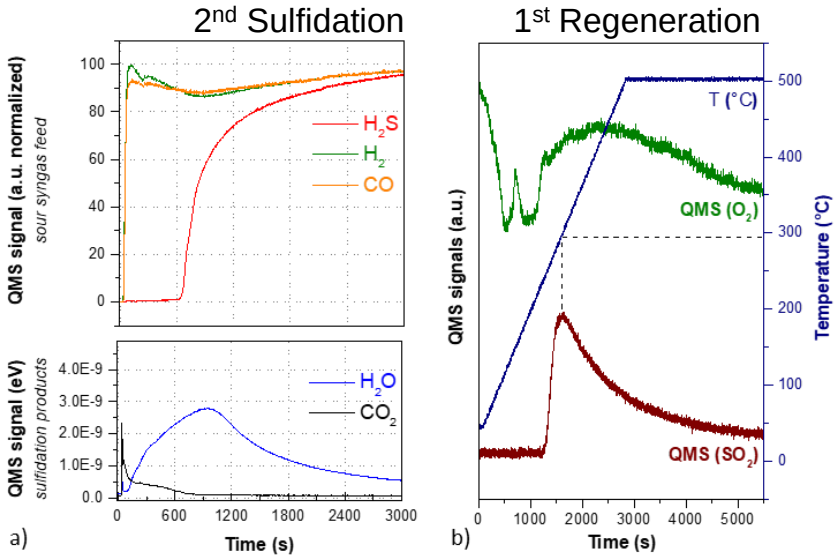


***Figure 7.9*** *(a, top) $H_2S$, CO, and $H_2$ Quadrupole Mass Spectrometer (QMS) profiles normalized for the sample 10Fe_FSA_MCM4; (a, bottom) $H_2O$ and $CO_2$ sulfidation products signals (eV) during the second sulfidation of the composite; b) $SO_2$ and $O_2$ QMS signals during the first regeneration run.*

On the top of the figure, the profiles of the fed sour syngas components show that only $H_2S$ remains at values close to zero at the beginning of the process, pointing out its selective retention on the sorbent. In correspondence with the $H_2$ and CO releases, the formation of $CO_2$, as a result of the possible reduction of Fe III by CO, and the subsequent production of $H_2O$ were spotted (same figure, bottom). This is in agreement with the substitution reaction (eq. 28), reported as follows.

$$Fe_2O_3 + 3\,H_2S \longrightarrow Fe_2S_3 + 3\,H_2O \qquad \textbf{(Eq. 28)}$$

$Fe_2S_3$ is known to be a thermodynamically unstable phase that easily transforms into pyrite[17] and $Fe_3S_4$ (eq. 29),

$$2\,Fe_2S_3 \longrightarrow FeS_2 + Fe_3S_4 \qquad \textbf{(Eq. 29)}$$

or pyrite, pyrrhotite and sulfur (eq. 30,where $\alpha$, $\beta$, and $\gamma$ represent the relative molar amounts).

$$Fe_2S_3 \longrightarrow g\,FeS_2 + \beta\,FeS_x + \gamma\,S \qquad \textbf{(Eq. 30)}$$

The formation of a small amount of $CO_2$ is justified by the redox reaction of CO which can lead to the formation of FeO and, as a consequence, a small amount of FeS can be formed (eq. 31 and 32).[18]

$$3\,Fe_2O_3 + CO \longrightarrow 2\,FeO + CO_2 \qquad \textbf{(Eq. 31)}$$

$$FeO + H_2S \longrightarrow FeS + H_2O \qquad \textbf{(Eq. 32)}$$

The low content of the iron oxide active phase (10 % w/w) and the ultrasmall size of the particles ($<$ 3 nm) do not allow wide angle XRD analysis to provide incontrovertible proof about the crystallographic phases formed during the sulfidation processes and therefore to confirm the proposed reaction scheme for $H_2S$ removal.
The slight reduction of the $H_2$ QMS signal in combination with the increase revealed for $H_2O$ does not preclude the possibility of reduction of the iron oxide phase by $H_2S$ according to the equation 33:

$$Fe_2O_3 + 2\,H_2S + H_2 \longrightarrow 2\,FeS + 3\,H_2O \qquad \textbf{(Eq. 33)}$$

The regeneration round, which followed sulfidation, was carried out by heating the sample under flowing air (20 $cm^3\ g^{-1}$) at 500 °C with a heating rate of 10 °C $min^{-1}$; the outlet gas composition was monitored by a quadrupole mass spectrometer (QMS) as shown if figure 7.9. The reactions involved in the regeneration process are exemplified by equations 34,35,and 36.[13]

$$4\,FeS_2 + 11\,O_2 \longrightarrow 2\,Fe_2O_3 + 8\,SO_2 \quad \textbf{(Eq. 34)}$$

$$Fe_3S_4 + 2\,O_2 \longrightarrow 2\,Fe_3O_4 + 4\,S \quad \textbf{(Eq. 35)}$$

$$FeS_x + xO_2 \longrightarrow Fe_2O_3 + xSO_2 \quad \textbf{(Eq. 36)}$$

The reduced phase (FeS) could instead lead to the formation of sulphur (eq. 37).[13]

$$4\,FeS + 3\,O_2 \longrightarrow 2\,Fe_2O_3 + S_8 \quad \textbf{(Eq. 37)}$$

The resulting gas profiles are reported in figure 7.9b. In the range between 100 °C and 250 °C, two main $O_2$ retention phenomena occurred followed by $SO_2$ release starting at 300 °C. These findings evidenced the restoration of the original iron oxide phase through these possible reaction. In terms of $H_2S$ removal perfomances, expressed in terms of sulfur retention capacity (SRC) of the three sulfidation runs, the sample 10Fe_FSA_MCM41 shows similar performances when compared with the TEOS-derived homologous, with steady behaviour over all the three sulfidation runs, and much better performances if compared with Katalco 32-5[12] (figure 7.10 and table 7.6).

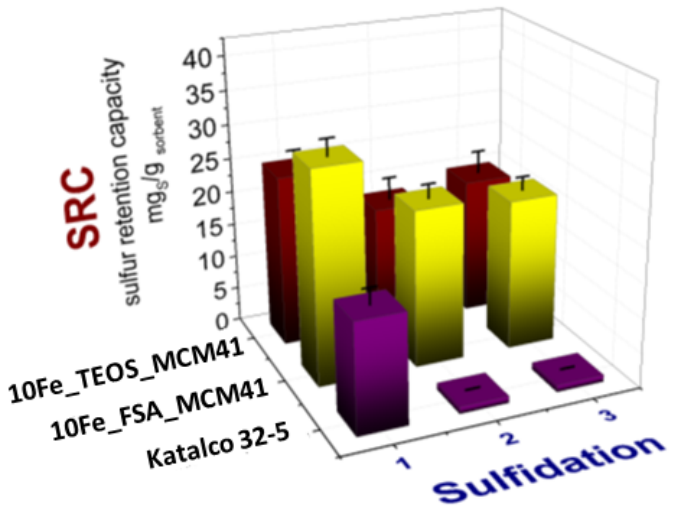


***Figure 7.10*** *$H_2S$ removal performances of FSA_MCM-41_$Fe_2O_3$ compared with TEOS_MCM-41_$Fe_2O_3$ and Katalco 32-5, unsupported ZnO-based commercial sorbent previously tested.*[12]

***Table 7.6*** *Breakthrough time ($B_t$) and sulfur retention capacity (SRC) of fresh and regenerated 10Fe_FSA_MCM41, 10Fe_TEOS_MCM41, and Katalco 32-5.[12] The label XR (with X = 1-3) refers to the regenerated material after X sulfidation/regeneration cycles. The error in SRC value is estimated to be ± 2 mg S $g_{sorbent}^{-1}$.*

| Sample | Sulfidation Run | $B_t$ (s) | SRC (mg S $g_{sorbent}^{-1}$) |
|---|---|---|---|
| **10Fe_FSA_MCM41** | 1st | 481 | 31 |
| **10Fe_FSA_MCM41_2R** | 2nd | 353 | 23 |
| **10Fe_FSA_MCM41_3R** | 3rd | 338 | 22 |
| **10Fe_TEOS_MCM41** | 1st | 187 | 25 |
| **10Fe_TEOS_MCM41_2R** | 2nd | 136 | 18 |
| **10Fe_TEOS_MCM41_3R** | 3nd | 156 | 20 |
| **Katalco 32-5** | 1st | 122 | 16 |
| **Katalco 32-5_2R** | 2nd | 10 | 1 |
| **Katalco 32-5_3R** | 3rd | 13 | 2 |

## 7.6 Comparison between the Fresh and the Three-Time Regenerated Sorbent

Upon three cycles of sulfidation/regeneration, a comparison between the fresh 10Fe_FSA_MCM41 sample and the three-time regenerated counterpart, referred to as 10Fe_FSA_MCM41_3R, was drawn to assess whether the latter preserved the original textural properties of the fresh. **SA-XRD** and **$N_2$-physisorption** were performed for this purpose. **Small-Angle XRD** pattern shows the three typical reflexes of an MCM-41 material, indicating the preservation of the hexagonal mesoporous order over the three cycles of sulfidation. **$N_2$-physisorption** measurements also confirm the retention of the textural properties: similar values for pore volume, pore width, and very similar pore size distribution were found. Surface area ($S_{BET}$), pore volume ($V_p$), DFT-determined pore diameter, lattice spacing ($d_{100}$), hexagonal unit cell parameter ($a_0$), and wall thickness ($w_t$) of the bare sample MCM41-FSA, the fresh (10Fe_FSA_MCM41), and the three-time regenerated sorbent (10Fe_FSA_MCM41_3R), although a decrease of 10 % in the value of surface area was observed as in the case of sorbents derived from TEOS.[13,18] Figure 7.11 along with table 7.7 report these findings.

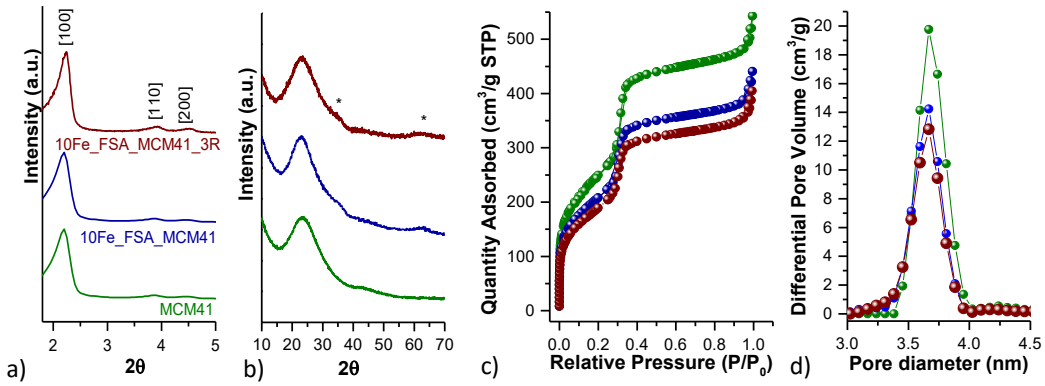


***Figure 7.11*** *(a, b) SA- and WA-XRD patterns, c) $N_2$-physisorption isotherms, and d) pore size distributions of FSA-derived MCM-41 and its 10 % w/w $Fe_2O_3$ nanocomposite in the fresh (10Fe_FSA_MCM41) and regenerated (10Fe_FSA_MCM41_3R) state.*

***Table 7.7*** *Surface area ($S_{BET}$), pore volume ($V_p$), DFT-determined pore diameter ($D_{P(DFT)}$), lattice spacing ($d_{100}$), hexagonal unit cell parameter ($a_0$), and wall thickness ($w_t$) of the bare sorbent, the pristine $Fe_2O_3$-bearing nanocomposite, and the same naocomposite after three cycles of sulfidation and regeneration. Data labelled with * have already been reported in previous sections.*

| Sample | $S_{BET}$ ($m^2$ $g^{-1}$) | $V_P$ ($cm^3$ $g^{-1}$) | $D_{p\ (DFT)}$ (nm) | $d_{100}$ (nm) | $a_0$ (nm) | $w_t$ (nm) |
|---|---|---|---|---|---|---|
| **MCM41 (FSA_T50_3h_Hyd)*** | 886 | 0.7 | 3.7 | 3.8 | 4.4 | 0.7 |
| **10Fe_FSA_MCM41*** | 754 | 0.6 | 3.6 | 3.8 | 4.4 | 0.7 |
| **10Fe_FSA_MCM41_3R** | 685 | 0.7 | 3.7 | 3.8 | 4.4 | 0.7 |

*Relative standard deviation: %RSD($S_{BET}$)=2.1%; %RSD ($V_p$)=1.1%; %RSD ($D_p$)=1.8%. $d_{100}$ and $a_0$ were obtained from XRD data. For bimodal pore size distributions, two values of $D_{p(DFT)}$ are reported.*

## 7.7 Conclusions

The results evidence reported in this chapter support the use of the γ-$Fe_2O_3$-bearing FSA-derived MCM-41nanocomposite as an alternative support to its TEOS-derived analogous in order to manufacture efficient and highly regenerable sorbents for $H_2S$ removal at mid-temperature. Moreover, being this composite regenerable at temperatures close to the one whereby sulfidation process is carried out (300 °C), the iron oxide active phase was proven to be promising in the development of a new generation of solid sorbents for processes based on IGCC systems, as a result of both the low cost and toxicity of the active phase and the utilization of waste FSA as a precursor. MCM-41 is rarely used in applications at mid- and high-temperature, probably because of the

possible collapse of the mesoporous structure, suppositionally fragile because of its small pore size and small wall thickness. However, the results clearly shows that the FSA-derived MCM-41 nanocomposite, after undergoing sulfidation (300 °C) and regeneration (500 °C) retained their stability. Moreover, the results highlight that the surface area seems to play a pivotal role in the performance, given the textural properties of both TEOS- and FSA-derived MCM-41 resulted to be similar. In fact, being the kinetic diameter of $H_2S$ and $N_2$ comparable, the specific surface area values calculated by $N_2$-physisorption should be considered as the effective surface accessible to $H_2S$ molecules. Besides showing similar performances when compared with its TEOS-derived homologue, the data here reported confirm that the sample 10Fe_FSA_MCM41 also retained its mesostructure after undergoing three cycles of sulfidation/regeneration and this occurs with minimal variations in textural properties. This evidence offers further decisive support for the use of FSA-derived materials in the manufacture of nanocomposites in alternative to those whose scaffold was obtained from silicon alkoxides, entailing significant environmental and economical advantages.

*Unfortunately, further experiments concerning the evaluation of the $H_2S$ performance capacity of the $ZnFe_2O_4$-bearing nanocomposites), to verify possible synergistic effect of zinc and iron in the mixed oxide, planned for March-April 2020, were not carried out as a consequence of the pandemic crisis.*

# References

[1] Westmoreland, P. R.; Harrison, D. P. Evaluation of Candidate Solids for High-Temperature Desulfurization ofLlow-Btu Gases. *Environmental Science and Technology* **1976**, *10*, 659–661, DOI: 10.1021/es60118a010.

[2] Dolan, M. D.; Ilyushechkin, A. Y.; McLennan, K. G.; Sharma, S. D. Sulfur Removal from Coal-Derived Syngas. Thermodynamic Considerations and Review. *Asia-Pacific Journal of Chemical Engineering* **2012**, *7*, 1–13, DOI: 10.1002/apj.528.

[3] Samokhvalov, A.; Tatarchuk, B. J. Characterization of Active Sites, Determination of Mechanisms of $H_2S$, COS and $CS_2$ Sorption and Regeneration of ZnO Low-Temperature Sorbents: Past, Current and Perspectives. *Phys. Chem. Chem. Phys.* **2011**, *13*, 3197–3209, DOI: 10.1039/C0CP01227K.

[4] Cheah, S.; Carpenter, D. L.; Magrini-Bair, K. A. Review of Mid- to High-Temperature Sulfur Sorbents for Desulfurization of Biomass- and Coal-derived Syngas. *Energy & Fuels* **2009**, *23*, 5291–5307, DOI: 10.1021/ef900714q.

[5] Davydov, A.; Chuang, K. T.; Sanger, A. R. Mechanism of $H_2S$ Oxidation by Ferric Oxide and Hydroxide Surfaces. *The Journal of Physical Chemistry B* **1998**, *102*, 4745–4752, DOI: 10.1021/jp980361p.

[6] Sánchez-Hervás, J.; Otero, J.; Ruiz, E. A study on Sulphidation and Regeneration of Z-Sorb III Sorbent for $H_2S$ Removal from Simulated ELCOGAS IGCC Syngas. *Chemical Engineering Science* **2005**, *60*, 2977–2989, ISSN: 0009-2509, DOI: https://doi.org/10.1016/j.ces.2005.01.018.

[7] Varghese, S.; Cutrufello, M.; Rombi, E.; Cannas, C.; Monaci, R.; Ferino, I. CO Oxidation and Preferential Oxidation of CO in the Presence of Hydrogen over SBA-15-Templated CuO-$Co_3O_4$ Catalysts. *Applied Catalysis A: General* **2012**, *443-444*, 161–170, ISSN: 0926-860X, DOI: https://doi.org/10.1016/j.apcata.2012.07.038.

[8] Rombi, E.; Cutrufello, M. G.; Cannas, C.; Casu, M.; Gazzoli, D.; Occhiuzzi, M.; Monaci, R.; Ferino, I. Modifications Induced by Pretreatments on Au/SBA-15 and their Influence on the Catalytic

Activity for Low Temperature CO Oxidation. *Phys. Chem. Chem. Phys.* **2009**, *11*, 593–602, DOI: 10.1039/B813982B.

[9] Belmabkhout, Y.; Heymans, N.; De Weireld, G.; Sayari, A. Simultaneous Adsorption of $H_2S$ and $CO_2$ on Triamine-Grafted Pore-Expanded Mesoporous MCM-41 Silica. *Energy & Fuels* **2011**, *25*, 1310–1315, DOI: 10.1021/ef1015704.

[10] Liu, X.; Wang, R. Effective Removal of Hydrogen Sulfide Using 4A Molecular Sieve Zeolite Synthesized from Attapulgite. *Journal of Hazardous Materials* **2017**, *326*, 157–164, ISSN: 0304-3894, DOI: https://doi.org/10.1016/j.jhazmat.2016.12.030.

[11] Garcia, C. L.; Lercher, J. A. Adsorption of Hydrogen Sulfide on ZSM 5 Zeolites. *The Journal of Physical Chemistry* **1992**, *96*, 2230–2235, DOI: 10.1021/j100184a038.

[12] Cara, C. Siliceous and non-siliceous Mesostructured Iron Oxide Nanocomposites for $H_2S$ Removal from Syngas., PhD Thesis, University of Cagliari, 2017.

[13] Cara, C.; Rombi, E.; Musinu, A.; Mameli, V.; Ardu, A.; Sanna Angotzi, M.; Atzori, L.; Nižňanský, D.; Xin, H. L.; Cannas, C. MCM-41 Support for Ultrasmall $\gamma$-$Fe_2O_3$ Nanoparticles for $H_2S$ Removal. *J. Mater. Chem. A* **2017**, *5*, 21688–21698, DOI: http://dx.doi.org/10.1039/C7TA03652C.

[14] Cara, C.; Rombi, E.; Ardu, A.; Vacca, M. A.; Cannas, C. Sub-Micrometric MCM-41 Particles as Support to Design Efficient and Regenerable Maghemite-Based Sorbent for $H_2S$ Removal. *Journal of Nanoscience and Nanotechnology* **2019**, *19*, 5035–5042, ISSN: 1533-4880, DOI: https://doi.org/10.1166/jnn.2019.16800.

[15] Kundu, A.; Upadhyay, C.; Verma, H. Magnetic Properties of a Partially Inverted Zinc Ferrite Synthesized by a New Coprecipitation Technique Using Urea. *Physics Letters A* **2003**, *311*, 410–415, DOI: 10.1016/S0375-9601(03)00509-7.

[16] Cara, C.; Mameli, V.; Rombi, E.; Pinna, N.; Angotzi, M. S.; Nižňanský, D.; Musinu, A.; Cannas, C. Anchoring Ultrasmall $Fe^{III}$-Based Nanoparticles on Silica and Titania Mesostructures for Syngas $H_2S$ Purification. *Microporous and Mesoporous Materials* **2020**, *298*, 110062,

ISSN: 1387-1811, DOI: https://doi.org/10.1016/j.micromeso.2020.110062.

[17] Mureddu, M.; Ferino, I.; Rombi, E.; Cutrufello, M.; Deiana, P.; Ardu, A.; Musinu, A.; Piccaluga, G.; Cannas, C. ZnO/SBA-15 Composites for Mid-Temperature Removal of $H_2S$: Synthesis, Performance and Regeneration Studies. *Fuel* **2012**, *102*, Special Section: ACS Clean Coal, 691–700, ISSN: 0016-2361, DOI: https://doi.org/10.1016/j.fuel.2012.05.013.

[18] Cara, C.; Rombi, E.; Mameli, V.; Ardu, A.; Sanna Angotzi, M.; Niznansky, D.; Musinu, A.; Cannas, C. $\gamma$-$Fe_2O_3$-M41S Sorbents for $H_2S$ Removal: Effect of Different Porous Structures and Silica Wall Thickness. *The Journal of Physical Chemistry C* **2018**, *122*, 12231–12242, DOI: 10.1021/acs.jpcc.8b01487.

# 8

# Conclusions and Future Insights

The work presented in this thesis has highlighted the importance of utilizing $H_2SiF_6$, an obnoxious waste material, as an alternative and inexpensive silicon source. After having been an overlooked topic of research with a limited number of articles published about this topic, the scientific community has recently started to acknowledge the importance of investigating ways to valorize $H_2SiF_6$, coming up with interesting applications of FSA-derived siliceous materials in industrial settings. In this context, the present thesis has investigated the utilization of $H_2SiF_6$ in obtaining both precipitated silica for tyre reinforcement and nanocomposites by impregnation of bare MCM-41materials with a suitable active phase to be used in the desulfidation of syngas from coal. Utilizing FSA in lieu of the most common silicon precursors in these contexts may lead to lower costs of the production of both the above-mentioned siliceous materials, let alone the favourable environmental impact of recovering and reusing an otherwise useless industrial waste.

As far as precipitated silica for tyre reinforcement is concerned, a systematic screening of the effects of pH, temperature, addition rate of FSA, concentration of reactants, and reaction *medium* on the properties of the so-obtained precipitated silica was carried out. This batch of experiments allowed to obtain promising samples, with suitable values of specific surface area, for the use in tyre reinforcement and were then used in preparing tread compounds that underwent testing to assess their performances. A series of attempts aimed at working out the best washing procedure was undertaken beforehand to ensure the obtainment of fluoride-free samples. The preliminary work and the obtained data reported in this thesis may constitute a basis for further synthesis methods

to obtain high-quality $SiO_2$ from $H_2SiF_6$ in lieu of conventional silicon sources.

As for the FSA-derived MCM-41 materials, a similar approach was adopted where parameters such as temperature, time, presence of ethyl acetate, and hydrothermal treatment in autoclave were ordinately changed to figure out their effects on the textural properties on the synthesized MCM-41 materials. However, in order to ascertain the most favourable conditions to obtain FSA-derived MCM-41, a head-to-head comparison was also drawn with their TEOS-derived counterparts, which were synthesized in parallel under the same experimental conditions. The $\gamma$-$Fe_2O_3$ nanocomposites derived from the best FSA-derived were characterized and tested as sorbent in the $H_2S$ removal from syngas with comparable results with the TEOS-derived ones. Thermal stability was also assessed. Furthermore, a Soxhlet extraction with ethanol from the MCM-41 material was attempted with encouraging results in order to recover the templating agent. The combined utilization of FSA as the siliceous precursor and the recovery of the templating agent might be the first step in the direction of envisaging a low-cost and environmentally friendly industrial process to manufacture such materials while recovering such a valuable reactant.

In conclusion, the work described in this thesis has confirmed the feasibility of utilizing hexafluorosilicic acid as an alternative silicon source with applications in the tyre industry and in environmental remediation. It could also constitute the basis of further research on the numerous fields where silica is involved (such as nanomedicine, molecular sieving, catalysis, *etc.*) and the use of an alternative silicon source may be advantageous.

# A

# Equipment and Techniques

*The following appendix will give a succinct description of the instruments and the main analytical techniques used throughout this work.*

## A.1 X-ray Diffraction

X-ray diffraction is a powerful technique which reveals details about the crystalline structure of a given sample. Diffraction is the phenomenon whereby the atoms of a crystal cause an interference pattern of the waves constituting an incident beam of x-rays. These interferences may be either destructive or constructive. Bragg's law (Eq. A.1) predicts the angles for coherent and incoherent scattering from a crystal lattice.

$$2dsin\theta = n\lambda \tag{A.1}$$

where $d$ represents the spacing between the diffracting planes, $\theta$ is the incident angle, $\lambda$ is the wavelength of the beam while $n$ is an integer number. The XRD spectra presented in this thesis were collected on either on a Seifert or an Panalytical X'Pert Pro diffractometer with a θ-θBragg-Brentano geometry. The X-ray radiation of choice was Cu $K_\alpha$. Throughout this work, low-angle and wide-angle measurements were carried out in the range of 2θ between 0.9-6° and 8-70°, respectively. The lattice parameter ($a_0$) for the hexagonal ($P6mm$) porous structure was calculated according to Eq. A.2:

$$a_0 = \frac{2d_{100}}{\sqrt{3}} \tag{A.2}$$

Studies of thermal stabilities were carried out by using a High Temperature Chamber (HTC) Anton Parr HT-106 up to 1300°C.

## A.2 Nitrogen Physisorption Measurements

$N_2$-physisorption measurements provide valuable information about surface area, pore volume, and pore size distribution of the sample. Adsorption comes about at the interface of a solid and a fluid phase and consists in the enrichment of material or increase in the density of the fluid in the vicinity of an interface.[1] In this work, surface area values were calculated by the BET model while pore size distribution calculations were performed differently according to the given sample, whether it be mesostructured or precipitated silica. As far as the latter is concerned, pore size distribution was assessed by using the conventional Barrett, Joyner, and Halenda method (BJH). In the case of mesostructured $SiO_2$, pore size distributions were calculated by means of the density functional theory (DFT), a computational quantum mechanical modelling that provides more accurate pore diameter values in mesostructured materials compared with other more conventional calculation methods. In fact, applying the BJH model on mesostructure materials like MCM-41 may result in lower pore diameter estimates, approximately less than 20% or even more.[2] The measurements on precipitated silica were performed on a Sorptomatic 1990 System. A Micromeritics ASAP 2020 system was instead used to test the mesostructured materials. All these analyses were preceded by activation, outgassing them under vacuum for 12 hours at 250 °C with a heating rate of 1 °C $min^{-1}$.

## A.3 Transmission Electron Microscopy

Transmission Electron Microscopy (TEM) is a technique in which a beam of electrons is transmitted through a sample to form an image. The specimen is usually an ultrathin section or a suspension laid by dropping on a grid. The image stems from the interaction of the electrons with the specimen as the beam is transmitted through it. The image is then magnified and focused onto an imaging device, such as a fluorescent screen, a layer of photographic film, or a sensor such as a scintillator attached to a charge-coupled device.[3] A simplified diagram a TEM microscope is given in Fig. A.1.

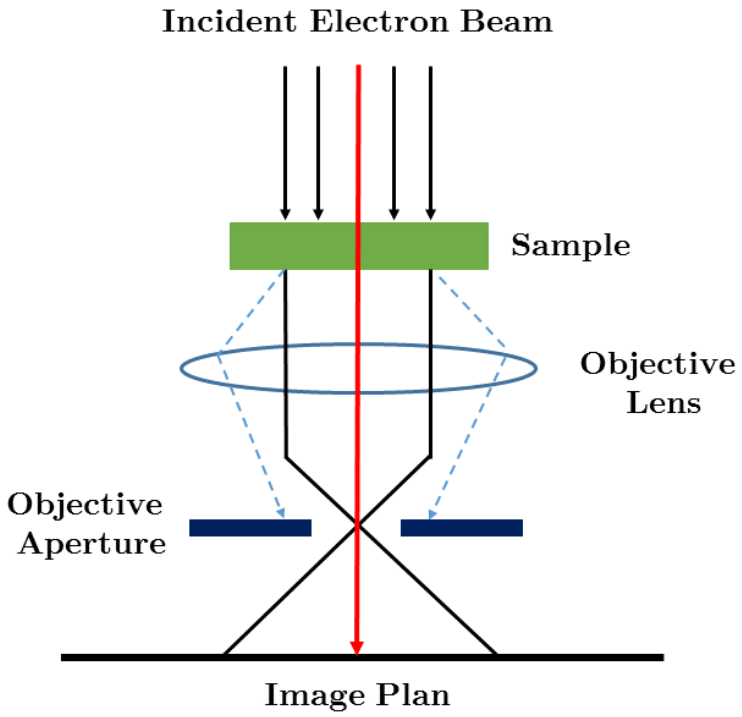


***Figure A.1*** *Simplified diagram of a TEM microscope*

Prior to analysis, the samples obtained in this work were dispersed in ethanol, sonicated for a couple of minutes, and then dropped on a copper grid. TEM micrographs were obtained on a TEM JEM 1400-PLUS microscope operating at an accelerating voltage of 120 kV. HRTEM was also performed on some samples to gauge *d*-spacing and pore size of some of samples synthesized on a JEM 2010 UHR equipped with a Gatan Imaging Filter (GIF) featuring a 15 eV window and a 794 slow scan CCD camera.

## A.4 FT-Infrared Spectroscopy

Infrared Spectroscopy is based on the interactions between infrared radiation and the matter, exploiting the fact that molecules absorb frequencies that are characteristic of their structure. In doing so, FT-IR is able to reveal the bonds and the chemical groups of a given sample.[4] An Equinox 55 was used. The investigated spectral window ranged between 400 and 4000 $cm^{-1}$. Before analysis, an apt amount of sample was finely ground and dispersed in KBr. The resulting powder was then pressed to obtain a pellet. A typical FT-IR spectra of MCM-41 feature characteristic bands: the symmetric stretching modes related to the $SiO_4$

tetrahedra at 1240, 1060, and 800 $cm^{-1}$; the stretching mode of the Si-OH groups at 960 $cm^{-1}$; the bending mode at 460 $cm^{-1}$ related to the O-Si-O groups.[5,6]. Infrared spectra investigating the content of CTAB in the MCM-41 materials were also performed. Characteristic absorption bands of this compound are: the stretching mode at 3010 $cm^{-1}$ of the N-$CH_3$ group; the symmetric and asymmetric stretching and bending modes of the $CH_2$ groups; the C-C stretching modes at 960 and 900 $cm^{-1}$.

## A.5 Mössbauer Spectroscopy

Mössbauer spectroscopy is based on the phenomenon of the nearly recoil-free resonant absorption and emission of $\gamma$-rays in solids. Usually, a solid sample is exposed to a beam of $\gamma$-radiation while a detector measures the intensity of the beam transmitted. The atoms constituting the emitting source must be of the isotope of interest in the sample. To date, Mössbauer effect has been observed in over 40 elements but the most common analysis is performed on $^{57}Fe$ by using $^{57}Co$ as $\gamma$ source. A Mössbauer spectrum is characterized by an extremely fine energy resolution and provides valuable information about the nuclear environment of the atoms of interest. The nuclear interactions determining how a Mössbauer spectrum appears are isomer shift, quadrupole splitting, and magnetic splitting. Mössbauer measurements were performed on a Wissel spectrometer calibrated by using a foil of $\alpha$-Fe as the reference standard. Measurements were carried out by laying about 40 mg of sample in a special plastic sample holder. Analysis was performed over a time span up to 24 hours. Data were then elaborated by using the software NORMOS.

## A.6 Magic Angle Soild State $^{29}Si$ ss-NMR Spectroscopy

Unlike NMR performed on a solution, Solid State Nuclear Magnetic Resonance spectroscopy (ss-NMR) is characterized by the presence of orientation-dependent interactions. For this reason, ss-NMR spectra show broader signals, given the absence of homogeneous tumbling typical of an analyte in solution.[7] SS-NMR provides the same information a "conventional" NMR would do but, to do so, a number of additional techniques and equipment may

be necessary, including magic-angle spinning (MAS), cross polarization, specially implemented 2D experiments, enhanced probe electronics, *etc.* These supplemental techniques are instrumental in minimizing anisotropic interactions between *nuclei* and increasing S/N in spectra of *nuclei*, especially those with $S \neq \frac{1}{2}$. Among these techniques, Magnetic Angle Spinning consists in spinning a sample at an apt frequency (up to 130 KHz) at the magic angle $\theta_m$ (54.74°, where $cos2\theta_m = \frac{1}{3}$).[7] In fact, when a sample is spinned at this angle, the main three interactions (dipolar, chemical shift anisotropy, quadrupolar) are averaged. The samples examined by $^{29}$Si-NMR were packed in a 2.5 mm diameter MAS rotor (internal volume 14 $\mu$L). Spectra were recorded at room on an Avance III HD spectrometer (Bruker, Billerica, MA, USA) operating at a $^{1}$H frequency of 600 MHz ($^{29}$Si: 119.229 MHz). Octakis(trimethylsiloxy)silsesquioxane ($Q_8M_8$) was used as external reference for the chemical shift scale, by setting its high frequency $^{29}$Si resonance at +12.6 ppm. $_{29}$Si-MAS spectra were acquired at 10 kHz spinning rate and using a 1.8 $\mu$s pulse (30°), 30 s delay time, 6 ms acquisition time, and a spectral width of 50 kHz for 1700 transients. *Spectra* processing and analysis, including deconvolution, were carried out by using the software iNMR v.5.4.6 (2015, Mestrelab Research).

## A.7 Magnetic Measurements

Magnetic measurements were carried out on a Superconducting Quantum Interference Device (S.Q.U.I.D.). A S.Q.U.I.D. is a sensitive magnetometer consisting in a superconducting magnet to produce powerful magnetic fields from zero to several negative and positive Tesla in a range of temperature form 4.2 K to 400 K. Two protocols exist to perform measurements of magnetization *vs.* temperature: ZFC and FC. These methods are the most commonly used to investigate superparamagnetic relaxation in nanoparticles.

The ZFC involves the cooling down of the sample from high temperature , with all the particle exhibiting superparamagnetic state, to a given low temperature in a zero magnetic field. A static magnetic field is then applied and magnetization is measured over warming up ($M_{ZFC}$). The so-obtained curve is therefore known as Zero Field Cooled.

On the other hand, FC protocol consists in cooling the sample in a DC field and then measuring the magnetization while the sample is warmed up without

quenching the applied field. If a magnetic field is applied during the cooling process, all the net magnetic moments of the nanoparticles result to be aligned to the field direction. When at low temperature, the magnetization direction of each particle is stuck along the field. An increase in temperature leads to an increased number of particles in the paramagnetic. This leads in turn to a monotonical decrease in magnetization bringing about a typical paramagnetic behaviour.[8] In this work, DC magnetic properties were studied on a Quantum Design PPMS Dynacool ($H_{max}$ = 90 kOe) by using the VSM module. Field dependence on magnetization has been studied at 5 K between -90 kOe and +90 kOe. Dependence on temperature of the magnetization was studied by using Zero-Field-Cooled (ZFC), Field-Cooled (FC) protocols: the sample was cooled down from 300 to 2 K in zero magnetic field; then, the curve was recorded under a static magnetic field of 250 Oe. $M_{ZFC}$ was measured during the warm-up from 2 to 300 K, whereas MFC was recorded both during cooling and warm-up. From these data, the characteristics temperatures $T_{max}$ and $T_{irr}$ were computed as follows. $T_{max}$ is the temperature of the maximum in the Zero-Field-Cooled curve. $T_{irr}$ has been calculated by considering a 3 % difference between $M_{FC}$ and $M_{ZFC}$.

## A.8 X-Ray Fluorescence Spectroscopy

X-ray Fluorescence (XRF) is an analytical technique that exploits the interaction of X-rays with a material to determine its elemental composition. XRF is usually suitable for solids, liquids, and powders. Two main XRF methodologies exist: energy (ED-XRF) and wavelength dispersive (WD-XRF), with each method having its own advantages and drawbacks. Energy dispersive detection system directly measures the different energies of the emitted x-rays from the sample by counting and plotting the relative numbers of x-ray photons whereas WD-XRF uses crystals to disperse the fluorescence spectrum into individual wavelengths of each element. Low background and resolution spectra are obtained leading to accurate determination of elemental concentrations. A variety of types of crystals are used in WD-XRF with synthetic thin film multilayer crystals being increasingly popular for their higher sensitivity and resolution for enhanced light element analysis. The range of detectable elements actually varies according to instrument configuration and set-up. ED-XRF covers the elements from Na to U, whereas WD-XRF has a broader analytical

window, starting from beryllium (Be). Concentrations can range from 100% down to ppm and in some cases sub-ppm levels. Limits of detection depend upon the specific element and the sample matrix but, as a general rule, heavier elements will have lower detection limits.[9] The instrument on wihch XRF analyses were carried out was a WD-XRF Bruker S8 Tiger 2. Fluorine content in the samples synthesized from FSA was the main parameter screened, but trace impurities were also monitored. The siliceous samples were first dispersed in cellulose (ratio $SiO_2$ : cellulose 9:1) and finely milled. The resulting mixture was then pressed on a $H_3BO_3$ pellet and finally analysed.

## A.9 Thermogravimetric Analysis (TGA)[10,11]

Thermogravimetric Analysis (TGA) is defined as a technique in which the mass change of a substance is measured as a function of temperature while the substance undergoes to a controlled temperature programme. The temperature programme must be taken to include holding the sample at a constant temperature other than ambient, when the mass change is measured against time. Mass loss is only seen if a process occurs where a volatile component is lost. TGA measurements provides information about phase transitions, absorption, adsorption, and desorption along with chemical phenomena including chemisorptions, thermal decomposition, and solid-gas reactions. A thermogravimetric apparatus consists of a precision balance with a sample pan located inside a furnace whose temperature can be programmed. The temperature is generally increased at constant rate. The analysis may be carried out under a variety of atmospheres including air, vacuum, inert gases, oxidizing/reducing gases, corrosive gases, *etc.* Before analysis, samples are laid into crucibles made of different materials and then placed into the furnace, such as platinum or fused alumina. In this work, the range of temperature of interest was 25- 850 °C with heating rate of 10 °C $min^{-1}$ while oxygen flux was set at 40 mL $min^{-1}$.

# A.10 Sulfur Retention Capacity and Laboratory Scale $H_2S$ Removal.[12]

## A.10.1 Assessment of Sulfur Retention Capacity

Sorbent desulfidation performances were assessed by analysing their related breakthrough curves. A breakthrough curve reports the adsorbate concentration of the adsorbate of interest in the outlet gas from the reactor as a function of the time. Its shape provides information about the mass transfer of the adsorptive-adsorbents system. Curve profile can be explained by taking into account the concentration of adsorbate within the sorbent as a function of the time. When fluid starts to flow through the bed, where it comes into contact with the first layer of sorbent ($t_1$), the amount of available sorbent rapidly falls down and the adsorbed close to the first layer will be saturated. In this case, the fluid leaving the bed does not contain $H_2S$ and this situation endures until the entire bulk of the sorbent is saturated ($t_2$). The break point occurs when the adsorbate concentration begins to increase in the outlet gas ($t_3$). Therefore, the estimation of the time passed until the break point occurs can be directly correlated to the removal capacity of the sorbent.
Two parameters are relevant for evaluating $H_2S$ removal performance of a sorbent:

- **Breakthrough Time ($t_b$):** defined as the time elapsed between the beginning of the desulfurization run and moment that $H_2S$ concentration has reached a given value in the outlet gas (in this work, fixed 100 ppm);
- **Breakthrough Capacity or Sulfur Retention Capacity (SRC):** representing the mass of sulfur adsorbed expressed in milligrams *per* gram of sorbent when breakthrough time is reached. It was calculated according to Eq. A.3:

$$SRC = \frac{V_{H_2S} \cdot t_b \cdot C_{A,in} \cdot MW_s}{W_{sorb}} \tag{A.3}$$

where:

- $V_{H_2S}$ is the volumetric rate of feed stream ($m^3\ s^{-1}$);
- $V_{H_2S}$ is the volumetric rate of feed stream ($m^3\ s^{-1}$);

- $t_b$ represents the breakthrough time (s);

- $C_{A,in}$is the $H_2$bconcentration (mol $m^{-3)}$);

- $MW_s$ is the molecular weight of elemental sulfur (g $mol^{-1}$);

- $W_{sorb}$ accounts for the adsorbed loading in the reactor (g).

### A.10.2 Experimental Setup of Desulfurization and Regeneration Cycles

Desulfurization performance was assessed at mid-temperature (300°C) and atmospheric pressure by first using a reactant gas containing 15,200 ppm (1.52 % v/v) of $H_2S$ in helium (inlet flow, 20 $cm^3$ $min^{-1}$), and then a *facsimile* specially prepared syngas with a composition of 1.52 % v/v of $H_2S$, 25 % v/v CO, 15 % v/v $H_2$ , and $N_2$ as balance gas (inlet flow, 20 $cm^3$ $min^{-1}$). To determine the desulfidation and regeneration activity, 50 mg of composite was placed on a quartz wool bed (50 mg) in a vertical quartz tubular reactor coaxially located in an electrical furnace. Before desulfurization, a pre-treatment at 300 °C for 30 minutes under a helium flow was carried out to remove air and moisture from the sorbent and the reactor. Then, a reactant gas containing 15,200 ppm of $H_2S$ (in helium or syngas) was fed into the reactor and $H_2S$ content in the outlet flow during adsorption was monitored by means of a quadruple mass spectroscopy (Thermo Electron Corporation). At the same time, $H_2O$ and $SO_2$ signals were also monitored while helium-carried $H_2S$ was fed. CO, $CO_2$ , $H_2$, and $H_2O$ signals were also gauged. As soon as $H_2S$ concentration had reached 15,200 ppm in outlet gas, the measurement was stopped and the system was purged by flowing helium (20 $cm^3$ $min^{-1}$) for one hour. Sulfur retention capacity of the sorbents was calculated as the difference between the composite and the bare support $b_t$ values. The error on SRC values was estimated to be 2 mg of sulfur *per* gram of sorbent. This estimate was based on several sulfurization cycles performed on fresh portions of the commercial sorbent Katalko JM 32-5. The regeneration process was performed on a Thermoquest 1100TPD/R/O equipped with a thermal conductivity detector (TCD) and a quadrupole mass spectrometer (QMS) to monitor $SO_2$ and $O_2$ signals. The composites were heated under an air flow (20 $cm^3$ $min^{-1}$) up to 500°C (heating rate 10°C $min^{-1}$) and the temperature was kept constant for three hours. To identify the samples

upon the different cycles of sulfurization and regeneration, a letter (S o R, respectively) and a number (denoting successive cycles) was added to the sample name. Sorbent lifetime, intended as regenerability of the active phase, thermal stability, and constant sulfur retention capacity value, is one evaluation of a sorbent. For this reason, three repeated sulfurization-regeneration cycles were performed on each sorbent. At the end of the cycles, a study of the thermal stability of the sorbents was carried out by performing $N_2$-physisorption measurements and low-angle x-ray diffraction.

# References


[1] Rouquerol, F.; Rouquerol, J.; Sing, K., *Adsorption by Powders and Porous Solids*; Rouquerol, F., Rouquerol, J., Sing, K., Eds.; Academic Press: London, 2014, pp 219–236, ISBN: 978-0-12-598920-6, DOI: https://doi.org/10.1016/B978-012598920-6/50009-9.

[2] Zhao, D.; Wan, Y.; Zhou, W., *Ordered Mesoporous Materials*; Wiley: 2013, ISBN: 9783527326358.

[3] Watt, I. M., *The Principles and Practice of Electron Microscopy*, 2nd ed.; Cambridge University Press: 1997, ISBN: 9781139170529, DOI: https://doi.org/10.1017/CBO9781139170529.

[4] Atkins, P.; de Paula, J., *Atkins' Physical Chemistry*; OUP Oxford: 2010, ISBN: 9780199543373.

[5] Wood, D.; Rabinovich, E. Infrared studies of Alkoxide Gels. *Journal of Non-Crystalline Solids* **1986**, *82*, Proceedings of the Third International Workshop on Glasses and Glass Ceramics from Gels, 171–176, ISSN: 0022-3093, DOI: https://doi.org/10.1016/0022-3093(86)90127-4.

[6] Orrù, F. Design of Functional Colloidal Magnetic Nanoparticles for Biomedical Applications., PhD Thesis, University of Cagliari, 2012.

[7] Duer, M. J., *Solid-State NMR Spectroscopy Principles and Applications*; Blackwell Science Ltd.: 2002, ISBN: 0-632-05351-8, DOI: https://doi.org/10.1007/0-632-05351-8.

[8] Jiles, D., *Introduction to Magnetism and Magnetic Materials, Second Edition*; Taylor & Francis: 1998, ISBN: 9780412798603.

[9] Beckhoff, B.; Kanngießer, B.; Langhoff, N.; Wedell, R.; Wolff, H., *Handbook of Practical X-Ray Fluorescence Analysis*; Springer ebook collection / Chemistry and Materials Science 2005-2008; Springer Berlin Heidelberg: 2007, ISBN: 9783540367222.

[10] Haines, P.; Laye, P.; Heal, G.; Group, T.; Price, D.; Warrington, S.; Staff, T.; Mallilnckrodt, M.; Wilson, R., *Principles of Thermal Analysis and Calorimetry*; RSC paperbacks; Royal Society of Chemistry: 2002, ISBN: 9780854046102.

[11] Coats, A. W.; Redfern, J. P. Thermogravimetric Analysis. A Review. *Analyst* **1963**, *88*, 906–924, DOI: 10.1039/AN9638800906.

[12] Cara, C. Siliceous and non-siliceous Mesostructured Iron Oxide Nanocomposites for $H_2S$ Removal from Syngas., PhD Thesis, University of Cagliari, 2017.

La borsa di dottorato è stata cofinanziata con risorse del
Programma Operativo Nazionale Ricerca e Innovazione 2014-2020 (CCI 2014IT16M2OP005),
Fondo Sociale Europeo, Azione I.1 “Dottorati Innovativi con caratterizzazione Industriale”

UNIONE EUROPEA
Fondo Sociale Europeo

*Ministero dell'Istruzione, dell'Università e della Ricerca*